Mechanobiology of Breast Cancer
a Rheological Approach from Spheroids to Extracellular Matrix

Tavasso, M.

DOI
10.4233/uuid:d924f5c6-47bf-4467-b245-275e0084988c

Publication date
2025

Document Version
Final published version

Citation (APA)
Tavasso, M. (2025). *Mechanobiology of Breast Cancer: a Rheological Approach from Spheroids to Extracellular Matrix*. [Dissertation (TU Delft), Delft University of Technology].
https://doi.org/10.4233/uuid:d924f5c6-47bf-4467-b245-275e0084988c

Important note
To cite this publication, please use the final published version (if applicable).
Please check the document version above.

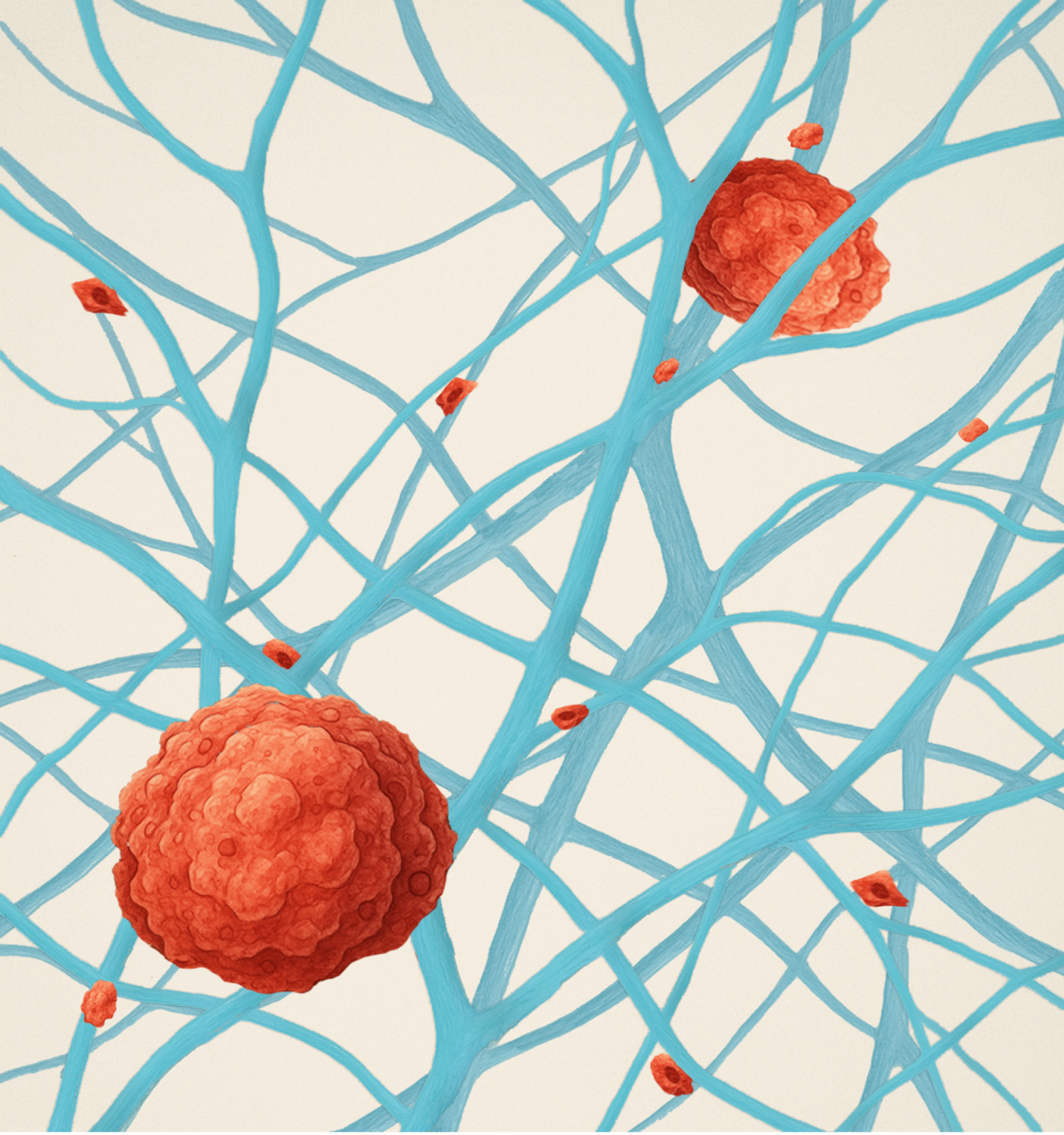

Mechanobiology of Breast Cancer

A Rheological Approach from Spheroids to Extracellular Matrix

Margherita Tavasso

MECHANOBIOLOGY OF BREAST CANCER

A RHEOLOGICAL APPROACH FROM SPHEROIDS TO EXTRACELLULAR MATRIX

MECHANOBIOLOGY OF BREAST CANCER

A RHEOLOGICAL APPROACH FROM SPHEROIDS TO EXTRACELLULAR MATRIX

Dissertation

for the purpose of obtaining the degree of doctor
at Delft University of Technology,
by the authority of the Rector Magnificus Prof. dr. ir. T.H.J.J. van der Hagen,
chair of the Board for Doctorates,
to be defended publicly on
Thursday, 9 October 2025 at 10.00 o'clock.

by

Margherita TAVASSO

Master of Science in Chemical Engineering,
Università degli Studi di Napoli Federico II, Italy
born in Napoli, Italy.

The dissertation has been approved by

promotor: Dr. P.E. Boukany
promotor: Prof. dr. V. Garbin

Composition of the doctoral committee:

Rector Magnificus,	Chairperson
Dr. P.E. Boukany	Delft University of Technology (promotor)
Prof. dr. V. Garbin	Delft University of Technology (promotor)
Independent members:	
Dr. M. Reffay	Université Paris Cité – CNRS
Prof. dr. ir. J. van der Gucht	Wageningen University and Research
Prof. dr. E. H. J. Danen	Leiden University Medical Centre
Dr. C. Chassagne	Delft University of Technology
Prof. dr. S.J. Picken	Delft University of Technology
Prof. dr. C. Joo	Delft University of Technology, reserve member

This work was financially supported the European Research Council.

Keywords: Rheology, Tissue mechanics, Microfluidics, Cell-matrix interactions, Rheo-confocal microscopy

Printed by: Gilderprint

Front & Back: An artistic impression of breast cancer spheroids and collagen by Carmen Giovanna Lavino.

ISBN 978-94-6496-467-7

An electronic version of this dissertation is available at
http://repository.tudelft.nl/.

Dedicated to my mother, my father and my sister.
You will always be my driving force.

CONTENTS

SUMMARY

Cancer development involves a series of complex events in which healthy cells undergo genetic modifications and begin proliferating uncontrollably. These cells may potentially spread to other locations in the body, through a process called metastasis, forming secondary tumors. Both cells and their surrounding environment, defined as the tumor microenvironment (TME), experience significant alterations during tumour progression. The TME is composed of cellular (e.g. fibroblasts, immune cells) and non-cellular components, like the extracellular matrix (ECM). The dynamic and reciprocal communication between cancer cells and TME is a key driver of cancer progression and invasion and triggers both physical and biological changes in a continuous feedback loop. For example, cells secrete matrix proteins, such as collagen, that increase the stiffness of the ECM around the primary tumor, but also enzymes like matrix metalloproteinases (MMPs) that degrade the ECM to facilitate invasion. On the other hand, tumour cells are also influenced by their environment: an increased compression from the ECM alters gene expression, causes cytoskeleton re-organization and activates signalling pathways that promote invasive behaviour. These events make cancer cells softer and more deformable, enabling them to overcome physical barriers to migrate through the TME. Unraveling the intricate crosstalk between cancer cells and the TME is a significant challenge, particularly in deciphering the cause-and-effect relationships underlying the biophysical, biochemical, and biological changes involved. To address this complexity, we focus on individual aspects and progressively connect our findings into a more comprehensive understanding.

This dissertation focuses on the biophysical properties of cancer cells and ECM, with a specific focus on rheological properties. Rheology examines how a material flows and deforms when subjected to applied forces. Based on their response, materials can be classified as elastic, viscous, or a combination of both. Individual cells and tissues exhibit both viscous and elastic properties, thus they are defined as viscoelastic materials. Changes in the viscoelastic properties of single cells and tissues have been linked to states of disease progression. The aim of this dissertation is to investigate the rheological behavior of tissue-like systems, with a focus on breast cancer.

One way to biophysically replicate disease progression is by applying external stimuli, such as compression, to cells or tissue and observing their response and changes in viscoelastic properties. In Chapter 2 of this dissertation, we developed a microfluidic device capable of imposing dynamic compression on multicellular aggregates (spheroids) composed of cells with varying malignancy. By modifying an established physical model, we extracted the viscoelastic properties of three different breast cancer spheroid types. Following compression, we assessed the spheroids' relaxation timescales and linked them to the cytoskeletal organization of F-actin and cell-cell adhesion properties. We demonstrated that, at the multicellular level, benign breast cancer spheroids exhibit higher bulk elastic modulus (E) and viscosity (η) compared to their malignant counterparts, similar to their constituent single cells, reinforcing the concept that increasing malignancy is associated with decreased stiffness and viscosity. Malignant breast cancer spheroids are more compliant to deformation than healthy spheroids and are prone to irreversible

deformation and fragmentation, facilitating the dissemination of invasive tumor cells under external physical forces.

Building upon this, in Chapter 3, we broadened our investigation to include the extracellular matrix (ECM). Specifically, examining how embedding active particles, such as cancer cells, influences the global rheology of the ECM through bulk rheology measurements. We modeled the ECM using its primary component, fibrillar collagen I, with embedded highly invasive MDA-MB-231 breast cancer cells at varying cell volume fractions. These cells actively interact with and remodel collagen fibers, altering the network's rheological properties when the cell volume fraction surpasses a certain threshold. Our findings revealed that, unlike fibroblasts or passive particles, invasive cancer cells induced an unexpected time-dependent softening of the collagen network and suppressed the classical stress-stiffening behavior typically seen in collagen matrices.

To understand the underlying mechanisms behind these altered rheological properties, we separated the effects of volume exclusion from those driven by active cellular processes, as observed through rheoconfocal microscopy experiments. Our results highlight that the interplay between volume exclusion, cell adhesion and contractility plays a crucial role in determining the rheology of collagen networks with active embedded inclusions, contributing to a deeper understanding of fibrous networks rheology and how their properties may be altered in disease contexts, such as cancer. Finally, in Chapter 4, the dissertation concludes with an outlook on potential future experiments and the possibilities and challenges involved in translating the findings of this research into diagnostic and/or therapeutic strategies.

SAMENVATTING

De ontwikkeling van kanker omvat een reeks complexe gebeurtenissen waarbij gezonde cellen genetische veranderingen ondergaan en ongecontroleerd beginnen te prolifereren. Deze cellen kunnen potentieel naar andere delen van het lichaam uitzaaien, via een proces genaamd metastase, en secundaire tumoren vormen. Zowel cellen als hun omgeving, gedefinieerd als de tumor micro-omgeving (TMO), ondergaan significante veranderingen tijdens de progressie van tumoren. De TMO bestaat uit cellulaire componenten (zoals fibroblasten, immuuncellen) en niet-cellulaire componenten, zoals de extracellulaire matrix (ECM). De dynamische en wederzijdse communicatie tussen kankercellen en de TMO is een belangrijke drijvende kracht achter de progressie en invasie van kanker en veroorzaakt zowel fysieke als biologische veranderingen in een continu feedbackmechanisme. Bijvoorbeeld, cellen scheiden matrixproteïnen uit, zoals collageen, die de stijfheid van de ECM rond de primaire tumor verhogen, maar ook enzymen zoals matrix metalloproteïnasen (MMP's) die de ECM afbreken om invasie mogelijk te maken. Aan de andere kant worden tumoren ook beïnvloed door hun omgeving: een verhoogde compressie vanuit de ECM verandert de genexpressie, veroorzaakt herorganisatie van het cytoskelet en activeert signaalroutes die invasief gedrag bevorderen.

Deze gebeurtenissen maken kankercellen zachter en meer vervormbaar, waardoor ze fysieke barrières kunnen overwinnen om door de TMO te migreren. Het ontrafelen van de complexe interactie tussen kankercellen en de TMO is een grote uitdaging, vooral bij het ontcijferen van oorzaak-en-gevolgrelaties die ten grondslag liggen aan de biofysische, biochemische en biologische veranderingen die erbij betrokken zijn. Om deze complexiteit aan te pakken, richten we ons op individuele aspecten en verbinden we geleidelijk onze bevindingen tot een meer alomvattend begrip.

Deze dissertatie richt zich op de biofysische eigenschappen van kankercellen en ECM, met speciale aandacht voor reologische eigenschappen. Reologie onderzoekt hoe een materiaal stroomt en vervormt wanneer het wordt blootgesteld aan aangebrachte krachten. Op basis van hun respons kunnen materialen worden geclassificeerd als elastisch, viskeus of een combinatie van beide. Individuele cellen en weefsels vertonen zowel viskeuze als elastische eigenschappen en worden daarom gedefinieerd als visco-elastische materialen. Veranderingen in de visco-elastische eigenschappen van enkele cellen en weefsels zijn gekoppeld aan stadia van ziekteprogressie. Het doel van deze dissertatie is om het reologisch gedrag van weefselachtige systemen te onderzoeken, met een focus op borstkanker.

Een manier om ziekteprogressie biofysisch te repliceren, is door externe stimuli zoals compressie toe te passen op cellen of weefsel en hun reactie en veranderingen in visco-elastische eigenschappen te observeren. In Hoofdstuk 2 van deze dissertatie ontwikkelden we een microfluïdisch apparaat dat in staat is om dynamische compressie toe te passen op multicellulaire aggregaten (sferoïden) samengesteld uit cellen met verschillende kwaadaardigheid. Door een bestaand fysisch model aan te passen, hebben we de visco-elastische eigenschappen van drie verschillende typen borstkankersferoïden geëxtraheerd. Na compressie hebben we de relaxatietijdschalen van de sferoïden beoordeeld en deze gekoppeld aan de cytoskeletorganisatie van F-actine en de eigenschappen van

cel-cel-adhesie. We hebben aangetoond dat op multicellulair niveau goedaardige borstkankersferoïden een hogere bulk elastische modulus (E) en viscositeit (η) vertonen vergeleken met hun kwaadaardige tegenhangers, vergelijkbaar met hun enkelvoudige cellen, waarbij het concept wordt versterkt dat toenemende kwaadaardigheid gepaard gaat met afgenomen stijfheid en viscositeit. Kwaadaardige borstkankersferoïden zijn meer vatbaar voor vervorming dan gezonde sferoïden en vertonen onomkeerbare vervorming en fragmentatie, wat de verspreiding van invasieve tumorcellen onder externe fysieke krachten vergemakkelijkt.

Voortbouwend hierop hebben we in Hoofdstuk 3 ons onderzoek uitgebreid om de extracellulaire matrix (ECM) op te nemen. Specifiek hebben we onderzocht hoe het insluiten van actieve deeltjes, zoals kankercellen, de globale reologie van de ECM beïnvloedt via metingen van bulkreologie. We hebben de ECM gemodelleerd met behulp van het primaire component, fibrillaire collageen I, met ingebedde zeer invasieve MDA-MB-231 borstkankercellen bij variërende celvolume-fracties. Deze cellen interageren actief met en verbouwen collageenvezels, wat de reologische eigenschappen van het netwerk verandert wanneer de celvolume-fractie een bepaalde drempel overschrijdt. Onze bevindingen onthulden dat, in tegenstelling tot fibroblasten of passieve deeltjes, invasieve kankercellen een onverwachte tijdafhankelijke verzachting van het collageennetwerk veroorzaakten en het klassieke stress-verstijvinggedrag onderdrukten dat typisch is voor collageenmatrices.

Om de onderliggende mechanismen achter deze veranderde reologische eigenschappen te begrijpen, hebben we de effecten van volume-uitsluiting gescheiden van die gedreven door actieve cellulaire processen, zoals waargenomen door reoconfocale microscopie-experimenten. Onze resultaten benadrukken dat de wisselwerking tussen volume-uitsluiting, celadhesie en contractiliteit een cruciale rol speelt bij het bepalen van de reologie van collageennetwerken met actieve ingesloten inclusies, wat bijdraagt aan een dieper begrip van de reologie van vezelige netwerken en hoe hun eigenschappen kunnen worden gewijzigd in ziektecontexten zoals kanker.

Tot slot, in Hoofdstuk 4, sluit de dissertatie af met een vooruitzicht op mogelijke toekomstige experimenten en de mogelijkheden en uitdagingen die gepaard gaan met het vertalen van de bevindingen van dit onderzoek naar diagnostische en/of therapeutische strategieën.

1

INTRODUCTION

1

Cancer is a fatal disease, responsible for 20 million new cases worldwide and 9.7 million deaths in 2022. Solid tumors, such as breast and lung cancer, are the most common cancers in women and men, both in incidence rate and in deaths [1]. The majority of the patients who die from cancer have experienced metastasis, a process in which cancerous cells spread throughout the body [2]. Metastasis requires tumor cells to leave their primary site, invade the tumor microenvironment (TME) and enter the bloodstream by breaking the basement membrane (intravasation). Circulating tumor cells can survive physical forces (such as pressure and shear stress) in blood vessels, exit the bloodstream (extravasation) and settle to a new cellular environment, establishing a secondary tumor [3]. Figure 1.1 presents a schematic of the metastatic cascade.

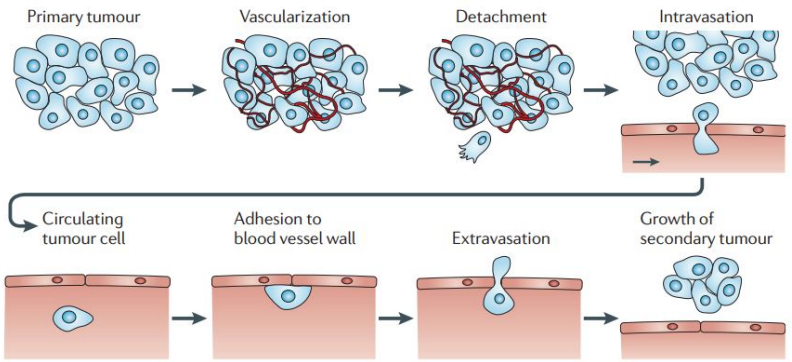

Figure 1.1: **Tumor metastasis schematic**. Cells detach from a primary, vascularized tumor, penetrate the surrounding tissue, enter nearby blood vessels (intravasation) and circulate in the vascular system. Some of these cells eventually adhere to blood vessel walls and are able to extravasate and migrate into the local tissue, where they can form a secondary tumor. Figure reproduced from [4].

In order to successfully form secondary tumors, cancer cells must interact physically and chemically with their surrounding environment, to invade the TME and consequently reach the bloodstream. The key component of the tumor microenvironment is the extracellular matrix (ECM), a complex mixture of proteins, glycoproteins, proteoglycans and polysaccharides that contribute to the structural and biochemical support of tissues [5]. As cancer progresses, the ECM undergoes dynamic adaptations, characterized by changes in its composition, topological structure and directionality, resulting in alterations in its physical properties, like increased stiffness. This increased stiffness impacts cancer cells by triggering signaling pathways, in a process known as mechanotransduction, which drives them toward a more malignant state [6]. During the metastatic process, the stiffening of the ECM was shown to promote the growth and invasion of mammary tissues [7]. This physical change is a defining feature of solid tumor growth and is often the primary indicator that clinicians and patients can detect, through palpation. The physical properties of the ECM (porosity, density and stiffness) play a crucial role in anti-cancer therapy, as ECM stiffness has been shown to influence drug resistance in breast cancer treatment [8].

A deeper investigation of these structural and physical changes in cancerous tissues can be achieved through biophysics, which provides a valuable framework for under-

standing the physical properties that distinguish them from healthy tissues [9]. By analyzing biophysical properties such as stiffness, shape, deformability and surface tension on different scales, from tissue to individual cells, research has made significant progress in understanding cancer progression and key cellular processes, including interactions with the ECM [10]. In the past decade, studies have focused on how variations in ECM composition and stiffness profoundly influence the migration of individual cells or cell clusters [11–14]. However, in this hybrid system where both ECM and cells are present, the relationship is reciprocal— while the ECM regulates cellular migration and invasion, cells also actively modify the ECM's biophysical properties, an aspect that has often been overlooked. This mutual interaction between cells and the ECM highlights the need to explore how cells actively modify the ECM.

Beyond ECM-driven influences, the intrinsic biophysical properties of multicellular tissues remain unexplored. Although single cancer cells have been shown to be softer than their healthy counterparts [7, 15], much less is known about multicellular aggregates and how their biophysical properties evolve with malignancy. At the primary site, tumor growth generates solid stresses (compressive, tensile and shear forces applied by non-fluidic elements of tissue) within the tumor and between the tumor and the host tissue, which affects its progression and invasion [16]. Therefore, understanding the inherent biophysical properties of tissues across different malignancy levels is crucial for predicting how they will respond to solid stresses. Addressing this gap could suggest new therapeutic targets aimed at alleviating solid stress in tumors [16] and could contribute to accelerate cancer diagnosis at early stages of the disease progression [17].

1.1. AIM OF THE DISSERTATION

This dissertation examines a specific subset of biophysical properties of cancer cells and ECM, defined as rheological properties, which focus specifically on the way (biological) materials flow and/or deform in response to externally applied force. Specifically, the aim is to investigate the rheological behavior of tissue-like systems, with a focus on breast cancer. To do so, tissue-like systems are analyzed from two distinct perspectives: (1) as multicellular aggregates exhibiting varying degrees of malignancy, subjected to dynamic compression and (2) as a composite system of ECM and individual cells, focusing on changes in the rheological response of cell-embedded ECM as cell density increases. To explore these aspects, the following research questions are addressed:

- What are the differences between the rheological properties of multicellular aggregates as their metastatic potential increases?
- Which biological characteristics of multicellular aggregates are associated with variations in their rheological properties across different malignancy levels?
- How is the presence of highly invasive cancer cells affecting the ECM rheological properties?
- What specific molecules or mechanisms mediate the interaction between individual cells and the ECM, leading to changes in the tissue's rheological properties?

1

In the following sections, relevant concepts regarding cancer tissue rheology and the experimental methods employed in this dissertation will be introduced.

1.2. VISCOELASTICITY OF LIVING TISSUES

Cells and tissues are classified as viscoelastic materials, exhibiting properties of both elastic solids and viscous fluids. An elastic material (e.g. a spring) displays a reversible deformation, meaning that once the external stress ceases, the material regains its original shape. The elasticity $E = \sigma/\epsilon$ is defined as the ratio of the applied stress σ and the resulting deformation ϵ. A viscous material (e.g. dashpot), instead, exhibits irreversible deformations when stress is applied and is characterized by viscosity $\eta = \sigma/\dot{\epsilon}$, where $\dot{\epsilon}$ is the rate of deformation, or strain rate [18]. Materials that exhibit both elastic response and viscous response to applied stress are denoted "viscoelastic" materials: due to time-dependent behavior, a viscoelastic material behaves as viscous in long time scale (minutes, hours, up to days) and appears as elastic in shorter experiment time (seconds to minutes). Cells display unique viscoelastic properties, like non-linear elasticity, which are mainly mediated by the cytoskeleton, a dynamic biopolymer network, that plays a crucial role in maintaining the shape of cells and providing them with mechanical support [19]. This network is composed of three major components: filamentous actin (F-actin), intermediate filaments and microtubules, as shown in Figure 1.2.

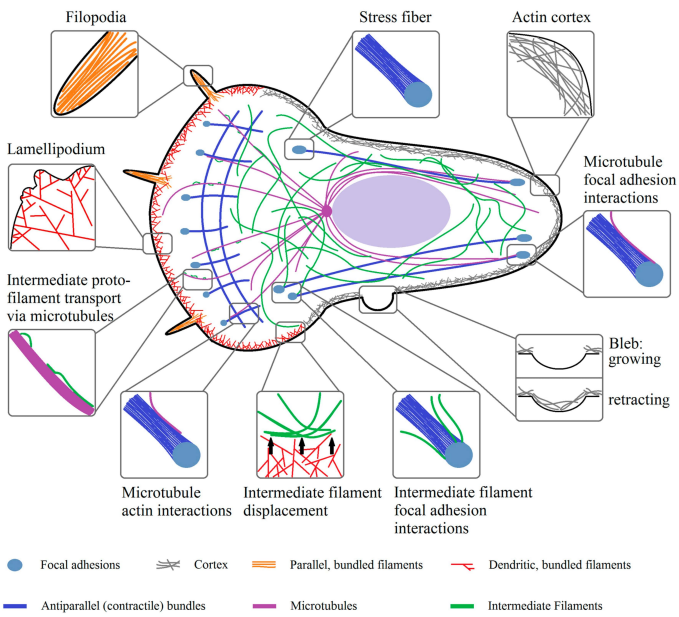

Figure 1.2: **The cytoskeleton.** Cells are provided with rigidity and structural support via the cytoskeleton. These functions are mediated by three polymerous filaments in the cytoskeleton: actin, microtubules and intermediate filaments, which interact with each other and form a dynamic network, which responds to internal and external cues and contributes to the overall non-linear viscoelasticity of the cell. Figure reproduced from [20].

Considerable research has been dedicated to studying the rheological properties of tissue-like materials through both experimental and theoretical approaches [21] with a focus on linking these properties to the corresponding behaviors observed at the single-cell level. These approaches include methods such as atomic force microscopy (AFM), optical tweezers and micropipette aspiration, all of which allow precise measurement of cell/clusters deformation in response to applied forces. In addition, many constitutive models have been developed, employing numerous combinations of two simple elements used as mechanical analogs: a spring element, which models time-independent elastic behavior and a dashpot element, which models time-dependent viscous behavior [22]. It is well-established that single-cell rheological properties vary with malignancy [23], however the relationship between these properties and the collective behavior of cells in a 3D aggregate (spheroid) remains poorly understood. Characteristics like cell-cell adhesion, packing density, stresses generated by tissue growth make it difficult to predict how rheological properties manifest at the multicellular level with increased malignancy.

1.3. SPHEROIDS AS 3D IN VITRO MODELS

Multicellular aggregates (spheroids) have emerged as promising 3D *in vitro* models to replicate the physiology of solid tumors. Spheroids are formed by sedimentation of single cells in a confined space and closely mimic the main biophysical features of solid tumors. Their cellular layered assembly reflects the pH, oxygen and nutrients gradients present in real tumors: the outer layer consists of highly proliferative cells, followed by a layer of quiescent cells and an inner layer of necrotic cells [24], as shown in Figure 1.3. Moreover, the capability of replicating the existing cell-cell and cell-ECM interactions in the tumor tissue, makes such system advantageous compared to 2D monolayer cultures and a suitable *in vitro* tumor model [25]. For this reason, multicellular spheroids are incorporated into various experimental platforms, to test their response to biochemical and biophysical factors under precisely controlled conditions, like microfluidic devices [26].

1.4. MICROFLUIDICS FOR TISSUE MECHANICS

Accurately measuring the rheological properties of tumor tissue is essential for understanding how they evolve during cancer progression and how these properties change with metastatic potential. Microfluidic devices provide an excellent platform to study *in vitro* cancer models in different physiological conditions, given their versatility in delivering physical and chemical cues. Compared to conventional techniques, the advantages of small sample volume, biocompatibility and high throughput make microfluidic technologies attractive for studying cell and spheroid biophysical properties. Microfluidic devices are, as suggested by the name, micro-sized flow channels, which can be printed in different geometries and patterns (with various techniques like soft lithography or 3D printing), that allow for live-imaging and controlled fluid flow [27, 28]. The diverse range of geometrical configurations enables the inclusion of physical constraints in the channels to apply compression in a controlled manner, or the application of shear stresses and interstitial fluid flow [29], further enhancing the ability to study how me-

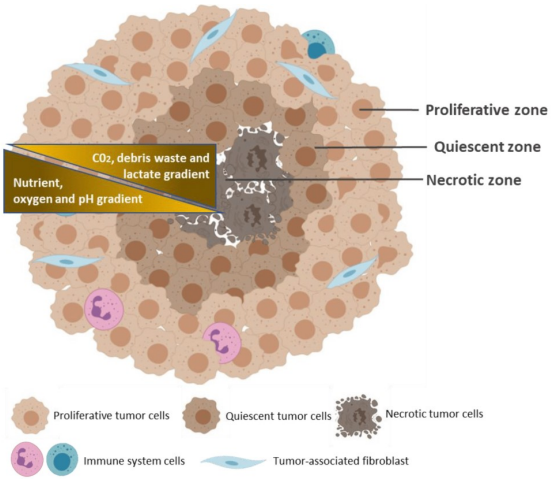

Figure 1.3: **Structural organization of a multicellular tumor spheroid**. Spheroids are multicellular self-organizing 3D aggregates that mimic *in vivo* tumor physiology. It consists of three zones: an outer layer of proliferating cells, a middle layer of quiescent cells and a necrotic core where lack of sufficient nutrients and accumulation of waste products lead to cell death. These distinct regions are the result of opposing gradients of oxygen, nutrients and pH moving inward, while metabolic byproducts such as CO_2, lactate and waste diffuse outward. Figure reproduced from [25].

chanical forces influence spheroid behavior. Additionally, hydrogels can be integrated within these microfluidic systems to mimic the ECM, providing a more physiologically relevant environment.

1.5. RHEOLOGY OF ECM-LIKE HYDROGELS AND RHEOCONFOCAL MICROSCOPY

Changes in the tissue bulk rheological properties is often correlated to the development of cancerous events, such as increased crosslinking of ECM proteins, like collagens and elastin, which make the tumor more rigid and contribute to its palpability [30]. To mimic experimentally the TME, hydrogels such as collagen, Matrigel, alginate are commonly used for *in vitro* cell studies. They provide the embedded cells with a highly hydrated environment, enabling the diffusion of nutrients and metabolites [31]. Collagen is the most abundant protein in the ECM and is involved in a dynamic crosstalk with tumor cells [32]. The rheological properties of tumors are closely linked to collagen deposition, as changes in collagen organization and abundance significantly affect the stiffness and viscoelasticity of the TME, influencing tumor progression and metastasis.

To assess these changes and their impact on tumor behavior, rheological measurements of cancerous tissues are needed, since they provide insights into the material's viscosity and elasticity, both essential for understanding tissue behavior. By using rheometers, which apply controlled stress or strain, we can characterize the response of collagen and other ECM proteins to externally applied forces. However, the rheological properties of both cells and the ECM are interconnected. Cells can dynamically modify their

stiffness in response to changes in the rheological properties of their surrounding environment, while, in turn, cellular activity—mediated by the actin-myosin cytoskeleton [33]—can influence the stiffness of the ECM through mechanical interactions at integrin receptors. This reciprocal relationship highlights the importance of rheology in understanding how cellular forces and ECM properties adapt in response to their mutual interactions.

While bulk rheological methods provide valuable insights into the macroscopic rheological properties of tissues, they are limited in their ability to capture changes at the micrometer length scale. To gain a deeper understanding of the microscopic alterations in the collagen matrix, rheo-microscopy serves as a powerful tool [34]. This advanced technique combines rheology with microscopy, enabling the real-time visualization and analysis of dynamic structural changes at the microscopic level. By integrating a microscope system, such as a confocal microscope, with a rheometer, rheo-microscopy allows for the examination of both the rheological and structural responses of collagen, but also cellular alterations occurring from dynamic crosstalk between collagen and surrounding cancer cells [35]. Through the use of staining techniques, for example of actin filaments, or by inhibiting specific ECM-cell interactions—such as adhesion or matrix degradation by metalloproteinases— it is possible to track cellular dynamics and pinpoint the mediators of these interactions. This enables the identification of factors that drive changes in the bulk rheological properties of collagen, clarifying the cellular and molecular mechanisms influencing tissue mechanics.

1.6. OUTLOOK OF THE THESIS

This dissertation investigates the rheological properties of breast cancer tissues to gain a deeper understanding of how tissue mechanics correlates to metastatic potential and to cell-interactions. In the next chapters (2 and 3) tissues are mimicked either as standalone multicellular systems, otherwise called spheroids, or as a system made of collagen hydrogel and single invasive breast cancer cells. Two different approaches are employed for the two systems: microfluidics is used to apply an external compressive stress to spheroids of different metastatic potential, while bulk rheology and rheoconfocal microscopy are employed to detect, quantify and visualize the ECM-cells interactions. In **Chapter 2**, a microfludic device equipped with a constricted channel and relaxation chamber is introduced. The chip provides controlled compression and allows for stress relaxation of breast cancer spheroids of different malignancy. Two constitutive models, adapted to the experimental conditions, are employed to extract rheological parameters (elasticity, viscosity, relaxation timescales). In addition, this chapter aims at identifying the biological component(s) responsible for the variations in rheological properties across different malignancy levels. **Chapter 3** introduces a unique method to investigate cell-collagen interactions influencing the overall tissue rheology. In particular, bulk rheology experiments of cell-embedded collagen (with increased cell density) demonstrate a softening of the collagen and a time-dependent behavior, particularly for a certain amount of cells embedded. We dive into the possible explanations of such evidence by observing *in situ* the interaction between collagen fibers and cells' cytoskeleton and by inhibiting acto-myosin contractility and adhesion via integrin receptors. The thesis concludes with **Chapter 4**, where key findings are critically discussed and an outlook on

potential future experiments is provided, with a focus on possible applications of these findings for diagnostic purposes.

REFERENCES

[1] F. Bray, M. Laversanne, H. Sung, J. Ferlay, R. L. Siegel, I. Soerjomataram, and A. Jemal, *Global cancer statistics 2022: GLOBOCAN estimates of incidence and mortality worldwide for 36 cancers in 185 countries,* CA: A Cancer Journal for Clinicians **74**, 229 (2024).

[2] M. B. Sporn, *The war on cancer,* Lancet **347** (1996), 10.1016/s0140-6736(96)91015-6.

[3] J. Fares, M. Y. Fares, H. H. Khachfe, H. A. Salhab, and Y. Fares, *Molecular principles of metastasis: a hallmark of cancer revisited,* Signal Transduction and Targeted Therapy **5** (2020), 10.1038/s41392-020-0134-x.

[4] D. Wirtz, K. Konstantopoulos, and P. C. Searson, *The physics of cancer: The role of physical interactions and mechanical forces in metastasis,* Nature Reviews Cancer **11**, 512 (2011).

[5] C. Echalier, L. Valot, J. Martinez, A. Mehdi, and G. Subra, *Chemical cross-linking methods for cell encapsulation in hydrogels,* Materials Today Communications **20** (2019), 10.1016/j.mtcomm.2019.05.012.

[6] Z. Mai, Y. Lin, P. Lin, X. Zhao, and L. Cui, *Modulating extracellular matrix stiffness: a strategic approach to boost cancer immunotherapy,* Cell Death and Disease **15** (2024), 10.1038/s41419-024-06697-4.

[7] C. Alibert, B. Goud, and J. B. Manneville, *Are cancer cells really softer than normal cells?* Biology of the Cell **109**, 167 (2017).

[8] Y. Jiang, H. Zhang, J. Wang, Y. Liu, T. Luo, and H. Hua, *Targeting extracellular matrix stiffness and mechanotransducers to improve cancer therapy,* Journal of Hematology and Oncology **15** (2022), 10.1186/s13045-022-01252-0.

[9] A. A. Gorfe, *Biophysics of cancer,* Biophysical Journal **121** (2022), 10.1016/j.bpj.2022.09.017.

[10] C. T. Mierke, *Extracellular Matrix Cues Regulate Mechanosensing and Mechanotransduction of Cancer Cells,* Cells **13** (2024), 10.3390/cells13010096.

[11] A. Elosegui-Artola, A. Gupta, A. J. Najibi, B. R. Seo, R. Garry, C. M. Tringides, I. de Lázaro, M. Darnell, W. Gu, Q. Zhou, D. A. Weitz, L. Mahadevan, and D. J. Mooney, *Matrix viscoelasticity controls spatiotemporal tissue organization,* Nature Materials **22**, 117 (2023).

[12] A. van der Net, Z. Rahman, A. D. Bordoloi, I. Muntz, P. t. Dijke, P. E. Boukany, and G. H. Koenderink, *EMT-related cell-matrix interactions are linked to states of cell unjamming in cancer spheroid invasion,* iScience **27**, 111424 (2024).

[13] W. Kang, J. Ferruzzi, C.-P. Spatarelu, Y. L. Han, Y. Sharma, S. A. Koehler, J. A. Mitchel, A. Khan, J. P. Butler, D. Roblyer, M. H. Zaman, J.-A. Park, M. Guo, Z. Chen, A. F. Pegoraro, and J. J. Fredberg, *A novel jamming phase diagram links tumor invasion to non-equilibrium phase separation,* iScience **24** (2021), 10.1016/j.isci.2021.103252.

[14] A. Aung, S. K. Davey, J. Theprungsirikul, V. Kumar, and S. Varghese, *Deciphering the Mechanics of Cancer Spheroid Growth in 3D Environments through Microfluidics Driven Mechanical Actuation,* Advanced Healthcare Materials **12** (2022), 10.1002/adhm.202201842.

[15] S. E. Cross, Y. S. Jin, J. Rao, and J. K. Gimzewski, *Nanomechanical analysis of cells from cancer patients,* Nature Nanotechnology **2**, 780 (2007).

[16] H. T. Nia, L. L. Munn, and R. K. Jain, *Physical traits of cancer,* Science **370**, eaaz0868 (2020).

[17] Y. Xin, K. Li, M. Huang, C. Liang, D. Siemann, L. Wu, Y. Tan, and X. Tang, *Biophysics in tumor growth and progression: from single mechano-sensitive molecules to mechanomedicine,* Oncogene **42**, 3457 (2023).

[18] Y. Lou, *Appetizer on soft matter physics concepts in mechanobiology,* Development Growth and Differentiation **65**, 234 (2023).

[19] F. Huber, A. Boire, M. P. López, and G. H. Koenderink, *Cytoskeletal crosstalk: When three different personalities team up,* Current Opinion in Cell Biology **32**, 39 (2015).

[20] T. Hohmann and F. Dehghani, *The cytoskeleton—a complex interacting meshwork,* Cells **8** (2019), 10.3390/cells8040362.

[21] R. C. Boot, G. H. Koenderink, and P. E. Boukany, *Spheroid mechanics and implications for cell invasion,* Advances in Physics: X **6** (2021), 10.1080/23746149.2021.1978316.

[22] R. K. Roeder, *Mechanical Characterization of Biomaterials,* in *Characterization of Biomaterials* (2013).

[23] A. Massey, J. Stewart, C. Smith, C. Parvini, M. McCormick, K. Do, and A. X. Cartagena-Rivera, *Mechanical properties of human tumour tissues and their implications for cancer development,* Nature Reviews Physics **6**, 269 (2024).

[24] A. S. Nunes, A. S. Barros, E. C. Costa, A. F. Moreira, and I. J. Correia, *3D tumor spheroids as in vitro models to mimic in vivo human solid tumors resistance to therapeutic drugs,* Biotechnology and Bioengineering **116**, 206 (2019).

[25] B. Pinto, A. C. Henriques, P. M. Silva, and H. Bousbaa, *Three-dimensional spheroids as in vitro preclinical models for cancer research,* Pharmaceutics **12**, 1 (2020).

[26] P. Mehta, Z. Rahman, P. ten Dijke, and P. E. Boukany, *Microfluidics meets 3D cancer cell migration,* Trends in Cancer **8**, 683 (2022).

[27] S. A. Vanapalli, M. H. Duits, and F. Mugele, *Microfluidics as a functional tool for cell mechanics,* Biomicrofluidics **3** (2009), 10.1063/1.3067820.

[28] G. Du, *Microfluidic platforms for cell analysis : applied to study cell mechanics and high-throughput screening,* Ph.D. thesis, Technische Universiteit Eindhoven (2016).

[29] Z. Rahman, A. D. Bordoloi, H. Rouhana, M. Tavasso, G. van der Zon, V. Garbin, P. ten Dijke, and P. E. Boukany, *Interstitial flow potentiates TGF-β/Smad-signaling activity in lung cancer spheroids in a 3D-microfluidic chip,* Lab on a Chip **24** (2023), 10.1039/d3lc00886j.

[30] E. Henke, R. Nandigama, and S. Ergün, *Extracellular Matrix in the Tumor Microenvironment and Its Impact on Cancer Therapy,* Frontiers in Molecular Biosciences **6** (2020), 10.3389/fmolb.2019.00160.

[31] M. W. Tibbitt and K. S. Anseth, *Hydrogels as extracellular matrix mimics for 3D cell culture,* Biotechnology and Bioengineering **103**, 655 (2009).

[32] Q. Zhang, Z. Y. An, W. Jiang, W. L. Jin, and X. Y. He, *Collagen code in tumor microenvironment: Functions, molecular mechanisms, and therapeutic implications,* Biomedicine and Pharmacotherapy **166** (2023), 10.1016/j.biopha.2023.115390.

[33] K. A. Jansen, R. G. Bacabac, I. K. Piechocka, and G. H. Koenderink, *Cells actively stiffen fibrin networks by generating contractile stress,* Biophysical Journal **105**, 2240 (2013).

[34] J. Läuger, A. P. Germany, and P. Heyer, *Rheo-Microscopy: Simultaneous structural and rheological information,* in *Annual Transactions of the Nordic Rheology Society* (2012).

[35] E. Cambria, M. F. Coughlin, M. A. Floryan, G. S. Offeddu, S. E. Shelton, and R. D. Kamm, *Linking cell mechanical memory and cancer metastasis,* Nature Reviews Cancer **24**, 216 (2024).

2

Linking Metastatic Potential And Viscoelastic Properties Of Breast Cancer Spheroids Via Dynamic Compression And Relaxation In Microfluidics

Abstract

The growth and invasion of solid tumors are associated with changes in their viscoelastic properties, influenced by both internal cellular factors and physical forces in the tumor microenvironment. Due to the lack of a comprehensive investigation of tumor tissue viscoelasticity, the relationship between such physical properties and cancer malignancy remains poorly understood. Here, the viscoelastic properties of breast cancer spheroids, 3D (*in vitro*) tumor models, are studied in relation to their metastatic potentials by imposing controlled, dynamic compression within a microfluidic constriction, and subsequently monitoring the relaxation of the imposed deformation. By adopting a modified Maxwell model to extract viscoelastic properties from the compression data, the benign (MCF-10A) spheroids are found to have higher bulk elastic modulus and viscosity compared to malignant spheroids (MCF-7 and MDA-MB-231). The relaxation is characterized by two timescales, captured by a double exponential fitting function, which reveals a similar fast rebound for MCF-7 and MCF-10A. Both the malignant spheroids exhibit similar long-term relaxation and display residual deformation. However, they differ significantly in morphology, particularly in intercellular movements. These differences between malignant spheroids are demonstrated to be linked to their cytoskeletal organization, by microscopic imaging of F-actin within the spheroids, together with cell-cell adhesion strength.

This chapter is published as M.Tavasso, A.D. Bordoloi, E. Tanré, S.H. Dekker, V. Garbin, P. E. Boukany, *Advanced Healthcare Materials (2024)* [1].

2.1. INTRODUCTION

The progression and invasion of solid tumors involve a complex interplay between tumor cells and their surrounding environment including blood and lymph vessels, immune cells, fibroblasts and extracellular matrix (ECM) [2, 3]. From a physical perspective, such interactions translate into solid stress (compressive and tensile forces applied by non-fluidic elements of the tumor environment) and interstitial fluid pressure, arising from tumor growth in confined spaces, ECM stiffening and remodeling, leaky blood vessels and altered lymphatic drainage system [4]. The mechanical properties of tissues, such as elasticity and viscosity, are significantly influenced by these cues, and instigate biochemical changes, which ultimately facilitate metastasis [5, 6].

The viscoelastic characterization of tumor cells has become a key indicator of tumor development and metastasis [7]. Nanomechanical analysis, performed using atomic force microscopy (AFM) of individual metastatic cells (from breast, lung and pancreatic cancer) in pleural fluids of patients showed that cancer cells are softer than their healthy counterparts [8]. This cell softening serves as a biomechanical adaptation to facilitate cancer invasion [9]. Several studies highlighted how confinement and compression can alter the intracellular structure of single cancer cells, linking their mechanical properties to their metastatic potential at the single-cell level. Malignant breast cancer cells traveling through microchannels that mimic blood vessels demonstrated to exhibit greater deformability compared to benign cell types [10, 11]. Additionally, invasive breast cancer cells showed residual irreversible deformations after squeezing through a tight constricted microchannel under flow conditions, attributed to cytoskeleton rearrangements [12]. Furthermore, nuclear envelope rupture and DNA damage occurred in several cancer cell lines during confined migration through narrow spaces and external compression [13].

At the tissue level, tumor cells are densely packed, held together by cell-cell junctions and surrounded by denser extracellular matrix, resulting in a stiffer tumor tissue compared to the surrounding healthy tissue [14, 15]. For this reason, numerous studies investigated how the mechanical properties of the ECM can profoundly alter single and collective cell migration from a primary tumor: the response to different levels of compressive, tensile and elongational stresses can be monitored in *in vitro* 3D tumor models (spheroids) by tuning the viscoelasticity, stiffness and composition of the surrounding matrix [16–19]. These approaches, however, only analyzed the solid tumor response in static conditions and in relation to the ECM composition [17], making it difficult to decouple the intrinsic spheroid's viscoelastic properties in response to dynamic external stresses from those of the surrounding ECM. In order to link the biophysical characteristics of spheroids and their metastatic potential in the early stage of metastasis, it is important to investigate these mechanical properties of tumor spheroids independent of the ECM. Solid and interstitial stress vary over a range of 0.21-20 kPa [20, 21] depending on the tissue examined and the tumor stage. Real time monitoring of 3D *in vitro* assays that impose and release controlled stress under biologically relevant conditions can unravel these properties.

Microfluidics provides a powerful platform to explore the viscoelastic properties of cancer spheroids within confined environment, due to its tunable geometries and dimensions [22]. Recent works involved microfluidic devices to study spheroid mechanics

via micropipette aspiration (MPA) in a high-throughput manner [23], or via compressing cellular aggregates in microchannels, to assess viscoelastic properties associated with the cell rearrangement and cell shape within the aggregate [24, 25]. Despite the valuable insights on the viscoelastic properties of tumor models gained from these studies, the relationship between the intrinsic viscoelastic characteristics of cancer spheroids and the degree of malignancy remains to be elucidated.

In this work, we establish this link by focusing on spheroids made from one non-tumorigenic epithelial cell line (MCF-10A) and two breast cancer cell lines with increasing metastatic potential(MCF-7 and MDA-MB-231). In a microfluidic chip, the spheroids are subjected to dynamic compression through a narrow constriction channel, with different level of confinement. We quantify the spheroids viscoelastic properties, by fitting the compression data to a modified Maxwell model adapted to the dynamic conditions, from which it is possible to distinguish the benign from the malignant spheroids. Then, we characterized the shape recovery of spheroids after compression during the relaxation process. Notably, comparing the fast and slow relaxation timescales of spheroids allows us to discern different degrees of malignancy, which we demonstrate to be closely associated with spheroid compactness and actin cortex arrangement.

2.2. RESULTS

2.2.1. MICROFLUIDIC ASSAY FOR DYNAMIC COMPRESSION AND RELAXATION OF BREAST CANCER SPHEROIDS

We develop a microfluidic assay to investigate the viscoelastic response of breast cancer spheroids subjected to dynamic compression. This assay involves flowing spheroids through a narrow constriction channel connected with a relaxation chamber (see Figure 2.1a). The flow rate is kept constant using a syringe pump. The pump withdraws one spheroid at a time from a suspension at the micropipette loading port, compressing each spheroid through the constriction channel (referred to as the compression stage). After passing through the constriction, the spheroids are released into a wider chamber where they can relax in the absence of flow (referred to the relaxation stage). The spheroid undergoes maximum compressive strain within the constriction channel, measured by the constriction index $I_c = (D_0 - d_c)/D_0$, defined by the width of the constricting channel d_c, and the equivalent spherical diameter of the spheroid D_0, such that a larger I_c signifies larger maximum strain. We prevent the spheroid from tumbling in the observation plane by maintaining the channel height below D_0 ($180 \pm 15\mu$m). We estimate the spheroid deformation during dynamic compression through the axial strain $\epsilon = (D(t) - D_0)/D_0$, where $D(t)$ refers to the axial dimension of the deformed spheroid over time (Figure 2.1b).

The dynamic compression of the spheroid can be characterized by three distinct phases: tongue aspiration ($t_1 < t \leq t_2$), impregnation ($t_2 < t \leq t_3$), and maximal compression ($t_3 < t \leq t_4$). Figure 2.1d captures the dynamics of these phases for a representative MCF-7 spheroid with $I_c = 0.63$ demonstrating the corresponding time-wise variations in the (I) pressure difference across the channel (ΔP), (II) velocity of the spheroid (u_s), and (III) its axial strain (ϵ). Immediately after clogging the entrance of the constriction channel ($t = t_1$), the spheroid's velocity drops significantly, accompanied by an

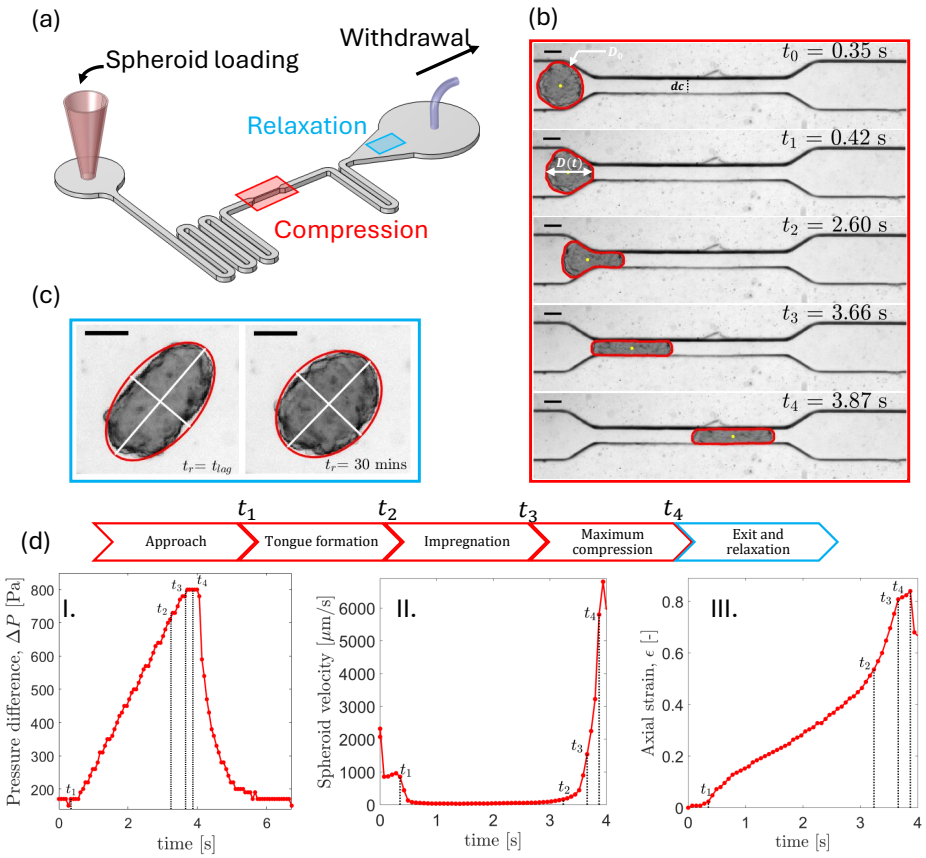

Figure 2.1: **Design and working principle of the microfluidic device for viscoelastic characterization of breast spheroids with different level of malignancy.** a) Schematic of the microfluidic chip for spheroids' dynamic compression and relaxation. The rectangles identify the middle constriction (red) and the relaxation chamber (light blue). b) Showcase of MCF-7 (I_c = 0.63) spheroid during the compression phase, with emphasis on relevant time points. The equivalent spherical diameter D_0 and the axial dimension over time $D(t)$ are highlighted. The spheroid edge is in red and the centroid in yellow. c) Showcase of the same MCF-7 spheroid during the relaxation phase at recovery time $t_r = t_{lag}$ and 30 minutes respectively. A red ellipse estimates the spheroid shape, with the major and minor axes, shown in white, tracked over time for subsequent data analysis. d) Time axis and identification of relevant time points of the deformation events and corresponding evolution of pressure difference across the channel (I), spheroids velocity (II) and axial strain (III) as function of time. Scale bar of the brightfield images: 100 μm.

increased pressure difference across the channel. This increasing ΔP dynamically compresses the spheroid by initiating a tongue at the leading front that is aspirated through the channel ($t > t_1$). As soon as the spheroid's centroid transits the constriction channel ($t = t_2$), the trailing end rapidly slips into the channel, leading to complete impregnation at $t = t_3$ and a sudden acceleration of the spheroid. During this phase, a rapid growth in axial strain ϵ takes place, reaching its maximum during the time $t_3 < t \leq t_4$ as the spheroid flows inside the constriction channel. At $t \geq t_4$, the spheroid unclogs and exits from the constriction enabling fluid flow through the channel, with a consequent drop in ΔP and u_s.

We monitor the relaxation of the spheroid for 30 minutes in the adjacent relaxation chamber. The relaxation monitoring was restricted to 30 minutes to minimize cell contact with the underlying glass slide and ensure cell viability (details in the Experimental Section). Unlike the constrained relaxation observed in MPA [26], the spheroids here are allowed to relax freely after exiting the constriction channel. Due to the imaging conditions and the chip design, it is not possible to capture both the constriction channel and the relaxation chamber within the same field of view. This results in a lag time $t_{\text{lag}} \approx$ 15-34 s (Figure S.2.1) between the frames at t_4, where the spheroids experience maximum compression, and the start of the relaxation monitoring (Figure 2.1c). We quantify the morphological relaxation of spheroid through a deformation parameter ($\mathscr{S}_r$) and the circularity ($\mathscr{C}_r$). Here, $\mathscr{S}_r = \frac{a(t)-b(t)}{a(t)+b(t)}$ with a and b being the major and minor axes of the ellipse, respectively, that fits the 2D spheroid boundary (see Figure 2.1c and 2.3a) [27–29] (details in the Experimental Section, Data acquisition and analysis). The circularity is quantified as $\mathscr{C}_r = (4\pi \cdot \text{Area}/\text{Perimeter}^2)$.

2.2.2. VISCOELASTIC RESPONSE AS A SIGNATURE OF METASTATIC POTENTIAL IN SPHEROIDS UNDER COMPRESSION

To probe the link between viscoelastic properties of spheroids and their cancer malignancy, we measure the axial deformation during the dynamic compression of three different breast cancer spheroids, formed from benign cells (MCF-10A) and from low and high metastatic cells (MCF-7 and MDA-MB-231). Figure 2.2a shows the time evolution of axial strain (ϵ) for three representative spheroids of each phenotype. Notably, the spheroid from the healthy cell line (MCF-10A) exhibits the highest resistance to deformation, followed by MCF-7 and MDA-MB-231, consistent with their increasing metastatic potential (see Supporting Movie S1). The benign spheroid (MCF-10A) demonstrates a significant delay in tongue formation with t_1= 68.9 s, in contrast to the two cancer spheroids (MCF-7 and MDA-MB-231) with $t_1 \approx 0.07$ s (as shown in Figure 2.2c). This results in an order of magnitude longer entry time ($t_E = t_3 - t_0$) (see Figure 2.2d), defined as the duration from when the spheroid contacts the entrance of the constriction channel (t_0) until the spheroid has completely entered the middle channel at time (t_3). We do not observe a statistically significant difference in t_E between the two malignant spheroids (MCF-7 and MDA-MB-231). Once the spheroid is fully inside the constriction channel during maximum compression, it traverses through the channel at nearly the same rate regardless of the cell type.

To estimate the elastic modulus (E) and viscosity (η) of each spheroid based on the evolution of its axial strain under dynamic compression, we adapt the modified Maxwell

model to account for the dynamic experimental conditions of our microfluidic assay. The modified Maxwell model was applied to MPA techniques previously to assess the viscoelastic properties of biological drops [30], and multicellular spheroids [23, 31]. The proposed model consists of four elements [32], as depicted in Figure 2.2b: the Kelvin-Voigt body is characterized by a spring of elasticity E, accounting for the bulk elasticity of the spheroid, in parallel with a spring of elasticity E^* and a dashpot of viscosity η^*. The latter two describe the initial elastic jump in the strain and the local viscosity respectively. Another dashpot in series characterizes the bulk viscosity η of the spheroid (or aggregate). The governing empirical equation describing strain evolution in this system is given by (full derivation in SI):

$$\ddot{\varepsilon} + \frac{\dot{\varepsilon}}{\tau_c} = \left(\frac{1}{E\tau_c} + \frac{1}{\eta}\right)\dot{\sigma} + \frac{1}{\eta\tau_c}\sigma, \tag{2.1}$$

where $\tau_c = \frac{\eta^*(E+E^*)}{EE^*}$ is a characteristic time for the fast elastic jump, determined by the cell-scale viscoelasticity (E^* and η^*) [32]. The applied stress σ, due to the pressure difference across the channel, is given by $\sigma(t) = \Delta P(t) = \Delta P_0 + \Delta\dot{P}t$. Here, $\Delta\dot{P}$ is the slope of the linear increment in the pressure (ΔP) against time during tongue formation (see Figure 2.1d (I)). The integration of Equation (1) yields the generalized equation presented in Equation (2), which we refer to as the dynamic modified Maxwell model (D3M). This model describes strain as a function of the time-dependent pressure difference (linked to the applied stress), and the viscoelastic parameters (E and η) of the spheroid:

$$\varepsilon(t) = \frac{\Delta P_0}{E}\left(1 - \frac{E^*}{E^*+E}e^{-\frac{t}{\tau_c}}\right) + \frac{\Delta P_0 t}{\eta} + \frac{\Delta\dot{P}t}{E} + \frac{\Delta\dot{P}t^2}{2\eta} + \frac{\Delta\dot{P}\eta^*}{E^2}\left(e^{-\frac{t}{\tau_c}} - 1\right) \tag{2.2}$$

The right-hand side of equation (2) comprises five terms: the non-linear elastic jump, linear viscous and linear elastic terms, non-linear viscous term, and non-linear viscoelastic term. The analysis reported in Figure S.2.2 shows that the last term, with E^2 in the denominator, is negligible. In the limit of a constant ΔP, condition used in earlier studies with micropipette aspiration, we recover the modified Maxwell model equation [30]. Since D3M considers the pressure to be a linear function of time, the onset time for tongue aspiration (t_1) corresponds $\Delta P = \Delta P_0$, initial condition of the model. As illustrated in Figure 2.2b, this D3M model captures the strain evolution curve through the tongue aspiration phase ($t_1 < t \leq t_2$) for all three spheroids. The brightfield images in Figure 2.2c compare the shape of each spheroid phenotype at the beginning (t_1) and the end (t_2) of the tongue aspiration phase. The accuracy of the D3M fit is found to be better than the modified Maxwell model (see Figure S.2.3 and Table S.2.1), which does not include the time-dependent linear elastic and non-linear viscous components of strain (see Equation 2). The data, as well as the model, shows a more distinct initial jump in ϵ for the more metastatic cell line, MDA-MB-231, which emphasizes the tendency of tumor cells to respond promptly and adapt to the deformations induced by either external forces or confinements. Immediately after the end of aspiration (when the spheroid centroid enters the constriction), the model becomes incapable to capture the sudden increase in strain, likely due to the unaccounted acceleration of the spheroid in the subsequent impregnation phase.

The viscoelastic response observed in Figure 2.2b is reflected in the parameters (E and η) obtained from fitting the D3M: Figures 2.2e-f reveal that the benign (MCF-10A) spheroids have higher elastic modulus and viscosity compared to the spheroids made of malignant cells for the constriction index ranges $I_c \geq 0.6$. The values of elastic modulus and viscosity are in agreement with previous studies that employed MPA [23, 24], compression tests [33–35] and AFM on breast spheroids [36], which reported elastic moduli of the order of $\sim 10^2 - 10^3 Pa$ and viscosity reaching values up to $10^5 Pa \cdot s$. The time-scale ($\tau_t = \eta/E$) over which the spheroid transitions from the elastic to the viscous regime during compression [32] is higher for MCF-10A (median τ_t = 8.3 s) compared to MCF-7 (median τ_c = 2.9 s) and MDA-MB-231 (median τ_t = 4.4 s), suggesting that the benign spheroid transitions more slowly into the viscous regime than the malignant spheroids (see Figure S.2.4).

We also compare the viscoelastic properties of MCF-7 and MCF-10A spheroids at low and high levels of compression, with $I_c < 0.6$ and $I_c \geq 0.6$, respectively (see Figure S.2.5). Notably, the spheroid viscoelasticity for MCF-10A is I_c-dependent, showing an order of magnitude increase for both E and η as the imposed compression increases ($I_c \geq 0.6$), in a similar trend as in single cells observed previously [37]. The effect of the constriction index for MCF-7 spheroids is minimal, with no significant difference in both E and η for lower compression levels, when $I_c \geq 0.6$. The experiments with MDA-MB-231 cells are limited only to $I_c \geq 0.6$ due to the difficulties in forming smaller, more compact spheroids that would fall within a lower I_c range.

2.2.3. RELAXATION RESPONSE AND SHAPE RECOVERY OF SPHEROIDS WITH DIFFERENT METASTATIC POTENTIALS

To test if the relaxation behavior of the spheroids also bears signatures of metastatic potential, we analyze their subsequent shape recovery in the absence of flow. Figure 2.3(a) shows representative images of three spheroids at the first ($t = t_{lag}$) and last (t = 30 min) captured frames in the relaxation chamber. Figure 2.3b and 2.3c illustrate the typical relaxation of MDA-MB-231, MCF-7 and MCF-10A spheroids through the time-wise evolution in the dimensionless deformation parameter ($\mathscr{S}_r$) and circularity ($\mathscr{C}_r$). For both curves, the starting points correspond to the values of $\mathscr{S}_r$ and $\mathscr{C}_r$ at the moment of maximum compression at $t = t_4$. This allows for the retrieval of the spheroid status immediately preceding the start of relaxation despite the lag time. After a fast rebound (see inset of Figure 3b), all three spheroids relax slowly and asymptotically toward a plateau (see Supporting Movie S2). In contrast to healthy MCF-10A spheroid, the malignant MCF-7 spheroid continues to relax and does not retrieve its original deformation ($\mathscr{S}_{r0}$) until the end of the experiment ($\approx$ 30 min). This results in a residual deformation ($\mathscr{S}_{r\infty} > \mathscr{S}_{r0}$) for MCF-7, associated with long time viscous effects. Interestingly, the MDA-MB-231 spheroid shows a different relaxation behavior compared to the other two cell-types. The MDA-MB-231 (with mesenchymal features) spheroids relaxes through rearrangement of constituent cells, such that the final deformation parameter ($\mathscr{S}_{r\infty}$) fluctuates significantly among cases and even reduces below its pre-compression value $\mathscr{S}_{r0}$ in the example shown in Figure 2.3b. To quantify the fast and slow relaxation and the subsequent residual deformation of breast spheroids, we employ a double exponential model (DEM) fit to the measured temporal deformation parameter ($\mathscr{S}_r$), given by:

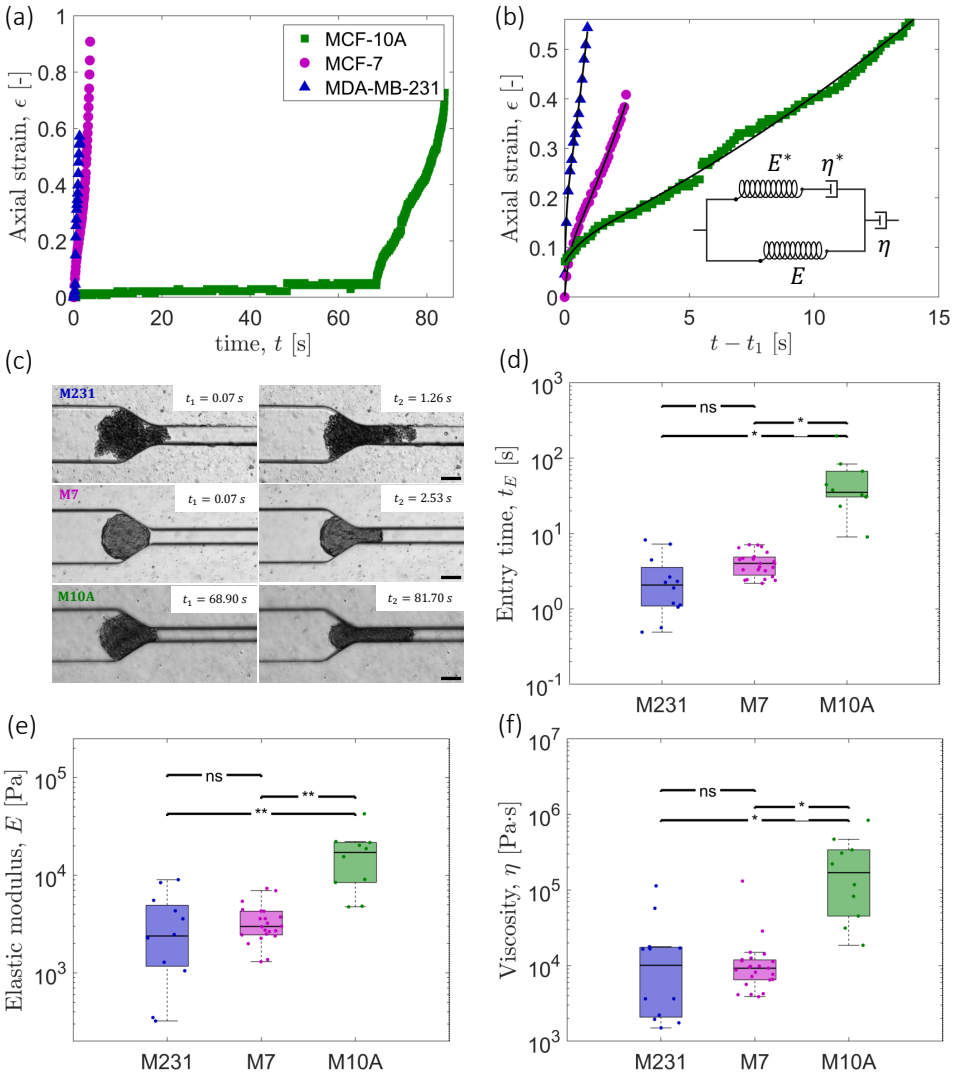

Figure 2.2: **Dynamic compression of spheroid and the Dynamic Modified Maxwell model (D3M) fitting to determine spheroids viscoelastic properties.** a) Time-wise evolution of axial strain during spheroid dynamic compression and deformation: The MCF-10A curve shows a delay in the rising of the axial strain, attributed to the longer time needed for tongue formation. b) The strain curves, shifted to the beginning of tongue formation t_1, are fitted with the D3M, the model being illustrated in the inset. c) Brightfield images of MDA-MB-231, MCF-7 and MCF-10A spheroids in the constriction channel: snapshots taken at time t_1 and t_2, showing that the time for MCF-10A spheroids for tongue formation is much longer than the other two malignant spheroids. Scale bar: 100 μm. d) Entry time (t_E) of the three spheroid types for $I_c \geq 0.6$. MDA-MB-231 (n=12) and MCF-7 (n=23) spheroids require a shorter time to fully enter the middle constricted channels compared to MCF-10A (n=10). e) and f) Boxplots comparing the spheroids bulk elastic moduli (E) and viscosity (η) for different metastatic potentials and for constriction index $I_c \geq 0.6$ (n_{M231}=12), (n_{M7}=23), (n_{M10A}=10). Data = solid line in the boxplot is the sample median. Box edges are first and third quartiles (IQR). Whiskers within 1.5 IQR value. The significance was calculated by a two-tailed t-test: ns = non significant, $p < 0.01$ (**) and $p < 0.05$ (*).

$$\mathscr{S}_r(t) = A_1 \exp(-t/\tau_1) + A_2 \exp(-t/\tau_2) + \mathscr{S}_{r\infty}. \tag{2.3}$$

The DEM characterizes the multiscale relaxation process via the two time-scales: τ_1 (short) and τ_2 (long), and the residual deformation ($\mathscr{S}_{r\infty}$) as fitting parameters. Herein, τ_1 corresponds to the immediate rebound of the spheroid after exiting from the constriction channel, and τ_2 to the subsequent long-term local rearrangements, likely associated with inter-cellular interactions. Both breast cancer single cells and other non-cancerous compressed multicellular aggregates are known to exhibit such double exponential behavior as observed in earlier studies [33, 38–41], based on other techniques like tissue surface tensiometry and AFM. For the spheroids used in our study, the relaxation curves are better captured by the DEM compared to some other fitting models, such as a single exponential and power-law fittings [42, 43], as shown in Figure S.2.6.

All three types of spheroids show an early-time fast elastic rebound with τ_1 of the order of $\approx$ 10 seconds, indicating an immediate elastic response after exiting the constriction. We find this timescale to be the shortest for the benign spheroid (MCF-10A), followed by progressively longer τ_1 corresponding to malignant spheroids (MCF-7 and MDA-MB-231), as shown in Figure 2.3d. The statistical difference in τ_1 among the three spheroid is significant only when comparing the benign (MCF-10A) and low-metastatic (MCF-7) spheroids with the highly metastatic (MDA-MB-231) spheroids. Notably, both MCF-7 and MCF-10A can be distinguished from highly metastatic MDA-MB-231 spheroids in terms of greater compactness, quantified by their high circularity values ($\mathscr{C}_r \approx 1$) prior to compression (Figure 2.3g). The absence of the inherent cell-cell adhesion in the latter resulted in less spherical MDA-MB-231 spheroids with circularity values ($\mathscr{C}_r \approx 0.85$). To examine this further, we visualize the F-actin distribution within each spheroid prior to compression (Figure 2.4a-b). We observe that both MCF-10A and MCF-7 form compact spheroids distinguished by a peripheral actin rim, which is more pronounced in the benign MCF-10A spheroids. Based on this result, we hypothesize that the fast relaxation (i.e. τ_1) is primarily influenced by surface elasticity resulting from the peripheral distribution of actin fibers, rather than solely by the bulk elasticity. This is supported by the significant difference in bulk elastic moduli, yet similar τ_1 values, between MCF-10A and MCF-7. To test this hypothesis, we examined the relaxation behavior of MCF-7 spheroids treated with blebbistatin, an inhibitor of myosin-II-specific ATPase, responsible for decreased acto-myosin contractility (see Figure S.2.8a). The MCF-7 spheroids treated with blebbistatin show different relaxation dynamics compared to untreated cases. In particular, the fast relaxation timescale τ_1 is statistically higher when the acto-myosin contractility is inhibited, whereas the longer relaxation timescale τ_2 remains unaltered. Furthermore, the F-actin immunostaining on MCF-7 (+ blebbistatin) spheroids reveals slightly rougher contours suggesting a reduced contractile actin rim compared to the untreated spheroids (see Figure S.2.8b). In contrast to MCF-7 and MCF-10A, MDA-MB-231 exhibits lower circularity ($\mathscr{C}_r \approx 0.85$), lacks a visible F-actin cortex, and thereby displays prolonged initial relaxation and greater variability in the τ_1 values. This suggests that the absence of a structured actin cortex contributes to a more heterogeneous and extended relaxation response in the MDA-MB-231 spheroid (see inset in Figure 2.3b).

The subsequent slow relaxation is characterized by the longer timescale τ_2, governed by the bulk elasticity (E). Benign spheroids (MCF-10A) exhibit the shortest relaxation

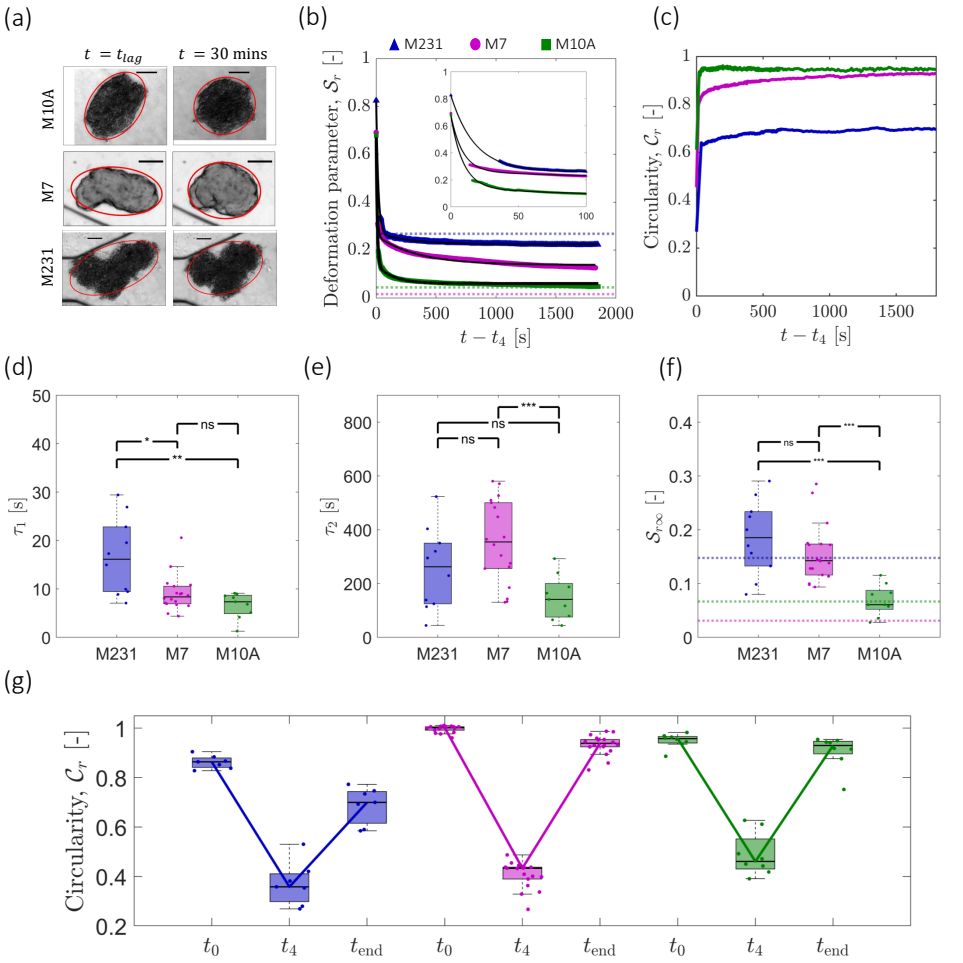

Figure 2.3: **Shape relaxation and recovery of spheroids with different metastatic potential after the dynamic compression ($I_c \geq 0.6$).** a) Brightfield images of MDA-MB-231, MCF-7 and MCF-10A spheroids in the relaxation phase: images taken at t = lag time and after 30 minutes from the time of maximum compression t_4. b) Deformation parameter $\mathscr{S}_r$ over time and the double exponential model (DEM) fitting. The starting point in each curve is shifted to t_4 and refers to the $\mathscr{S}_r$ value at maximum compression. The dotted lines refer to the deformation parameter of each spheroid prior to compression $\mathscr{S}_{r0}$. The inset shows the fitting of the first 100 seconds. c) Circularity $\mathscr{C}_r$ curve over time during the relaxation phase. MCF-10A and MCF-7 spheroids recover the circular shape, whereas MDA-MB-231 spheroids maintain an irregular shape after deformation. d) Short (τ_1) e) long (τ_2) timescales of relaxation and f) residual deformation $\mathscr{S}_{r\infty}$ based on the DEM fits for spheroids of $I_c \geq 0.6$. The dotted lines in 3f indicate the median values of the deformation parameter prior to compression $\mathscr{S}_{r0}$ (n_{M231}=10), (n_{M7}=18), (n_{M10A}=9). g) Boxplots of circularity $\mathscr{C}_r$ before compression (t_0), at the maximum compression (t_4) and after 30 minutes of relaxation (t_{end}) for the three spheroid type. The highly metastatic spheroids do not recover their initial circularity values, differently from the less metastatic MCF-7 spheroids and the benign MCF-10A spheroids (n_{M231}=7), (n_{M7}=18), (n_{M10A}=8). Data = solid line in the boxplot is the sample median. Box edges are first and third quartiles (IQR). Whiskers within 1.5 IQR value. The significance was calculated by a two-tailed t-test: ns = non significant, $p < 0.001$ (***), $p < 0.01$ (**) and $p < 0.05$ (*).

time (with $\tau_2 < 141$ s), indicative of their higher elasticity and compact structure, enabling quick and uniform relaxation. The two malignant cell lines (MCF-7 and MDA-MB-231) display similar slow relaxation times, but with higher τ_2 compared to MCF-10A. These late-time relaxation timescales are consistent with the E values derived from dynamic compression and deformation, with lower elasticity for the malignant spheroids (MCF-7 and MDA-MB-231) compared to MCF-10A spheroids. The median value of τ_2 for MDA-MB-231 is smaller, yet not statistically different, than for MCF-7. MDA-MB-231 cells form a more compliant and flexible spheroid, with cells at the periphery that are more free to move and rearrange, while MCF-7 spheroids, despite being less metastatic, maintain their deformed state for a longer time, but are still capable to recover most of the spherical initial shape (up to 93.7%), as shown by the circularity plot in Figure 2.3g.

At the end of 30 minutes of relaxation, all benign MCF-10A spheroids nearly regain their original deformation $\mathscr{S}_{r0}$, such that $\mathscr{S}_{r\infty} \rightarrow \mathscr{S}_{r0}$ (Figure 2.3f). They also achieve a final circularity value nearly identical to their initial shape before compression (retrieving 97% of original circularity), as depicted in Figure 2.3g. By contrast, the malignant MCF-7 cell lines display much greater resistance to recovery due to long time viscous effects with significant residual deformation ($\mathscr{S}_{r\infty}$) at the end of our experimental time. The residual deformation of MDA-MB-231 ($\mathscr{S}_{r\infty}$) is found to be case specific due to cell-cell rearrangements, which results in a broad range of $\mathscr{S}_{r\infty}$ values both above and below their original deformation parameter ($\mathscr{S}_{r0}$). The two malignant spheroids also differ significantly in their morphological recovery: MCF-7 spheroids regain a spherical shape, while MDA-MB-231 spheroids display fragmented edges, with cells moving in different directions (Supporting Movie S2), leading to an overall irregular spheroid shape.

2.3. DISCUSSION AND CONCLUSION

In this work, we investigate the relationship between the viscoelastic properties of breast spheroids and their metastatic potential through dynamic compression and relaxation experiments. We use a microfluidic chip to systematically analyze spheroid deformation and subsequent relaxation, allowing us to obtain the bulk elastic modulus (E) and viscosity (η) through a viscoelastic model tailored to the experimental conditions.

Benign spheroids display higher E and η compared to the low and high metastatic counterparts (MCF-7, MDA-MB-231). These findings on breast cancer spheroids align with previous studies on single breast cancer cells [37, 44–46] and on spheroids of different tissues, e.g. originating from bladder cancer [47]. Notably, among the three cell lines, only MCF-10A shows significant sensitivity in both E and η to the imposed maximum strain, with higher values corresponding to increased level of maximum strain. This behavior, also observed on single MCF-10A cells previously [37], indicates that the apparent viscoelasticity of a spheroid is not only imposed strain-dependent [48], but also is specific to spheroid metastatic potential.

Additionally, the variation in spheroid entry time relative to metastatic potential corroborates earlier findings on single breast cancer cells in a similar constriction channel [10]. The higher entry time for benign MCF-10A cells, compared to MCF-7 and MDA-MB-231, was attributed to their greater stiffness, and correlates with both bulk elasticity and viscosity (Figure S.2.7). Overall, these studies suggest that malignant breast cancer spheroids, similar to their constituent single cells, are more compliant to deforma-

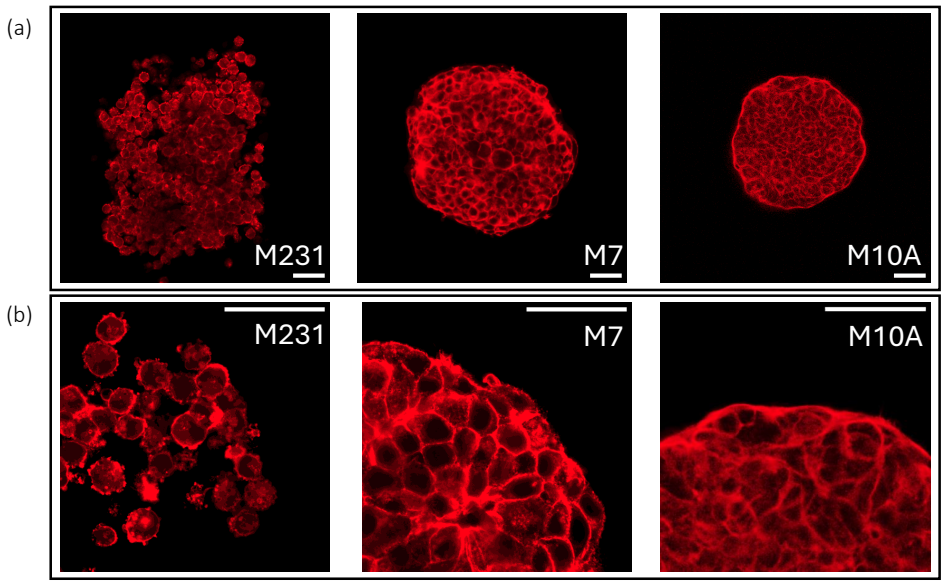

Figure 2.4: **F-actin immunostaining in breast cancer spheroids of different malignancy.** (a) Confocal images (at 20x) of F-actin (at the equitorial plane) in MDA-MB-231, MCF-7 and MCF-10A breast spheroids (from left to right): MCF-10A spheroids display smooth edges with a prominent collective actin rim, MCF-7 spheroids show similar but less pronounced actin rim, while MDA-MB-231 spheroids exhibit fragmented edges lacking a collective actin rim. (b) Same spheroids at higher magnification (63x): MCF-10A cells at the boundary display stretched morphology with compact and smooth actin organization. MCF-7 spheroid edges are similarly compact, but have slightly rougher contours. In contrast, MDA-MB-231 spheroids feature non-interconnected cells with irregular F-actin distribution. Scale bar is 50 μm.

tion compared to healthy spheroids. This translates to a reduced elasticity with higher deformability and reduced viscosity as spheroid malignancy increases. Tissue fluidity, often considered as the opposite of viscosity, has been defined as an indicator of the invasive potential [49]. Healthy spheroids have immobile, jammed cells, and are characterised by an overall lower fluidity, hence higher viscosity. On the contrary, metastatic spheroids display high cell motility and deformability and a disordered, unjammed state [50]. Such feature corroborates the lower viscosity detected for malignant spheroids in our experiments.

During the relaxation phase we identify two distinct time scales for all three spheroid types. Despite the similarity in the bulk properties of both two malignant spheroids (MCF-7 and MDA-MB-231) during compression, we observe distinct behaviors in their relaxation. The early-time fast relaxation, characterized by smaller τ_1 values, is attributed to surface elasticity. Both MCF-7 and MCF-10A spheroids, with their distinct peripheral actin rims and spherical shape, exhibit a faster initial rebound compared to MDA-MB-231 spheroids. Immunostaining of F-actin fibers reveals that this peripheral actin rim

is present in MCF-10A and MCF-7 spheroids, but is absent in MDA-MB-231 spheroids, which exhibit a highly irregular shape, as highlighted in previous studies [51]. This indicates that the structural arrangement of actin fibers significantly influences the early-time relaxation dynamics making the less malignant MCF-7 behave more like the benign MCF-10A spheroid than the highly malignant MDA-MB-231 spheroid. We quantify this surface characteristic through spheroid circularity, which is much closer to 1 for MCF-10A ($\mathscr{C}_r \approx 0.96$) and MCF-7 ($\mathscr{C}_r \approx 1$) than MDA-MB-231 ($\mathscr{C}_r \approx 0.86$). The late-time slow relaxation is correlated with the bulk elasticity (E) values with a shorter τ_2 for the benign MCF-10A than the malignant MCF-7. Notably, we do not observe a dominant viscous effect within the experimental time frame of relaxation (30 minutes), especially for MCF-7 and MCF-10A. Despite MCF-10A spheroids having the highest viscosity among the three types, a longer viscous relaxation timescale is expected, but is not observed in our experiments. The long time viscous effects (beyond experimental time) in MCF-7 spheroids, leading to residual deformation ($\mathscr{S}_{r\infty}$) after the dynamic compression stage, may be linked to changes in E-cadherin-mediated adhesions, which are known to either strengthen or weaken under mechanical stress [52]. Additionally, the mechanical compression could also lead to inhomogeneous cellular rearrangements within the spheroid [25]. A future experiment examining the cellular rearrangement and E-cadherin juncture modification within the MCF-7 spheroid would help understand these long-time effects.

Although MDA-MB-231 shows a τ_2 similar to MCF-7, aligning with their respective elastic moduli, we believe that the relaxation of the former is more complex and is likely influenced by the rearrangement of individual cells. The non-uniform actin distribution in MDA-MB-231 spheroids, seen in Figure 2.4 (also reported earlier in [51, 53]), limits its ability to recover a morphologically compact, circular shape, unlike MCF-7 (see Figures 2.3g and 2.4). This has resulted in a broad range of post-relaxation deformation parameter $\mathscr{S}_{r\infty}$ in MDA-MB-231 spheroids, including values lower than their pre-compression values ($\mathscr{S}_{r0}$) (see Figure 2.3b). We hypothesize that, due to the mesenchymal characteristics of this cell line, cells at the periphery of MDA-MB-231 spheroids exhibit increased mobility (Supporting Movie S2), enhancing the potential for cell-cell rearrangements. These rearrangements are facilitated by the lack of E-cadherin expression in the highly metastatic MDA-MB-231 cells, which is crucial for cell-cell adhesion [54, 55]. This further contributes to the spheroid's loosening during the dynamic compression stage influencing the cell rearrangement during the relaxation [56]. In a separate experiment, an MDA-MB-231 spheroid subjected to high $I_c = 0.87$ fragments during dynamic compression, with individual cells disseminating from the spheroid (see Movie S3). This confirms that spheroids with high metastatic potential (with mesenchymal features) are more prone to deforming irreversibly and breaking, disseminating invasive tumor cells under external physical forces (such as compression), due to unstable cell-cell contact and weak cortical contractility [51].

To summarize, we compare the viscoelastic properties of benign spheroids with malignant spheroids (with low and high metastatic potentials). Notably, the benign spheroids exhibit the highest bulk elasticity, viscosity, and resistance to deformation, in contrast to the two malignant spheroids. We find that both low and high metastatic spheroids have similar apparent viscoelastic properties; however, they differ significantly during

the relaxation phase. Important extension of this work could be the investigation of heterogeneous spheroids to mimic the diverse cellular population within the tumour. From a clinical standpoint, the investigation of the mechanical properties of patient derived biopsy samples (from patients diagnosed by breast cancer) would allow to link them to different stages of metastasis. The microfluidic platform developed in this work provides mechanistic insights into physiological processes, such as cellular remodeling within invasive tumors, and identifies unique "mechanical biomarkers". These biomarkers can be applied in developing therapeutic approaches that target the dissemination of primary solid tumors [6, 7].

2.4. EXPERIMENTAL SECTION

2.4.1. CELL CULTURE AND SPHEROID FORMATION

Human mammary MCF-10A cells (ATCC CRL-10317) were cultured in DMEM/F12 1:1 medium (Gibco) supplemented with 5% horse serum (Gibco), 0.5 μg mL^{-1} hydrocortisone (Sigma), 20 ng mL^{-1} human epidermal growth factor (hEGF) (Peprotech), 100 ng mL^{-1} cholera toxin (Sigma), 10 g mL^{-1} insulin (Human Recombinant Zinc, Gibco) and 1% Penicillin–Streptomycin 100× solution (VWR Life Science). Human mammary MCF-7 mCherry cells and MDA-MB-231 LifeAct GFP (kindly provided by Peter ten Dijke's lab) were cultured in DMEM medium (Gibco) supplemented with 10% fetal bovine serum (Gibco) and 1% antibiotic-antimycotic solution (Gibco). All cells were incubated at 37°C with 5% CO_2 and subcultured at least twice a week. Cells were regularly tested for absence of mycoplasma. Spheroids were formed in a commercially available Corning® Elplasia ® 96-well plate or Sphericallate 5D ® (Kugelmeiers) designed for efficient spheroid production. These plates have a round-bottom shape and a specialized Ultra-Low Attachment (ULA) surface that prevents cells from attaching to the plate and encourages cell-to-cell adhesion. The size of the spheroids depends on factors such as the initial seeding density and the duration of the culture (related to proliferation rate of each cell line). The seeding density was tuned to obtain a spheroid diameter of 200-220 μm after 2 days of culture in the case of MCF-7 and MCF-10A. Due to the lack of cell-cell adhesion (E-cadherin), the MDA-MB-231 spheroids required a separate protocol compared to the other two cells. To promote cell adhesion and spheroid formation for MDA-MB-231 cells, the media was supplemented with methylcellulose (Merck Sigma) in a ratio of 1:4 to promote spheroid compactness [57, 58]. The spheroids were harvested after 5 days. After harvesting, MDA-MB-231 spheroids were resuspended in methylcellulose-free media to ensure the same media viscosity across the three cell lines. We verified that the addition of methylcellulose did not affect the viscoelastic properties using a separate experiment (see Figure S.2.9 in SI).

2.4.2. BLEBBISTATIN TREATMENT

Myosin II inhibitor (-) Blebbistatin (ab120425) was dissolved in dimethyl sulfoxide (DMSO) at a stock concentration of 5 mM. Spheroids were treated with 10 μM blebbistatin for 3 hours before experiments.

2.4.3. SPHEROIDS FIXATION, PERMEABILIZATION, IMMUNOSTAINING AND IMAGING

Spheroids were fixed with 4% paraformaldehyde for 30 min at room temperature (RT) and then permeabilized using 0.1% Triton X-100 (diluted in PBS) at RT for 5 min. For immunostaining, cells were incubated with Phalloidin iFluor 647 Reagent (ab176759) diluted 1:100 in 1% BSA for 90 min at RT. In between all steps, the samples were washed multiple times using PBS. Samples were kept at 4°C, protected from light. Soon after the staining procedure, the spheroids were placed in uncoated chamber wells (ibidi) for visualization of the F-actin organization. Images were acquired on a confocal microscope (LSM 980 with Airyscan 2, Zeiss) equipped with Plan Apochromat 20x/0.8 M27 air objective (to image the whole spheroid) and Plan Apochromat 63x/1.40 Oil DIC M27 objective

for the spheroids' edges (λ_{ex} = 653 nm and λ_{em} = 668 nm). Z-stacks were acquired with a step of 5μm and the equitorial planes were chosen for the visualization of the whole spheroids and their edges. Images post-processing was performed on ImageJ (v1.53t, National Institute of Health, USA).

2.4.4. MICROFLUIDIC CHIP DESIGN AND EXPERIMENTAL SETUP

A 4-inch silicon wafer was used as the base material for the chip, and the fabrication process was carried out in a cleanroom facility (Kavli Nanolab Delft) via a photo-lithography process using the µMLA Laser Writer (Heidelberg Instruments). A detailed procedure of the wafer fabrication can be found in the Supporting Information. Using the master mold as a template, the microfluidic chips were then produced using the soft lithography technique with polydimethylsiloxane (PDMS) as the main material.The day before each experiment, the chips were coated with 1 % bovine serum albumin (BSA, Sigma Aldrich) in DPBS buffer solution to reduce friction of the spheroids with the channel walls. The chips were kept overnight at 37°C and with sufficient humidity. The day of the experiment the chips were flushed with DPBS to remove BSA extra residues and eventual dirt. The three serpentines positioned at the inlet allow for the stabilization of the flow when the spheroid enters the chip, whereas the last serpentine is strategically utilized to impede the spheroid's exit, ensuring its prolonged residence in the relaxation chamber. The height of the chip (180±15 μm) is uniform along the whole design. To prevent the tumbling of the spheroids, we selected spheroids with a higher diameter than the height of the chip. This allows for a pre-compression of the spheroid in the z-axis, enabling subsequent observations and measurements to be conducted within the recording x-y plane. This also implies the clogging of the flow when the spheroids enter the constriction, excluding possibilities of shear flow between the spheroids and the channel walls. The microfluidic chips have been fabricated with different constriction widths (60-65 μm, 84-94 μm and 100-110 μm). The experimental setup consists of a 200 μL pipette tip plugged into the inlet for the spheroids loading, while at the outlet a tube is connected to an In-Line pressure sensor, S version (Fluigent) for a continuous measurement of pressure. Additionally, a syringe pump (Harvard Apparatus, Pump 11 Pico Plus Elite) operating in withdrawal mode (4 μL min^{-1}) is used to ensure constant fluid flow and enable the spheroids to pass through the constriction in a controlled manner. When the spheroid exits the constriction the withdrawal flow rate is immediately set to zero, allowing to keep the spheroid within the relaxation chamber. The spheroids are individually loaded into the pipette tip at the inlet, together with the cell culture media, one at a time, to prevent flow and pressure instability given by the traverse of two or more spheroids in the microfluidic chip. Experiments that had more than one spheroid flowing in the chip were not considered in the analysis. All experiments were conducted at 37°C through a Heating Insert (ibidi). The inlet reservoir precluded the use of a lid for humidity and CO_2 control.

2.4.5. DATA ACQUISITION AND ANALYSIS

Brightfield images of the spheroids entering the constricted channels were captured on an inverted fluorescence microscope (Zeiss Axio-Observer) with camera streaming (for the compression stage) using a 5×/NA 0.16 air objective and Zeiss Axio-Observer 0.63x

digital camera with a resolution of 2048x2048 μm^2. Once the spheroid exited the constriction, the syringe pump was paused to allow the spheroid to reside in the chamber. For the relaxation phase, images were taken at 2 fps for the first 10 minutes, and successively at 0.1 fps for the remaining 20 minutes, for a total of 30 minutes of relaxation recording in the same imaging conditions as during the compression. To analyze the dynamic compression data, an image without the spheroid was subtracted from the image containing the spheroid to remove all background noise and identify the spheroid contour (edges in red in Figure 2.1b). The image was then converted to binary format, and morphological closing was applied to remove the rough edges from the boundary of the spheroid. To determine the spheroid axial dimensions prior to (D_0) and during compression (D(t)), a MATLAB function that detects the minimum and maximum pixel values in the horizontal direction was used. The velocity (u) of the spheroid was calculated by first identifying the centroid (using regionprops function in MATLAB) and then averaging the displacements of the centroid for consecutive images according to the Δt from one image to the other. For the relaxation, given the variable orientation of the spheroid in the relaxation chamber, it was not possible to implement the same function used for the dynamic compression to detect the length of the deformed spheroid. Therefore, an ellipse fitting was used and its major and minor axes (white lines in Figure 2.1c) were detected to calculate the deformation parameter $\mathscr{S}_r$.

2.4.6. PRESSURE CHARACTERIZATION AND D3M MODEL

The spheroid entering the constriction clogged the fluid flow, causing the volumetric flow rate in the channel to go to zero. However, the withdrawal force applied by the syringe pump remained constant, causing an increase in the pressure in the constriction, detected by the pressure sensor located at the outlet. The sensor recorded a linear pressure increase, meaning that the stress experienced by the spheroid linearly increased during the compression phase (Figure 2.2a). The deformation of the spheroid in the main constriction is fitted by the Dynamic Modified Maxwell Model (D3M), up to the inflex point of the strain curve, corresponding to the time t_2. The model considers the pressure as an affine line, rather than a constant value as the Modified Maxwell Model (MMM), used for conventional MPA experiments. The two models share the same schematic, but the governing equations are different because of the time dependence of the pressure.

The general governing equation is given by (for full derivation refer to Supporting Information):

$$\ddot{\varepsilon} + \frac{\dot{\varepsilon}}{\tau_c} = \left(\frac{1}{E\tau_c} + \frac{1}{\eta}\right)\dot{\sigma} + \frac{1}{\eta\tau_c}\sigma \tag{2.4}$$

with $\tau_c = \frac{\eta^*(E^*+E)}{E^*E}$

The initial conditions for the stress and strain are the following:

$$\sigma(0) = \Delta P_0 \tag{2.5}$$

$$\dot{\sigma}(0) = \Delta \dot{P} \tag{2.6}$$

$$\epsilon(0) = \frac{\Delta P_0}{E^* + E} \tag{2.7}$$

$$\dot{\epsilon}(0) = \frac{\Delta \dot{P}}{E^* + E} + \frac{E^{*2} \Delta P_0}{\eta^* (E^* + E)^2} + \frac{\Delta P_0}{\eta} \tag{2.8}$$

The resolution of the differential equation gives us:

$$\dot{\epsilon}(t) = \frac{\Delta P_0}{\tau_c} \frac{e^{-\frac{t}{\tau_c}}}{E_{(1,2)}} + \frac{\Delta \dot{P} t + \Delta P_0}{E} \tag{2.9}$$

with $E_{(1,2)} = \frac{E_2(E_1+E_2)}{E_1}$

2.4.7. STATISTICAL ANALYSIS

The solid line in the boxplots represents the median value. The box edges indicate the interquartile range (IQR), spanning from the 25^{th} percentile (Q_1) to the 75^{th} percentile (Q_3). The dotted whiskers are within 1.5 times the IQR from the quartile. Outliers are represented by individual markers outside the dotted whiskers range. All statistical analysis was performed using Microsoft Excel (Microsoft Corporation, USA) and MATLAB. The statistical significant differences between the experimental groups were determined by Student t-test using the function t-test: two-tailed distribution with unequal variance and p values below 0.05 were considered to be significant. We categorize statistical differences as following: $p < 0.001$ (***), $p < 0.01$ (**) and $p < 0.05$ (*).

AUTHOR CONTRIBUTIONS

M. T., A. D. B. and P. E. B. conceived the ideas and designed the experiments. M. T. , E. T. , S. D. carried out the experiments and collected the data. M. T. and A. D. B. performed data and image analysis. A. D. B. developed MATLAB codes for image analysis. E.T., A.D.B. and M.T. developed the model. M. T. wrote the paper and A. D. B., V. G. and P. E. B. edited it.

ACKNOWLEDGEMENTS

The authors thank Peter ten Dijke (from Leiden University Medical Center) for kindly providing MCF-7 mCherry and MDA-MB-231 LifeAct GFP cells. M.T. and P. E. B. gratefully acknowledge funding from the European Research Council (ERC) under the European Union's Horizon 2020 research and innovation program (grant agreement no. 819424). A. D. B. gratefully acknowledges funding from MSCA Postdoctoral Fellowships 2022 Project ID: 101111247. E.T. was supported by an Erasmus+ Traineeship.

SUPPLEMENTARY INFORMATION

2.A. DETAILS ABOUT MICROFLUIDIC CHIP FABRICATION

The master wafer was fabricated by a standard photo-lithography technique using the μMLA laserwriter (Heidelberg Instruments) on a 4-inch silicon wafer at the Kavli Nanolab Delft. Firstly, SU-8 2100 (Kayaku Advanced Materials) negative photoresist was spin-coated in two steps:

- 500 rpm for 10 seconds with an acceleration of 100 rpm/s
- 1850 rpm for 30 seconds with an acceleration of 300 rpm/s

The silicon-wafer with SU-8 was soft-baked at 65 °C for 5 minutes then at 95 °C for 30 minutes. The wafer was then inserted in the laser writer holder for printing using a 365mn laser source. Details of the AutoCAD design can be found here —. After laser printing, the wafer was post baked at 65 °C for 5 minutes, followed by 95 °C for 12 minutes and developed in SU- 8 photo-resist developer (mr-Dev 600, Micro resist technology or PGMEA, Sigma Aldrich). After development, a hard bake at 150°C for 5 minutes ensured better defined patterns. The photolithography procedure was optimized to achieve a final channel height of 180 ± 15 μm. The height of the channels was determined by a Dektak profilometer. The master wafer was coated with trichloro(1H,1H,2H,2H-perfluorooctyl)silane to create a hydrophobic surface for easy demoulding. Polydimethylsiloxane (PDMS, Sylgard 184) based microfluidic chips were prepared using the mixture of PDMS and curing agent with a ratio of 10:1. Individual chips were then cut out and inlets/outlets were punched in the PDMS slab for tube fitting (PTFE, inner diameter: 0.3mm, outer diameter: 1.6mm). Final bonding was performed by plasma cleaning (Harrick Plasma) of the PDMS slab and a glass coverslip (#1.5) for two 2 minutes 20 seconds to facilitate final bonding. Finally, the assembled device was kept in the oven at 70 °C for at least 20 minutes to facilitate bonding strength. Afterward, the microfluidic devices can be stored indefinitely.

2.B. DERIVATION OF THE DYNAMIC MODIFIED MAXWELL MODEL

The schematic of the model is the following:

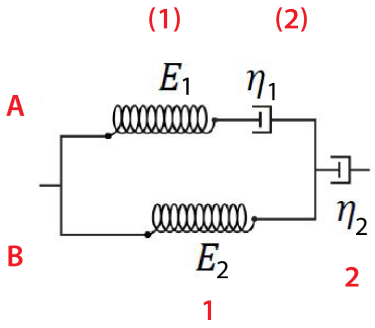

For the springs in the model Hooke's law applies:

$$\sigma = E\epsilon$$

The dashpots follow Newton's law for Newtonian fluids, where

$$\sigma = \eta\dot{\epsilon}$$

Based on these, we have the following equations

$$\sigma_B = E_2\epsilon_B \tag{1}$$

$$\sigma_A = E_1\epsilon_A^{(1)} = \eta_1\dot{\epsilon}_A^{(2)} \tag{2}$$

$$\epsilon_1 = \epsilon_A = \epsilon_B \tag{3}$$

$$\epsilon_A = \epsilon_A^{(1)} + \epsilon_A^{(2)} \tag{4}$$

From Equation (3) and Equation(2),it can be written respectively

$$\sigma_A = E_1\epsilon_A - \epsilon_A^{(2)} \tag{5}$$

$$\dot{\sigma}_A = E_1\left(\dot{\epsilon}_A - \frac{\sigma_A}{\eta_1}\right) \tag{6}$$

With

$$\sigma_1 = \sigma_A = \sigma_B \tag{7}$$

and therefore

$$\dot{\sigma}_1 = \dot{\sigma}_A = \dot{\sigma}_B$$

leads to

$$\dot{\sigma}_1 = E_1\left(\dot{\epsilon}_1 - \frac{\sigma_A}{\eta_1}\right) + E_2\dot{\epsilon}_1 \tag{8}$$

By implementing Equation (7) into the first term:

$$\dot{\sigma}_1 = E_1\left(\dot{\epsilon}_1 - \frac{1}{\eta_1}(\sigma_1 - E_2\epsilon_1)\right) + E_2\dot{\epsilon}_1 \tag{9}$$

$$\dot{\sigma}_1 = E_1\dot{\epsilon}_1 - \frac{E_1}{\eta_1}\sigma_1 + \frac{E_1E_2}{\eta_1}\epsilon_1 + E_2\dot{\epsilon}_1 \tag{10}$$

Given that $\sigma = \sigma_1 = \sigma_2$ and $\epsilon = \epsilon_1 + \epsilon_2$, we have that $\epsilon_1 = \epsilon$ - ϵ_2. Equation (10) can be rewritten as

$$\dot{\sigma}_1 = E_1\dot{\epsilon} - E_1\dot{\epsilon}_2 - \frac{E_1}{\eta_1}\sigma + \frac{E_1E_2}{\eta_1}(\epsilon - \epsilon_2) + E_2\dot{\epsilon} - E_2\dot{\epsilon}_2 \tag{11}$$

Considering the second derivative of the stress σ_1 (which is 0) and rewriting the equation with the strain terms on the left side and the stress on the right side of the equation, we obtain:

$$\ddot{\epsilon} + \frac{E_1 E_2}{(E_1+E_2)} \frac{1}{\eta_1} \dot{\epsilon} = \frac{1}{(E_1+E_2)} \left(\frac{E_1}{\eta_1} + \frac{E_1}{\eta_2} + \frac{E_2}{\eta_2} \right) \dot{\sigma} + \frac{E_1 E_2}{(E_1+E_2)} \frac{1}{\eta_1 \eta_2} \sigma \tag{12}$$

This equation can be rewritten as the following

$$\ddot{\epsilon} + \frac{\dot{\epsilon}}{\tau_c} = \left(\frac{1}{E_2 \tau_c} + \frac{1}{\eta_2} \right) \dot{\sigma} + \frac{1}{\eta_2 \tau_c} \sigma \tag{13}$$

With $\tau_c = \frac{\eta_1 (E_1+E_2)}{E_1 E_2}$

This is the constitutive equation of the model that will be solved with the appropriate initial conditions.

Solving the differential equation with initial conditions

For the stress on the spheroid, the following expression is used:

$$\sigma(t) = \Delta P(t) = at + \Delta P_0$$

To simplify, $\sigma = at + b$ and therefore $\dot{\sigma} = a$

By substituting these two formulas in Equation (13):

$$\ddot{\epsilon} + \frac{\dot{\epsilon}}{\tau_c} = \left(\frac{1}{E_2 \tau_c} + \frac{1}{\eta_2} \right) a + \frac{a}{\eta_2 \tau_c} t + \frac{b}{\eta_2 \tau_c}$$

The following initial conditions are used to solve this differential equation:

$$1. \sigma(0) = \Delta P_0$$

$$2. \dot{\sigma}(0) = \dot{\Delta P} = a$$

$$3. \epsilon(0) = \frac{\Delta P_0}{E_1 + E_2}$$

$$4. \dot{\epsilon}(0) = \frac{a}{E_1 + E_2} + \frac{E_1^2 \Delta P_0}{\eta_1 (E_1+E_2)^2} + \frac{\Delta P_0}{\eta_2}$$

The last initial condition is obtained by solving:

$$\dot{\epsilon}(0) = \dot{\epsilon}_1(0) + \dot{\epsilon}_2(0)$$

with

$$\dot{\epsilon}_2(0) = \frac{\sigma(0)}{\eta_2} = \frac{b}{\eta_2}$$

and

$$\dot{\epsilon}_1(0)$$

is derived from rewriting Equation (10) and substituting the first two initial conditions.

The homogeneous solution for the strain derivative is

$$\dot{\epsilon}(t) = Ce^{-t/\tau_c}$$

From Equation(13) the particular solution is:

$$\ddot{\epsilon} = \frac{a}{\eta_2} \quad \text{and} \quad \dot{\epsilon} = \frac{a}{\eta_2}t + \frac{a}{E_2} + \frac{b}{\eta_2}$$

By combining the homogeneous and particular solution:

$$\dot{\epsilon}(t) = Ce^{-t/\tau_c} + \frac{at+b}{\eta_2} + \frac{a}{E_2} \tag{14}$$

By substituting first the 4. Initial condition, the constant C is obtained from the homogeneous solution:

$$C = \frac{E_1}{E_2(E_1+E_2)}\left(\frac{b}{\tau_c} - a\right)$$

By defining

$$E_{(1,2)} = \frac{E_2(E_1+E_2)}{E_1}$$

and substituting the value of the constant C in Equation(14):

$$\dot{\epsilon}(t) = \frac{1}{\tau_c}\frac{b}{E_{(1,2)}}e^{-t/\tau_c} - \frac{a}{E_{(1,2)}}e^{-t/\tau_c} + \frac{at+b}{\eta_2} + \frac{a}{E_2} \tag{15}$$

By integrating Equation(15) into the following:

$$\epsilon(t) = -\frac{b}{E_{(1,2)}}e^{-t/\tau_c} + \frac{a\tau_c}{E_{(1,2)}}e^{-t/\tau_c} + \frac{a}{2\eta_2}t^2 + \frac{bt}{\eta_2} + \frac{at}{E_2} + D \tag{16}$$

Implementation of the 3. Initial condition provides the value of the constant D:

$$D = \frac{b}{E_2} - \frac{a\eta_1}{E_2^2}$$

By substituting the value of D and rewriting

$$a = \Delta\dot{P}, \quad E_1 = E^*, \quad E_2 = E, \quad \eta_1 = \eta^*, \quad \eta_2 = \eta$$

the following equation is obtained:

$$\epsilon(t) = \frac{\Delta P_0}{E}\left(1 - \frac{E^*}{E^*+E}e^{-t/\tau_c}\right) + \frac{\Delta P_0 t}{\eta} + \frac{\Delta\dot{P}t}{E} + \frac{\Delta\dot{P}t^2}{2\eta} + \frac{\Delta\dot{P}\eta^*}{E^2}\left(e^{-t/\tau_c} - 1\right) \tag{17}$$

which is the final equation of the Dynamic Modified Maxwell Model.

2.C. SUPPLEMENTARY FIGURES

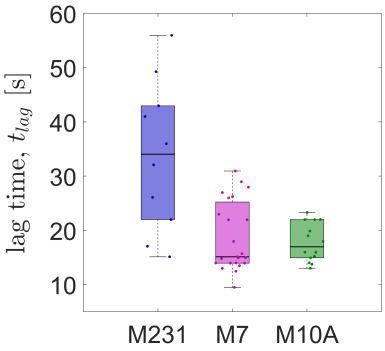

Figure S.2.1: **Lag time before relaxation monitoring.** Boxplots displaying the lag time for the three spheroid types. The lag time marks the time difference between the maximum strain experienced by the spheroid (before exiting the constriction channel) and the start of the relaxation recording. It denotes the time required for the spheroid to traverse the final serpentine and reach the relaxation chamber.

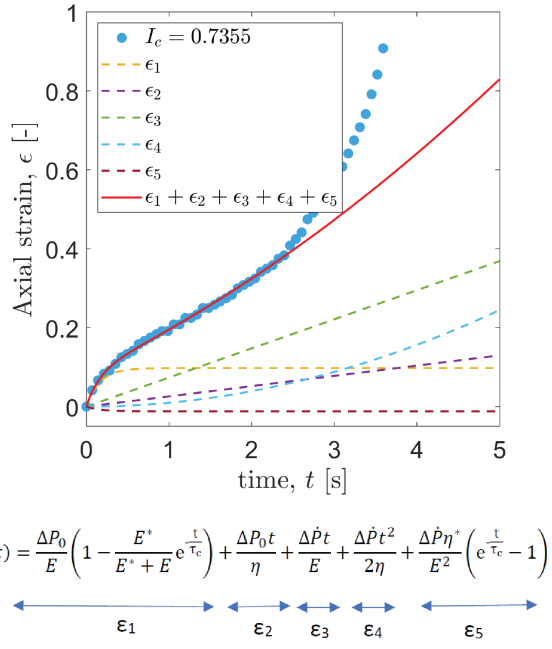

Figure S.2.2: **Decomposition of the constitutive equation of the D3M.** The red solid line shows the fitting of the D3M for an MCF-7 spheroid of $I_c = 0.7355$. The fitting stops at the inflex point, corresponding to the timepoint τ_2 as described in the main text. The dotted lines show the contribution of each term of the constitutive equation of the D3M, highlighting that the contribution of the last exponential term is very small.

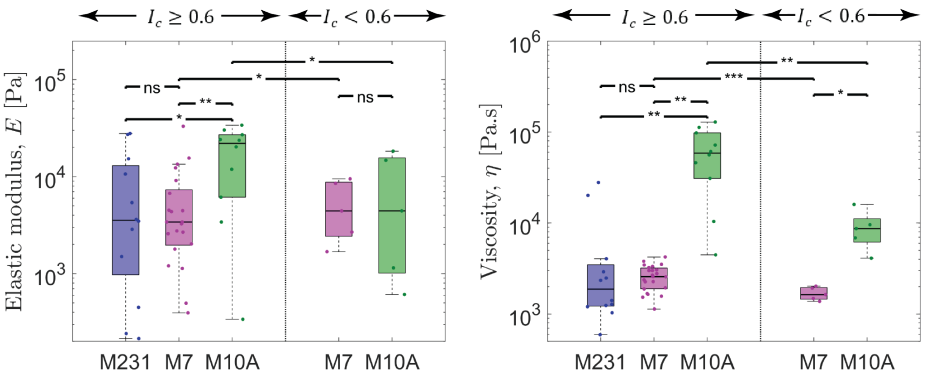

Figure S.2.3: **Spheroid viscoelastic properties extracted from 3M.** Left: Bulk elastic modulus for the three spheroid types extracted from the fitting of the Modified Maxwell Model (3M). MCF-10A spheroids display higher bulk elasticity, compared to MCF-7 and MDA-MB-231 spheroids, with comparable values to the ones extracted from the D3M. Right: Viscosity for the three spheroid types extracted from the fitting of the Modified Maxwell Model (3M). The trend is similar to the one observed from the D3M, with MCF-10A displaying higher viscosity compared to the malignant spheroids.

Model	Coefficient of Determination (R^2)		
	MD-MB-231	**MCF-7**	**MCF-10A**
Dynamic Modified Maxwell Model	0.9922	0.9966	0.9939
Modified Maxwell Model	0.98815	0.9893	0.9913

Table S.2.1: **Comparison of the values of the coefficient of determination R^2 for 3DM and 3M.** The values reported represent the median value of the coefficient of determination R^2 for all the fittings reported in both Figure 2e,f and Figure S.2.3. The 3DM shows a higher coefficient of determination compared to 3M for all three spheroid types.

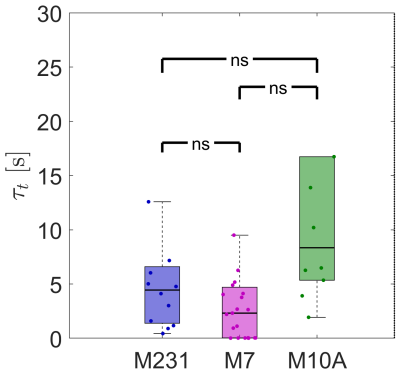

Figure S.2.4: **Tissue transition time.**The transition time τ_t , defined as η/E, describes the transition of the tissue from the elastic regime to the viscous regime during compression. MCF-10A spheroids show the longest transition time among the spheroids, suggesting a more predominant elastic contribution in the first stages of the dynamic compression for the benign spheroids.

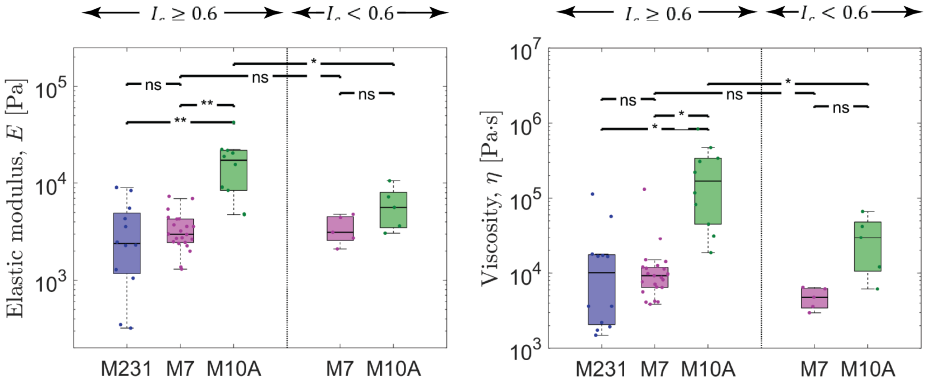

Figure S.2.5: **Bulk elastic moduli and viscosity for different I_c ranges.** Bulk elastic modulus (left figure) and viscosity (right figure) for the three spheroid types for two ranges of I_c. MCF-10A spheroids display viscoelastic properties that are dependent on the level of compression, with higher E and η as the compression increases ($I_c \geq 0.6$). MCF-7 spheroids, instead, do not show any statistical differences in their viscoelastic properties across different I_c values. The distinction between benign and malignant spheroids disappears at lower levels of compression, indicating that the differences between them become discernible only above a certain threshold of stress or confinement.

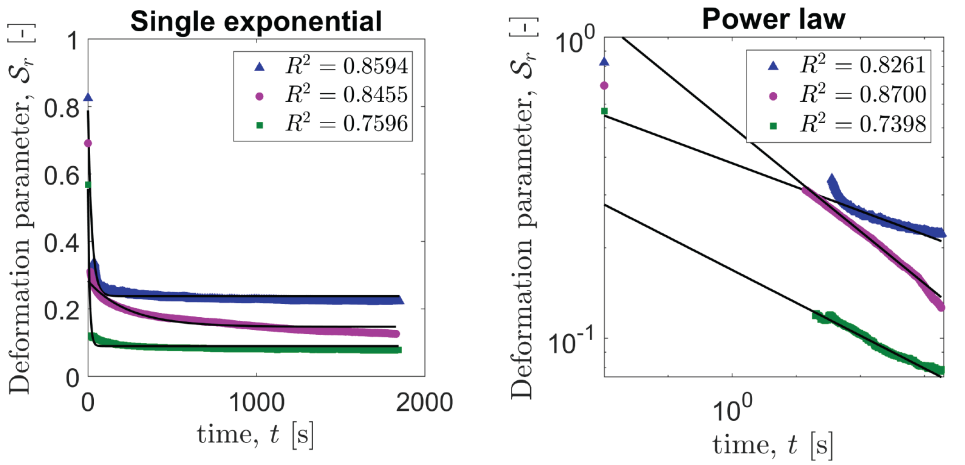

Figure S.2.6: **Relaxation curves fitting a single exponential and power law equations.** Showcases of relaxation curves fitted with a single exponential (left) and power law (right, in log-log scale) equations. The coefficients of determination R^2 are outlined in the legends, highlighting that the double exponential model describes better the deformation parameter curves (with $R^2 > 0.98$) via the two characteristic timescales.

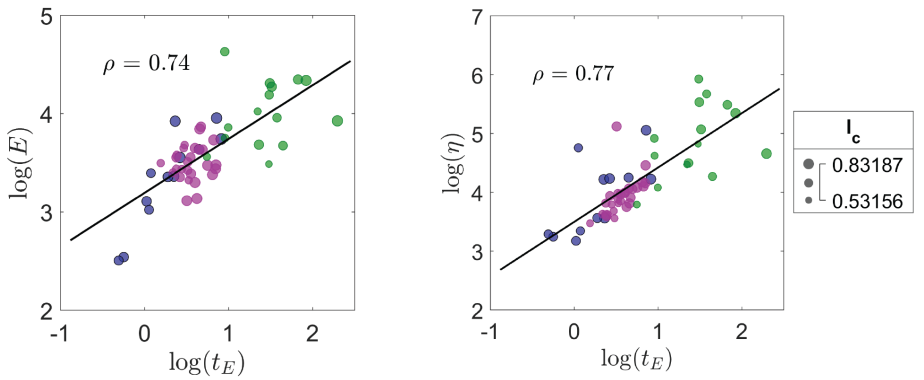

Figure S.2.7: **Bubble charts correlating entry time t_E, bulk elasticity E, viscosity η and Constriction Index I_c.** The colours correspond to the spheroid type: blue for MDA-MB-231, magenta for MCF-7 and green for MCF-10A. The bubble size increases with higher Constriction Index values. Left figure: Bubble chart showing the strong correlation (Pearson coefficient ρ = 0.74) between the entry time and the bulk elasticity E of the aggregates, distinguished by spheroid type and I_c value. MCF-10A show higher bulk elasticity, corresponding to higher entry times, independently from the Constriction Index. Right figure: Bubble chart showing the strong correlation (ρ = 0.77) between the entry time and the aggregates viscosity η, confirming the hypothesis that more viscous spheroids require longer time to deform and squeeze in the constricted channel. Smaller I_c values correspond to lower entry time t_E and for MCF-10A spheroids lower I_c translates in lower viscosity values, as shown in Figure S.2.5.

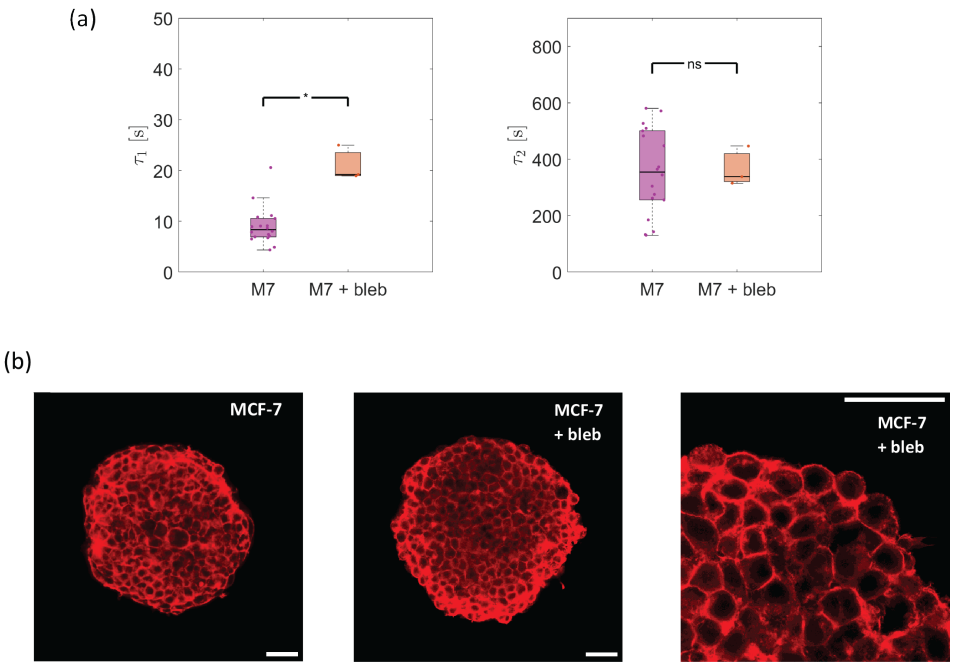

Figure S.2.8: **Relaxation timescales of MCF-7 spheroids, blebbistatin-treated MCF-7 spheroids and F-actin immunostaining.** (a) Short (τ_1) and long (τ_2) timescales of relaxation of MCF-7 spheroids and MCF-7 spheroids treated with 10μM blebbistatin for 3 hours. The inhibition of the actomyosin contractility with blebbistatin results in a higher τ_1, associated with decreased surface elasticity, whereas the long timescale τ_2 is unaltered. (b) Confocal images of F-actin distribution (at the equatorial plane) in untreated MCF-7 spheroid (left, 20x magnification) and blebbistatin treated MCF-7 spheroid (middle and right picture, 20x and 63x magnification respectively). The spheroid edges appear to be rougher in the MCF-7 + blebbistatin spheroid compared to the untreated MCF-7, suggesting that altering the peripheral actin rim impacts the fast relaxation phase.

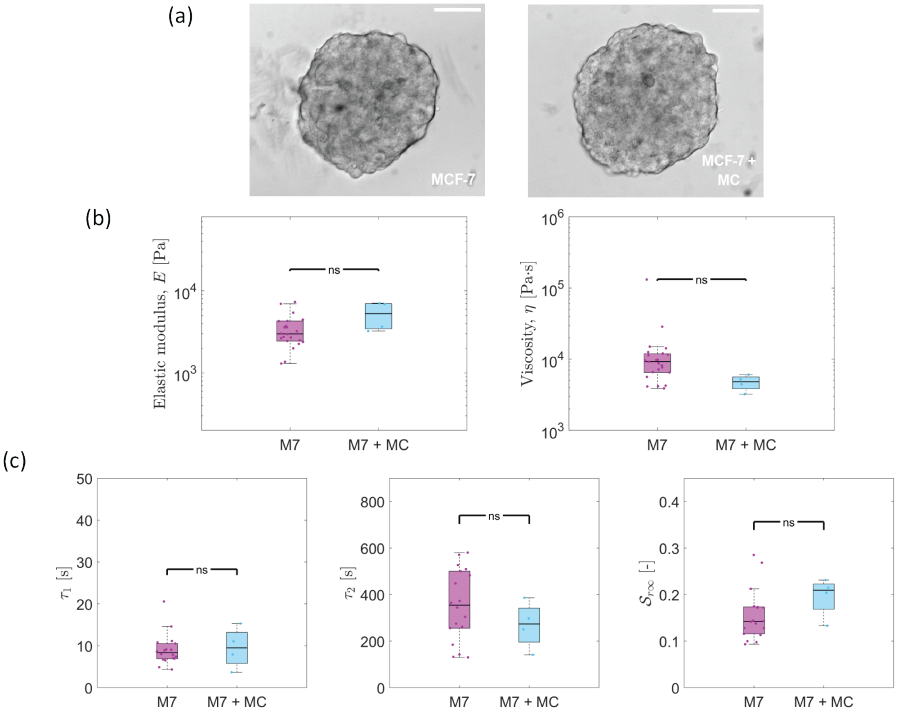

Figure S.2.9: **Methylcellulose (MC) does not affect spheroid viscoelasticity.** (a) Brightfield images of MCF-7 spheroids formed in Elplasia 96-well plate in conventional media (left) and in methylcellulose (MC) + conventional media. The addition of MC does not affect the spheroid morphology. Scale bar: 100 μm. (b) Boxplots comparing the bulk elastic moduli (E) and viscosity (η) of MCF-7 spheroids and MCF-7 spheroids formed with MC. (c) Boxplots comparing relaxation timescales τ_1, τ_2, and residual deformation (S_∞) of MCF-7 spheroids and MCF-7 spheroids formed with MC. No statistical significance in the viscoelastic properties and the relaxation dynamics is present, suggesting that MC does not affect the spheroid behavior.

2.D. SUPPLEMENTARY MOVIES

Movie S1. Dynamic compression and deformation of MDA-MB-231, MCF-7 and MCF-10A spheroids respectively.

Movie S2. Relaxation of MDA-MB-231, MCF-7 and MCF-10A spheroids respectively.

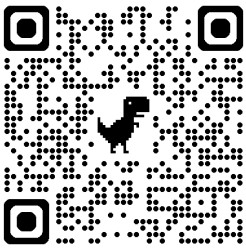

Movie S3. Breakage and cell dissemination of MDA-MB-231 spheroid during dynamic compression and deformation.

REFERENCES

[1] M. Tavasso, A. D. Bordoloi, E. Tanré, S. A. Dekker, V. Garbin, and P. E. Boukany, *Linking Metastatic Potential and Viscoelastic Properties of Breast Cancer Spheroids via Dynamic Compression and Relaxation in Microfluidics,* Advanced Healthcare Materials **14** (2024), 10.1002/adhm.202402715.

[2] D. Wirtz, K. Konstantopoulos, and P. C. Searson, *The physics of cancer: The role of physical interactions and mechanical forces in metastasis,* Nature Reviews Cancer **11**, 512 (2011).

[3] E. Cambria, M. F. Coughlin, M. A. Floryan, G. S. Offeddu, S. E. Shelton, and R. D. Kamm, *Linking cell mechanical memory and cancer metastasis,* Nature Reviews Cancer **24**, 216 (2024).

[4] H. T. Nia, L. L. Munn, and R. K. Jain, *Physical traits of cancer,* Science **370**, eaaz0868 (2020).

[5] V. Gensbittel, M. Kräter, S. Harlepp, I. Busnelli, J. Guck, and J. G. Goetz, *Mechanical Adaptability of Tumor Cells in Metastasis,* Developmental Cell **56** (2021), 10.1016/j.devcel.2020.10.011.

[6] A. Massey, J. Stewart, C. Smith, C. Parvini, M. McCormick, K. Do, and A. X. Cartagena-Rivera, *Mechanical properties of human tumour tissues and their implications for cancer development,* Nature Reviews Physics **6**, 269 (2024).

[7] W. Yu, S. Sharma, E. Rao, A. C. Rowat, J. K. Gimzewski, D. Han, and J. Rao, *Cancer cell mechanobiology: a new frontier for cancer research,* Journal of the National Cancer Center **2** (2022), 10.1016/j.jncc.2021.11.007.

[8] S. E. Cross, Y. S. Jin, J. Rao, and J. K. Gimzewski, *Nanomechanical analysis of cells from cancer patients,* Nature Nanotechnology **2**, 780 (2007).

[9] C. Rianna, M. Radmacher, and S. Kumar, *Direct evidence that tumor cells soften when navigating confined spaces,* Molecular Biology of the Cell **31**, 1726 (2020).

[10] H. W. Hou, Q. S. Li, G. Y. Lee, A. P. Kumar, C. N. Ong, and C. T. Lim, *Deformability study of breast cancer cells using microfluidics,* Biomedical Microdevices **11**, 557 (2009).

[11] H. A. Cognart, J. L. Viovy, and C. Villard, *Fluid shear stress coupled with narrow constrictions induce cell type-dependent morphological and molecular changes in SK-BR-3 and MDA-MB-231 cells,* Scientific Reports **10** (2020), 10.1038/s41598-020-63316-w.

[12] Z. Yan, X. Xia, W. C. Cho, D. W. Au, X. Shao, C. Fang, Y. Tian, and Y. Lin, *Rapid Plastic Deformation of Cancer Cells Correlates with High Metastatic Potential,* Advanced Healthcare Materials **11** (2022), 10.1002/adhm.202101657.

[13] P. Shah, C. M. Hobson, S. Cheng, M. J. Colville, M. J. Paszek, R. Superfine, and J. Lammerding, *Nuclear Deformation Causes DNA Damage by Increasing Replication Stress,* Current Biology **31**, 753 (2021).

[14] T. Fuhs, F. Wetzel, A. W. Fritsch, X. Li, R. Stange, S. Pawlizak, T. R. Kießling, E. Morawetz, S. Grosser, F. Sauer, J. Lippoldt, F. Renner, S. Friebe, M. Zink, K. Bendrat, J. Braun, M. H. Oktay, J. Condeelis, S. Briest, B. Wolf, L. C. Horn, M. Höckel, B. Aktas, M. C. Marchetti, M. L. Manning, A. Niendorf, D. Bi, and J. A. Käs, *Rigid tumours contain soft cancer cells,* Nature Physics **18**, 1510 (2022).

[15] N. V. Popova and M. Jücker, *The Functional Role of Extracellular Matrix Proteins in Cancer,* Cancers **14** (2022), 10.3390/cancers14010238.

[16] A. Elosegui-Artola, A. Gupta, A. J. Najibi, B. R. Seo, R. Garry, C. M. Tringides, I. de Lázaro, M. Darnell, W. Gu, Q. Zhou, D. A. Weitz, L. Mahadevan, and D. J. Mooney, *Matrix viscoelasticity controls spatiotemporal tissue organization,* Nature Materials **22**, 117 (2023).

[17] A. Aung, S. K. Davey, J. Theprungsirikul, V. Kumar, and S. Varghese, *Deciphering the Mechanics of Cancer Spheroid Growth in 3D Environments through Microfluidics Driven Mechanical Actuation,* Advanced Healthcare Materials **12** (2022), 10.1002/adhm.202201842.

[18] W. Kang, J. Ferruzzi, C.-P. Spatarelu, Y. L. Han, Y. Sharma, S. A. Koehler, J. A. Mitchel, A. Khan, J. P. Butler, D. Roblyer, M. H. Zaman, J.-A. Park, M. Guo, Z. Chen, A. F. Pegoraro, and J. J. Fredberg, *A novel jamming phase diagram links tumor invasion to non-equilibrium phase separation,* iScience **24** (2021), 10.1016/j.isci.2021.103252.

[19] K. S. Kopanska, Y. Alcheikh, R. Staneva, D. Vignjevic, and T. Betz, *Tensile forces originating from cancer spheroids facilitate tumor invasion,* PLoS ONE **11** (2016), 10.1371/journal.pone.0156442.

[20] M. Kalli and T. Stylianopoulos, *Defining the role of solid stress and matrix stiffness in cancer cell proliferation and metastasis,* Frontiers in Oncology **8** (2018), 10.3389/fonc.2018.00055.

[21] Z. Rahman, A. D. Bordoloi, H. Rouhana, M. Tavasso, G. van der Zon, V. Garbin, P. ten Dijke, and P. E. Boukany, *Interstitial flow potentiates TGF-β/Smad-signaling activity in lung cancer spheroids in a 3D-microfluidic chip,* Lab on a Chip **24** (2023), 10.1039/d3lc00886j.

[22] K. Jiang, L. Liang, and C. T. Lim, *Engineering confining microenvironment for studying cancer metastasis,* iScience **24** (2024), 10.1016/j.isci.

[23] R. C. Boot, A. Roscani, L. van Buren, S. Maity, G. H. Koenderink, and P. E. Boukany, *High-throughput mechanophenotyping of multicellular spheroids using a microfluidic micropipette aspiration chip,* Lab on a Chip **23** (2023), 10.1039/d2lc01060g.

[24] S. L. Tlili, F. Graner, and H. Delanoë-Ayari, *A microfluidic platform to investigate the role of mechanical constraints on tissue reorganization,* Development **149** (2022), 10.1242/dev.200774.

[25] S. Jain, H. Belkadi, A. Michaut, S. Sart, J. Gros, M. Genet, and C. N. Baroud, *Using a micro-device with a deformable ceiling to probe stiffness heterogeneities within 3D cell aggregates,* Biofabrication **16** (2024), 10.1088/1758-5090/ad30c7.

[26] I. Pajic-Lijakovic, *Viscoelasticity and Collective Cell Migration: An Interdisciplinary Perspective Across Levels of Organization* (Elsevier, 2021) pp. 21–46.

[27] G. S. Oostenbrug, R. P. Mensink, M. R. Hardeman, T. De Vries, F. Brouns, and G. Hornstra, *Exercise performance, red blood cell deformability, and lipid peroxidation: Effects of fish oil and vitamin E,* Journal of Applied Physiology **83**, 746 (1997).

[28] D. Bento, R. O. Rodrigues, V. Faustino, D. Pinho, C. S. Fernandes, A. I. Pereira, V. Garcia, J. M. Miranda, and R. Lima, *Deformation of red blood cells, air bubbles, and droplets in microfluidic devices: Flow visualizations and measurements,* Micromachines **9** (2018), 10.3390/mi9040151.

[29] K. Matthews, E. S. Lamoureux, M. E. Myrand-Lapierre, S. P. Duffy, and H. Ma, *Technologies for measuring red blood cell deformability,* Lab on a Chip **22**, 1254 (2022).

[30] K. Guevorkian, M. J. Colbert, M. Durth, S. Dufour, and F. Brochard-Wyart, *Aspiration of biological viscoelastic drops,* Physical Review Letters **104** (2010), 10.1103/PhysRevLett.104.218101.

[31] K. Guevorkian, D. Gonzalez-Rodriguez, C. Carlier, S. Dufour, and F. Brochard-Wyart, *Mechanosensitive shivering of model tissues under controlled aspiration,* 10.1073/pnas.1105741108/-/DCSupplemental.

[32] K. Guevorkian, F. Brochard-Wyart, and D. Gonzalez-Rodriguez, *Flow dynamics of 3D multicellular systems into capillaries,* in *Viscoelasticity and Collective Cell Migration: An Interdisciplinary Perspective Across Levels of Organization* (Elsevier, 2021) pp. 193–223.

[33] M. Yu, A. Mahtabfar, P. Beelen, Y. Demiryurek, D. I. Shreiber, J. D. Zahn, R. A. Foty, L. Liu, and H. Lin, *Coherent Timescales and Mechanical Structure of Multicellular Aggregates,* Biophysical Journal **114**, 2703 (2018).

[34] P. Marmottant, A. Mgharbel, J. Kä Fer, B. Audren, J.-P. Rieu, J.-C. Vial, B. Van Der Sanden, A. F. M. Maré E D, F. Graner, and H. Lè Ne Delanoë Ayari, *The role of fluctuations and stress on the effective viscosity of cell aggregates,* , 17271 (2009).

[35] R. Ferraro, S. Caserta, and S. Guido, *A Low-Cost, User-Friendly Rheo-Optical Compression Assay to Measure Mechanical Properties of Cell Spheroids in Standard Cell Culture Plates,* Advanced Materials Technologies **9** (2024), 10.1002/admt.202301890.

[36] X. Xie, F. Sauer, S. Grosser, J. Lippoldt, E. Warmt, A. Das, D. Bi, T. Fuhs, and J. A. Käs, *Effect of non-linear strain stiffening in eDAH and unjamming,* Soft Matter **20**, 1996 (2024).

[37] Q. S. Li, G. Y. Lee, C. N. Ong, and C. T. Lim, *AFM indentation study of breast cancer cells,* Biochemical and Biophysical Research Communications **374**, 609 (2008).

[38] B. Zbiral, A. Weber, J. Iturri, M. M. Vivanco, and J. L. Toca-Herrera, *Estrogen modulates epithelial breast cancer cell mechanics and cell-to-cell contacts,* Materials **14** (2021), 10.3390/ma14112897.

[39] S. Moreno-Flores, R. Benitez, M. D. Vivanco, and J. L. Toca-Herrera, *Stress relaxation and creep on living cells with the atomic force microscope: A means to calculate elastic moduli and viscosities of cell components,* Nanotechnology **21** (2010), 10.1088/0957-4484/21/44/445101.

[40] G. Forgacs, R. A. Foty, Y. Shafrir, and M. S. Steinberg, *Viscoelastic properties of living embryonic tissues: A quantitative study,* Biophysical Journal **74**, 2227 (1998).

[41] K. Jakab, B. Damon, F. Marga, O. Doaga, V. Mironov, I. Kosztin, R. Markwald, and G. Forgacs, *Relating cell and tissue mechanics: Implications and applications,* Developmental Dynamics **237**, 2438 (2008).

[42] M. Layachi, L. Casas-Ferrer, G. Massiera, and L. Casanellas, *Rheology of vesicle prototissues: A microfluidic approach,* Frontiers in Physics **10** (2022), 10.3389/fphy.2022.1045502.

[43] N. Khalilgharibi, J. Fouchard, N. Asadipour, R. Barrientos, M. Duda, A. Bonfanti, A. Yonis, A. Harris, P. Mosaffa, Y. Fujita, A. Kabla, Y. Mao, B. Baum, J. J. Muñoz, M. Miodownik, and G. Charras, *Stress relaxation in epithelial monolayers is controlled by the actomyosin cortex,* Nature Physics **15**, 839 (2019).

[44] M. Dessard, J. B. Manneville, and J. F. Berret, *Cytoplasmic viscosity is a potential biomarker for metastatic breast cancer cells,* Nanoscale Advances **6**, 1727 (2024).

[45] M. Nikkhah, J. S. Strobl, R. De Vita, and M. Agah, *The cytoskeletal organization of breast carcinoma and fibroblast cells inside three dimensional (3-D) isotropic silicon microstructures,* Biomaterials **31**, 4552 (2010).

[46] C. Alibert, B. Goud, and J. B. Manneville, *Are cancer cells really softer than normal cells?* Biology of the Cell **109**, 167 (2017).

[47] K. Gnanachandran, S. Kędracka-Krok, J. Pabijan, and M. Lekka, *Discriminating bladder cancer cells through rheological mechanomarkers at cell and spheroid levels,* Journal of Biomechanics **144** (2022), 10.1016/j.jbiomech.2022.111346.

[48] R. C. Boot, A. van der Net, C. Gogou, P. Mehta, D. H. Meijer, G. H. Koenderink, and P. E. Boukany, *Cell spheroid viscoelasticity is deformation-dependent,* Scientific Reports **14** (2024), 10.1038/s41598-024-70759-y.

[49] F. Sauer, S. Grosser, M. Shahryari, A. Hayn, J. Guo, J. Braun, S. Briest, B. Wolf, B. Aktas, L. C. Horn, I. Sack, and J. A. Käs, *Changes in Tissue Fluidity Predict Tumor Aggressiveness In Vivo,* Advanced Science **10** (2023), 10.1002/advs.202303523.

[50] S. Grosser, J. Lippoldt, L. Oswald, M. Merkel, D. M. Sussman, F. Renner, P. Gottheil, E. W. Morawetz, T. Fuhs, X. Xie, S. Pawlizak, A. W. Fritsch, B. Wolf, L. C. Horn, S. Briest, B. Aktas, M. L. Manning, and J. A. Kas, *Cell and Nucleus Shape as an Indicator of Tissue Fluidity in Carcinoma,* Physical Review X **11** (2021), 10.1103/PhysRevX.11.011033.

[51] E. Warmt, S. Grosser, E. Blauth, X. Xie, H. Kubitschke, R. Stange, F. Sauer, J. Schnauß, J. M. Tomm, M. Von Bergen, and J. A. Kas, *Differences in cortical contractile properties between healthy epithelial and cancerous mesenchymal breast cells,* New Journal of Physics **23** (2021), 10.1088/1367-2630/ac254e.

[52] K. V. Iyer, R. Piscitello-Gómez, J. Paijmans, F. Jülicher, and S. Eaton, *Epithelial Viscoelasticity Is Regulated by Mechanosensitive E-cadherin Turnover,* Current Biology **29**, 578 (2019).

[53] M. Zanetti, L. Andolfi, M. R. Taylor, L. Mestroni, and M. Lazzarino, *AFM macroprobes to investigate whole 3D cardiac spheroids,* Micro and Nano Engineering **15** (2022), 10.1016/j.mne.2022.100134.

[54] Andrea Ivascu and Manfred Kubbies, *Diversity of cell-mediated adhesions in breast cancer spheroids,* International Journal of Oncology **31**, 1403 (2007).

[55] G. C. Russo, A. J. Crawford, D. Clark, J. Cui, R. Carney, M. N. Karl, B. Su, B. Starich, T. S. Lih, P. Kamat, Q. Zhang, P. R. Nair, P. H. Wu, M. H. Lee, H. S. Leong, H. Zhang, V. W. Rebecca, and D. Wirtz, *E-cadherin interacts with EGFR resulting in hyperactivation of ERK in multiple models of breast cancer,* Oncogene **43**, 1445 (2024).

[56] M. Pandey, Y. J. Suh, M. Kim, H. J. Davis, J. E. Segall, and M. Wu, *Mechanical compression regulates tumor spheroid invasion into a 3D collagen matrix,* Physical Biology **21** (2024), 10.1088/1478-3975/ad3ac5.

[57] H. P. Naber, E. Wiercinska, P. T. Dijke, and T. van Laar, *Spheroid assay to measure TGF-β-induced invasion,* Journal of Visualized Experiments (2011), 10.3791/3337.

[58] B. M. Leung, S. C. Lesher-Perez, T. Matsuoka, C. Moraes, and S. Takayama, *Media additives to promote spheroid circularity and compactness in hanging drop platform,* Biomaterials Science **3**, 336 (2015).

3

INVASIVE CANCER CELLS SOFTEN COLLAGEN NETWORKS AND DISRUPT STRESS STIFFENING VIA VOLUME EXCLUSION, CONTRACTILITY AND ADHESION

ABSTRACT

Collagen networks form the structural backbone of the extracellular matrix in both healthy and cancerous tissues, exhibiting nonlinear mechanical properties that crucially regulate tissue mechanics and cell behavior. Here, we investigate how the presence of invasive breast cancer cells (MDA-MB-231) influences the polymerization kinetics and mechanics of collagen networks using bulk shear rheology and rheo-confocal microscopy. We show that embedded cancer cells delay the onset of collagen polymerization due to volume exclusion effects. During polymerization, the cells (at 4% volume fraction) cause an unexpected time-dependent softening of the network. We show that this softening effect arises from active remodeling via adhesion and contractility rather than from proteolytic degradation. At higher cell volume fractions, the dominant effect of the cells shifts to volume exclusion, causing a two-fold reduction of network stiffness. Additionally, we demonstrate that cancer cells suppress the characteristic stress-stiffening response of collagen. This effect (partially) disappears when cell adhesion and contractility are inhibited, and it is absent when the cells are replaced by passive hydrogel particles. These findings provide new insights into how active inclusions modify the mechanics of fibrous networks, contributing to a better understanding of the role of cells in the mechanics of healthy and diseased tissues like invasive tumors.

This chapter is published as I.Nagle*, M. Tavasso*, A. D. Bordoloi, I.A. A. Muntz, G. H. Koenderink, P. E. Boukany, *Acta Biomaterialia (2025) (* equal author contribution)*

3.1. INTRODUCTION

Biological tissues exhibit tissue-specific mechanical properties, which arise from the complex interplay between extracellular matrix (ECM) composition, cell activity, and their relative proportions [1]. The ECM is a fibrous network composed of different biopolymers, including collagen, fibrin, and fibronectin. It serves as a scaffold for cell adhesion and controls the shape and mechanical properties of the tissue [2]. Additionally, it provides biochemical and biophysical cues to cells, which regulate essential processes such as cellular differentiation, tissue morphogenesis, wound healing, and homeostasis [3, 4]. Conversely, the ECM can also be altered by the activity of the cells themselves, including active force application [5] as well as chemical modifications, such as proteolytic degradation of the matrix [6]. Mechanochemical feedback mechanisms ensure tissue homeostasis and overall health [7] and disruptions in this feedback can contribute to pathological conditions such as fibrosis [8] or cancer [9]. These pathological states involve matrix remodeling and alterations of the tissue mechanics, at both local and global scales. In the context of cancer, for example, the tumor microenvironment undergoes extensive remodeling due to the activity of various cell types, including cancer-associated fibroblasts and malignant cancer cells. This remodeling generally results in increased tissue stiffness, primarily driven by ECM deposition, crosslinking, and contractile forces exerted by cells [9, 10].

A major challenge in deciphering the contributions of cells and ECM to the overall tissue mechanics arises from the intrinsic complexity of biological tissues, which feature heterogeneous compositions and architectures. One successful approach to address this limitation has been the development of biomimetic tissue models, where ECM components, such as collagen networks, are populated with cells, in order to replicate natural tissues [11, 12]. Collagen is the main determinant of the overall mechanical properties of connective tissues [13] and exhibits highly nonlinear responses to shear or tensile loading, with stiffness increasing sharply as strain increases [14]. Cells within the fibrous ECM network can act as volume-conserving inclusions, modifying its mechanical properties in a similar way to inert particles [15]. Recently, there have been several studies on the effect of inert microparticles that serve as passive inclusions on the mechanical properties of fibrous networks [15–17]. Stiff inclusions at high volume fractions can lead to compression-stiffening due to stretching of the interstitial ECM network. Nevertheless, cells are different from passive inclusions, as they actively interact with the surrounding network. Among cellular inclusions, fibroblasts have been extensively studied due to their ability to generate prestress and bundle ECM fibers. Their contractile forces stiffen the ECM by increasing fiber alignment and tension, reinforcing the overall stiffness of the network [18, 19]. For some other ECM components (like fibronectin and fibrin), tension can induce domain unfolding at submicron scales, undetectable by confocal microscopy [20–22]. However, this is not known to occur for fibrillar collagen. The mechanical influence of other cell types, such as invasive cancer cells, that interact dynamically with the matrix, remains less understood. Cancer cells, which remodel the ECM through matrix proteolysis and matrix deposition, adhesion, and dynamic forces [23, 24], may influence tissue mechanics in a distinct manner. To better understand the role of collagen in regulating the mechanics of cell-ECM composite systems, a two-phase model has been recently proposed, but only in the limit of high cell density cancer ag-

gregates [25]. Despite the critical function of cells in the tumor microenvironment, the precise role of cancer cells in modifying ECM mechanics, particularly in comparison to passive inclusions and fibroblasts, remains largely unexplored. Moreover, a clear disentangling between the contributions of passive mechanical effects versus active cellular processes to tissue mechanics is still lacking.

Here, we address this research gap by investigating how local cell-ECM interactions regulate the global mechanics of collagen networks in a biomimetic tissue model composed of fibrillar collagen type I with embedded cancer cells (volume fractions ranging from 0.4% to 20%). We initially test human dermal fibroblasts and compare their behavior to that of highly invasive MDA-MB-231 breast cancer cells, which are known to remodel and reorganize collagen type I fibers [26]. We explore by bulk shear rheology how the presence of the cells influences collagen polymerization and the mechanical properties of the final network. We show that the cancer cells delay the kinetics of collagen network assembly and cause softening of the collagen network. In addition, they suppress the stress-stiffening response of collagen networks above a threshold volume fraction. These findings are in marked contrast with the classical stiffening response seen with highly contractile fibroblasts. By comparing the impact of cells with that of passive cell-sized microparticles, we show that cells influence collagen polymerization and mechanics through a combination of volume exclusion and active remodeling dependent on integrin-mediated cell-matrix adhesion. Using a custom-built rheo-confocal microscope, we demonstrate that the cells dynamically remodel the collagen network in their local vicinity as it polymerizes. Our results show that cells influence collagen network mechanics through a delicate combination of volume exclusion, cell adhesion and contractility, providing new insights into the physical mechanisms that determine the mechanical properties of healthy and diseased tissues.

3.2. MATERIALS AND METHODS

3.2.1. CELL CULTURE

Human triple negative breast cancer cells (MDA-MB-231) stably transfected with either LifeAct-GFP (used in most experiments) or nls-mCherry (used only in collagen DQ assays to test collagen degradation) were cultured in DMEM high glucose medium (Gibco), supplemented with 10% fetal bovine serum (FBS, Gibco) and 1% antibiotic-antimycotic solution (15240062, Gibco). This serum-enriched medium is referred to as complete medium. Human dermal fibroblasts (HDF, NHDF-Ad, CC-2511, Lonza) were cultured in IMDM medium (31980022, Gibco) supplemented with 10% FBS (Gibco) and 1% Penicillin-Streptomycin (P/S, 15140122, Gibco). All cells were maintained in a 37°C incubator with 5% CO_2. MDA-MB-231 cells were subcultured at 90-100% confluency, and HDF cells were subcultured at 80% confluency. Cell counts and viability were assessed with the TC20^{TM} Automated Cell Counter (Bio-Rad) and Trypan Blue 0.4% (15250061, Gibco). MDA-MB-231 cells were cultured until passage 15 and human dermal fibroblasts were cultured until passage 11. The absence of mycoplasma was tested at least once every 4 months.

3.2.2. FABRICATION OF SOFT HYDROGEL MICROPARTICLES

Soft hydrogel microparticles with an average radius of 13 ± 6 μm were manufactured from acrylamide-co-acrylic-acid (PAA) by Rick Rodrigues (T. Schmidt lab, Leiden University) following a procedure described in [27]. The microparticles had an average Young's modulus of 4.9 ± 1.4 kPa as determined by shallow indentation measurements with an atomic force microscope [27]. They were stored at 4°C in PBS 1x with 1% (volume percentage) sodium azide at a particle volume fraction of ~ 15%.

3.2.3. PHARMACOLOGICAL INHIBITION OF CELL ADHESION, CONTRACTILITY AND METALLOPROTEINASES ACTIVITY

Non-muscle myosin II activity was inhibited by treating cells with (±)-blebbistatin (ab120425, Abcam), which inhibits the ATPase activity of myosin by blocking entry into the strong binding state [28]. The blebbistatin powder was dissolved in dimethylsulfoxide (DMSO) at a stock concentration of 5 mM. Cells adhering in plastic culture flasks were incubated with 10 μM blebbistatin [29] in complete medium (DMEM, 10% FBS and 1% antibiotic-antimycotic) in the incubator (37°C, 5 %CO_2) for 3 hours. Cells were then trypsinized (Trypsin-EDTA 0.25%, phenol red, Gibco), centrifuged for 4 minutes at 200 g and resuspended in the desired volume of complete medium, containing 10 μM blebbistatin, right before the rheology experiments.

Integrin β1-mediated cell adhesion to collagen was inhibited by treating cells with the anti-β1 integrin antibody (CD29, clone p5d2, MAB17781, R&D Systems). The antibody, supplied as a lyophilized powder, was dissolved in sterile PBS 1x at a stock concentration of 0.5 mg/mL. After cell detachment by trypsinization, cells were incubated in suspension with 10 μg/mL anti-β_1 integrin antibody for 15 minutes at 37°C. The cells were then centrifuged for 2 minutes at 200 g and the cell pellet was resuspended in the desired volume of complete medium, right before the rheology experiments.

Batimastat (BB-94), a broad spectrum MMP-inhibitor (ab146619, Abcam), was dissolved in DMSO to a stock concentration of 1 mM. Cells adhering in plastic culture flasks were incubated with 10 μM batimastat [30] in complete medium in the incubator for 3 hours. Cells were then trypsinized, centrifuged for 4 minutes at 200 g and resuspended in the desired volume of complete medium, to obtain a final concentration of 10 μM batimastat, right before the rheology experiments.

3.2.4. PREPARATION OF CELL- AND MICROPARTICLE-EMBEDDED COLLAGEN NETWORKS

Throughout this work, we used type I atelocollagen extracted from bovine hides, supplied as a 10 mg/mL solution in 0.01 N HCl (FibriCol®, 5133, Advanced Biomatrix) and stored at 4°C. The samples were prepared in Eppendorf tubes on ice just before experiments, to prevent premature collagen polymerization. First, the pH was adjusted to 7.4 (checked with pH paper strips, Whatman®, Cytiva) with 1% (volume percentage) 0.1 M NaOH (Sigma-Aldrich) and the salt concentration was adjusted with PBS 10x (524650-1EA, Merck-Millipore). Next, complete medium was added to reach a final collagen concentration of 4 mg/mL. If applicable, hydrogel microparticles or cells were included in the complete medium, in varying volume fractions. The cellular volumes were calculated from the average cell size measured by flow cytometry (see Figure S.3.1). The cel-

lular volume fractions were determined from the average cellular volume and the cell number density. Each hydrogel formulation was carefully adjusted to maintain constant collagen and salt concentrations in the fluid phase by taking into account the volume occupied by the cells or hydrogel microparticles.

3.2.5. BULK RHEOLOGY MEASUREMENTS

Rheology tests were performed with two stress-controlled rotational rheometers (Physica MCR 501, Anton Paar, Graz, Austria) equipped with a parallel plate geometry with a diameter of 20 mm and using a gap of 160 μm. For one rheometer we used the measuring plate PP20 (part no. 3049) and for the other one the shaft for disposable measuring systems (part no. 10636) with disposable plate D-PP20 (cat. no.17473, Anton Paar). Collagen solutions (with or without cells/hydrogel microparticles) were deposited on the bottom plate, preheated to 37°C. After quickly lowering the top plate to the desired gap, 500 μL of complete medium was pipetted around the sample edge to prevent drying. The time evolution of the storage and loss moduli (G' and G'', respectively) during collagen polymerization was monitored every 5 s by applying a small-amplitude (γ = 1%) oscillatory strain at a constant frequency f = 1 Hz for 90 minutes until the moduli reached their steady-state values. Next, the frequency-dependent shear moduli of the final network were measured by applying oscillations with a constant strain amplitude (γ = 1%) and a frequency ranging from 0.1 Hz to 10 Hz. Finally, the nonlinear elastic response and rupture stress of the network was tested by applying a stress ramp, with stresses logarithmically increasing from 0.01 Pa to 100 Pa at a rate of 10 points per decade and with 5 s between each point.

3.2.6. FLOW CYTOMETRY MEASUREMENTS OF CELL SIZES

The size distributions of MDA-MB-231 Lifeact-GFP and HDF cells were evaluated using a Cytek® Amnis® ImageStream®X Mk II Imaging Flow Cytometer. Cells were trypsinized (Trypsin-EDTA 0.25%, phenol red, Gibco), centrifuged at 200 g and then resuspended in PBS 1x at a concentration of a few tens of million of cells per mL. The cell diameter was measured using the bright-field channel. Cellular objects taken into account for the measurements had aspect ratios between 0.7 and 1 and areas between 300 and 1400 μm^2 or 150 and 600 μm^2 for HDF or MDA-MB-231 Lifeact-GFP cells, respectively. These thresholds were determined by visual inspection of the images to include only single cells. The average cell diameters over the entire population (6,223 cells for HDF and 13,234 cells for MDA-MB-231 Lifeact-GFP) were used to determine the collagen hydrogel formulation required to compensate for the volume occupied by the cells.

3.2.7. CONFOCAL IMAGING OF COLLAGEN NETWORKS AND COLLAGEN DEGRADATION

Confocal imaging was performed on collagen networks formed in 'static conditions', i.e., outside the rheometer parallel plates. To this end, the networks were polymerized in 18-well glass-bottom plates (81817, Ibidi) at 37°C (Thermomixer Comfort incubator, Eppendorf) in a humid atmosphere for 90 minutes. Complete cell medium was added on top of the gels after 45 minutes to avoid sample drying. The final network structure was visualized using a Zeiss LSM 710 confocal microscope (Carl Zeiss MicroImaging)

equipped with an AxioCam MRm camera and a 63x oil objective (Plan-APOCHROMAT 63/1.4 oil DIC ∞/0.17). The collagen network was imaged in reflection with a 514 nm laser. MDA-MB-231 cells expressed Lifeact-GFP and HDF cells were stained with SiR-Actin (Spirochrome) (incubation with 2 μM SiR-actin for 45 minutes at 37°C, 5 % CO_2). Actin was imaged by fluorescence microscopy with λ_{ex} = 488 nm and λ_{em} = 516 nm for Lifeact-GFP and λ_{ex} = 633 nm and λ_{em} = 646 nm for SiR-actin. Confocal Z-stacks were acquired over a total depth of 50 μm starting at a height of 10 μm above the coverslip with Z-steps of either 0.35 μm or 1 μm (xy-pixel size = 0.11 μm x 0.11 μm and pixel dwell time 0.78 μs).

Proteolytic degradation of the collagen gels by the cells was tested by confocal imaging of networks labelled with a fluorescent dye-quenched protein substrate (DQ-collagen I). Upon proteolytic cleavage, fluorescence is released and reflects the level of proteolysis by the cells [31]. Lyophilized DQ^{TM} collagen (type I from bovine skin, fluorescein conjugate, D12060, Thermofischer Scientific) was dissolved in sterile milliQ water at a stock concentration of 1 mg/mL. It was mixed at a concentration of 25 μg/mL with the 4 mg/mL collagen preparations. MDA-MB-231 stably transfected with nls-mCherry were embedded at a volume fraction of 4%. The cell-embedded network was polymerized in a humid atmosphere at 37°C using a Thermomixer Comfort incubator (Eppendorf) in 18-well glass-bottom plates (81817, Ibidi) for 90 minutes. Complete medium was added on top of the hydrogels after 45 minutes. The cell-embedded hydrogels were then incubated for 45 minutes at 37°C, 5% CO_2. Fluorescence resulting from collagen degradation was evaluated with the Zeiss LSM710 confocal microscope. The collagen network was imaged using reflection microscopy with a 514 nm laser and the degradation-induced fluorescence was imaged with a 488 nm laser (λ_{ex} = 488 nm and λ_{em} = 516 nm).

3.2.8. ANALYSIS OF COLLAGEN FIBER ORIENTATIONS

To quantify the relative orientation of collagen fibers with respect to the edges of individual hydrogel microparticles and MDA-MB-231 cells (hereafter referred to as “cells”), we employed a custom MATLAB 2021b algorithm taking input from automated analysis using the OrientationJ [32] plugin in Fiji (ImageJ v1.54f) [33]. First, multiple regions of interest (ROIs) were extracted from Z-stack reflection images (collagen channel) using ImageJ. We then considered the maximum intensity projection of Z-stacks (acquired with a step size of 0.35 μm or 1 μm) over a depth of 2 μm, focusing on the central imaging plane of individual cells or microparticles. Each ROI image projection was independently processed using the OrientationJ plugin in ImageJ to obtain the local pixel-based orientation ($\theta_{absolute}$) with respect to the x-axis. Subsequently, a binary mask of collagen fibers was created using intensity thresholding (using imbinarize in MATLAB), to eliminate noisy orientation values. Cell centroid positions and radii in the same ROI images were extracted using image thresholding: from the actin (Lifeact-GFP) channel (in the case of cells) or by fitting a circular shape to the boundary of the microparticle. Finally, the absolute fiber orientation angles were transformed into polar coordinates centered at each cell's/microparticle centroid, providing the relative orientation of fibers with respect to the edge of the cell/microparticle of reference. The analysis pipeline is shown in Figure S.3.2.

3.2.9. RHEO-CONFOCAL MICROSCOPY EXPERIMENTS

A dynamic shear rheometer measuring head (DSR 502, Anton Paar) was equipped with a custom-built bottom stage, designed to be mounted on the Zeiss LSM 710 confocal microscope, substituting the microscope XY-moving stage. A Peltier unit, connected to a control box (PE 94 Temperature Controller, Linkam), was mounted into the bottom stage using a 3D-printed holder to maintain a fixed temperature of 37°C. The Peltier module included a middle hole for optical access. Details are shown in Figure S.3.3. A glass coverslip of 30 mm diameter (No. 1, ECN 631-1585, VWR) was glued to the Peltier unit with a thin layer of silicon glue (5398, Loctite). The upper plate was the same geometry as the one used for the standard rheometers: parallel plate geometry with a diameter of 20 mm (shaft for disposable measuring systems (part no. 10636) with disposable plate D-PP20 (cat. no. 84855, Anton Paar).

In each experiment, first the zero gap was identified by lowering the upper plate and bringing it in contact with the glass bottom plate, with contact defined as the gap where the normal force was 0.1 N. The gap was then set to zero on a Mitutoyo dial indicator, which was subsequently used to measure the gap between the plates. After depositing the collagen solutions on the glass coverslip bottom plate, the upper plate was quickly and manually lowered until reaching the gap of 160 μm. To prevent sample drying and maintain humidity, 500 μL of complete medium was pipetted around the sample, and a metal hood with wet tissues was placed around the measuring head (Figure S.3.3).

Similar to the bulk rheology experiments, collagen network formation was monitored for 90 minutes by measuring the increase of the shear moduli using small amplitude oscillatory shear oscillations (γ = 1% and f = 1 Hz). At the same time, the collagen network (in reflection mode) and cells (in fluorescence mode) were imaged every 10 s or 20 s in a confocal plane fixed at a height of 30 μm above the coverslip (xy pixel size = 0.11 μm x 0.11 μm and pixel dwell time of 0.78 μs for each channel). The region of interest was located at a fixed radial distance of 0.7 R, with R being the radius of the top plate. After network formation, we applied a stress ramp with stresses logarithmically increasing from 0.01 Pa to 100 Pa at a rate of 10 points per decade and with 5 s between each point. We imaged the network every 2 s to 15 s (depending on the image size) at a height of 30 μm above the coverslip (xy-pixel size= 0.11 μm x 0.11 μm and pixel dwell time of 0.78 μs for each channel) until the rupture point, after which no reflection signal from the collagen was detected.

3.2.10. ANALYSIS OF RHEOLOGY DATA

The rheology data were analyzed using a custom-made script written in Python (version 3.11). All the derivatives were computed using the gradient function from the numpy Python library. The network polymerization onset time was defined from time sweeps (storage modulus $G'(t)$ versus time t) acquired during polymerization. It was defined as the intersection between the tangent to the curve's inflection point and the time axis, with the inflection point determined as the maximum of the derivative of the storage modulus with respect to time, $\frac{\partial G'}{\partial t}$ (see Supplementary Figure S.3.4a-b). Before computing the derivatives, the curves were smoothed using the function gaussian_filter1d from Python (sigma = 2 for standard rheology and sigma = 10 for rheo-confocal data to compensate for noisier data).

The differential modulus K was obtained from the stress-strain curves acquired in stress ramp experiments by calculating the local tangent according to $K = \frac{\partial \sigma}{\partial \gamma}$. The curves were smoothed using the function gaussian_filter1d from Python (sigma = 2). The strain and stress at rupture were identified as the point where K reached its maximum value (see Supplementary Figure S.3.4c-d). Plots of the differential modulus as a function of stress were truncated at this rupture point. Curves that showed clear evidence of wall slip, indicated by a non-monotonic trend before rupture, were excluded.

3.2.11. ANALYSIS OF CONFOCAL IMAGES

The kinetics of collagen network formation were determined from the rheo-confocal imaging data by determining the total intensity of reflection microscopy images over time using Fiji (ImageJ). Since cells are also visible in reflection images, we used the fluorescence signal from the GFP-LifeAct stained cells to exclude cell regions. The fluorescence images were processed by applying a Gaussian blur with 2 pixels radius (Fiji) followed by a conversion to a binary image using the Mean or Triangle method in Fiji. The resulting image was subsequently subtracted from the reflection images. Similar to the analysis of the polymerization onset time from the rheological measurements, we determined the onset time from the reflection intensity-time ($I(t)$) curves by finding the intersection between the tangent to the curve's inflection point (point where $\frac{\partial I(t)}{\partial t}$ is maximum) and the time axis.

3.2.12. STATISTICAL ANALYSIS

For each experiment, the figure captions specify the total number of samples (n) and the number of independent experiments (N). For boxplots, the center solid line represents the sample median, the box edges correspond to the first and third quartiles and the whiskers are equal to 1.5 times the inter-quartile range. All statistical tests were carried out with Mann-Whitney tests using the scipy Python library. Statistical significance is indicated using p-values (*, ** and *** corresponding to p<0.05, p<0.01 and p<0.001, respectively) and ns denotes non-significant differences.

3.3. RESULTS

3.3.1. CANCER CELLS AND FIBROBLASTS HAVE OPPOSITE EFFECTS ON COLLAGEN NETWORK MECHANICS

To investigate how different human cells influence the bulk mechanics of collagen networks, we first compared the effect of highly invasive cancer cells (MDA-MB-231) and human dermal fibroblasts (HDFs). Cells were mixed into 4 mg/mL collagen solutions at various volume fractions, ranging from 0.4% to 20%. This collagen concentration replicates the collagen density of breast tumor microenvironments [34]. To ensure a constant collagen network density, we compensated for the presence of the cells by adjusting the hydrogel formulation to account for the volume occupied by the cells calculated from their average diameter (29.3 ± 4.2 μm for HDF cells and 19.7 ± 2.1 μm for MDA-MB-231 cells, see Figure S.3.1). The cell-collagen mixture was polymerized between the two parallel plates of a shear rheometer with the plates spaced apart by 160 μm (see schematic in Figure 3.1a left). Collagen polymerization was monitored over a time period of 90 min-

utes by applying small-amplitude strain oscillations to measure the storage modulus G' and loss modulus G'' (Figure 3.1a middle). Next, the final network was subjected to a stress ramp to assess the nonlinear elastic response and rupture strength (Figure 3.1a right). The choice of gap size did not affect the mechanical properties of the networks (Figure S.3.5), indicating that no wall slip occurred during the measurements. Similarly, the application of a small oscillatory strain during polymerization had no effect on the network mechanics (Figure S.3.6).

Confocal fluorescence imaging of the actin cytoskeleton of the cells, once collagen polymerization was complete, showed that the fibroblasts were elongated with branched protrusions extending from the cell poles (green signal in Figure 3.1b), whereas the cancer cells were roundish and showed only small protrusions (Figure 3.1c). This difference in cell morphologies suggests that fibroblasts interact more persistently with the collagen matrix and may exert greater long-term contractile forces on the network compared to cancer cells. This was further confirmed by reflectance imaging of the collagen network surrounding the cells, that showed accumulation of collagen fibers (grey signal in Figure 3.1b) near the fibroblasts protrusions, but a more homogeneous collagen fiber distribution around the cancer cells (Figure 3.1c).

Time-resolved rheology experiments showed that these morphological differences were associated with opposite effects of the cells on the bulk mechanics of the collagen network: the fibroblasts caused global stiffening of the collagen matrix, whereas the cancer cells caused a global softening, relative to control networks (Figure 3.1d). For control networks (in absence of cells), the storage modulus G' suddenly started to increase after a delay time of a few hundred seconds, and then quickly reached a constant value. This kinetic behavior reflects the known nucleation-and-growth mechanism of collagen polymerization [35, 36]. In the presence of fibroblasts, the storage modulus showed a biphasic increase with time. The first stiffening phase set in at a time point that was only weakly dependent on cell density, suggesting that it originates from collagen fiber nucleation (Figure S.3.7). The second phase set in at a time point that did depend on cell volume fraction (compare 0.4% and 4%, individual curves in Figure S.3.8), suggesting that it is due to cell-mediated contraction. The loss modulus G'' showed similar time dependencies as the storage modulus (Figure S.3.9). In marked contrast to the fibroblasts, the invasive cancer cells (MDA-MB-231) caused global softening of the collagen network relative to control networks (Figure 3.1e). This effect was dependent on cell density. Cells at 0.4% did not significantly impact the final storage modulus. Strikingly, however, cells at 4% caused a non-monotonic time-dependent modulus. The elastic modulus first increased, peaking at a value similar to the control network, and then gradually decreased to a final value about two-fold lower than for the control networks. This non-monotonic behavior was observed for more than 75% of the samples (Figure S.3.10). When the cell volume fraction was further raised to 20%, the non-monotonic behavior was lost, but the final network was again about two-fold softer than the control network. We did not observe any obvious changes in the collagen fiber length or density in the network surrounding the cells to explain the softening (Figure S.3.11). We note that the loss modulus G'' showed similar time dependencies as the storage modulus (Figure S.3.12). Overall, the only similarity between the behavior of the fibroblasts and MDA-MB-231 cells was that they both delayed the onset of collagen polymerization (Figure 3.1i).

Following collagen polymerization, the nonlinear elastic behavior of the mature network was assessed by applying a gradually increasing shear stress until network rupture. We quantified the nonlinear response via the differential modulus K, defined as the local derivative of the stress/strain curves ($K = \frac{\partial \sigma}{\partial \gamma}$). With increasing stress, control networks showed an initial linear response (constant K values), followed by stress-stiffening above stresses of $\sim$ 1 Pa (grey curves in Figure 3.1f and g). Stress-stiffening behavior is a well-known feature of collagen networks that is attributed to a transition from a soft-bending-dominated regime at small deformations to a rigid stretch-dominated regime at large deformations [14, 37, 38]. Fibroblasts and cancer cells had very different effects on this stress-stiffening behavior. Fibroblasts only minimally affected the stress-stiffening behavior of collagen, irrespective of cell volume fraction (Figure 3.1f, individual curves in Figure S.3.13a-c). Furthermore these cells did not affect the rupture strain nor the rupture stress (Figure S.3.13d-e). By contrast, the cancer cells strongly inhibited the stress-stiffening behavior of collagen above a cell volume fraction of 4% (Figure 3.1g). They also strongly reduced the rupture strain γ_r (Figure 3.1h) and rupture stress σ_r (Figure S.3.14) compared to the control collagen network. We conclude that fibroblasts and cancer cells have opposite effects on the bulk rheology of collagen. Fibroblasts apply contractile stress and cause network stiffening, whereas the cancer cells apply minimal contractile stress, cause network softening, and suppress stress-stiffening.

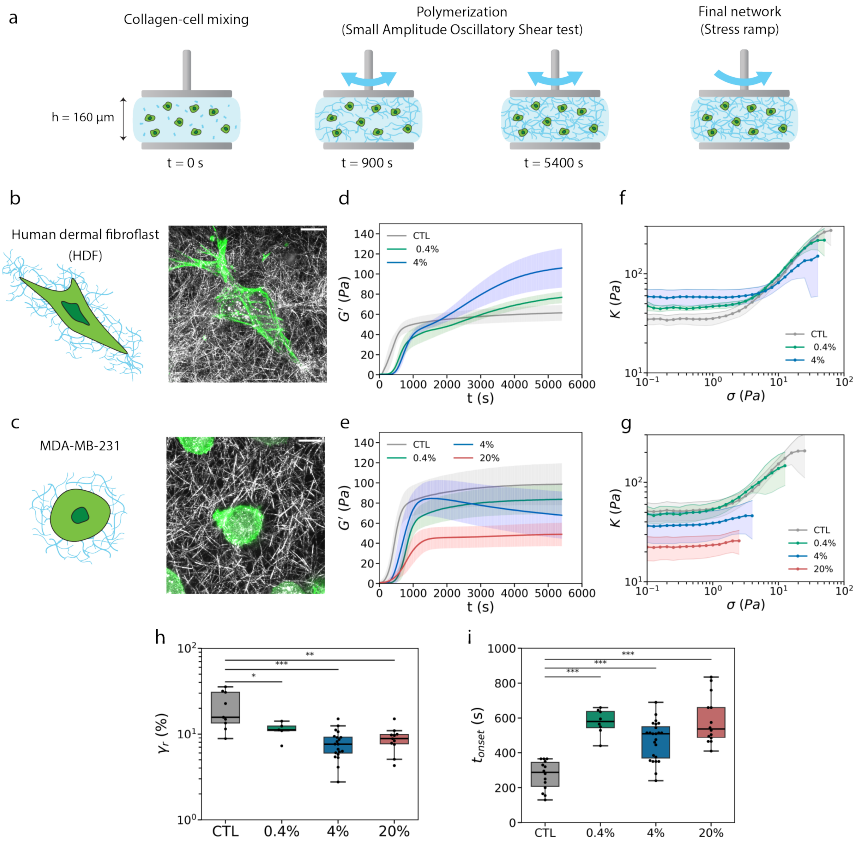

Figure 3.1: **Invasive breast cancer cells (MDA-MB-231) and human dermal fibroblasts (HDF) have opposite effects on the bulk rheology of collagen networks.** (a) Cells were mixed with a solution of type I collagen monomers and confined between the two parallel plates of a shear rheometer at t=0 (left). Collagen polymerization was monitored by applying small-amplitude shear oscillations (middle). The final network was subjected to a stress ramp to assess the nonlinear elastic response and rupture strength (right). (b-c) Fibroblasts (b) and breast cancer cells (c) embedded in a collagen network. Schematics (left) and maximum intensity projections of confocal Z-stacks (right). Collagen fibers (grey) were imaged using reflection and the cellular actin cytoskeleton (green) was imaged via fluorescence (using SiR-actin labelling for HDF cells and Lifeact-GFP for MDA-MB-231 cells). Scale bars are 10 μm. (d-e) Storage modulus G' as a function of polymerization time for various volume fractions of HDF cells (d, CTL: n=4, N=1; 0.4%: n=2, N=1; 4%: n=4, N=1) and MDA-MB-231 cells (e, CTL: n=16, N=8; 0.4%: n=8, N=3; 4%: n=24, N=10; 20%: n=16, N=8). Data represent mean ± SD. (f-g) Differential modulus K as a function of applied shear stress for cell-embedded collagen networks with various volume fractions of HDF (f, CTL: n=3, N=1; 0.4%: n=2, N=1; 4%: n=4, N=1) and MDA-MB-231 cells (g, CTL: n=9, N=4; 0.4%: n=5, N=2; 4%: n=20, N=8; 20%: n=11, N=6). Data represent mean ± SD. (h-i) Boxplots of the strain at rupture γ_r (h) and the collagen polymerization onset time t_{onset} (i) measured for control networks (CTL) and networks containing MDA-MB-231 cells at volume fractions of 0.4%, 4% or 20%.

3.3.2. BOTH VOLUME EXCLUSION AND CELL ADHESION IMPACT COLLAGEN NETWORK MECHANICS

The embedded cancer cells could modulate collagen network mechanics by acting as viscoelastic inclusions [15] and/or by actively exerting forces on the collagen fibers through

integrin-mediated adhesion receptors [39]. To test the importance of volume exclusion, we first performed bulk rheological measurements on collagen networks with embedded soft hydrogel microparticles. These microparticles are inert, cell-sized, mechanically uniform and isotropic [27]. Importantly, they lack collagen-binding sites on their surface, so they merely serve as soft passive cell-sized inclusions [40, 41]. Confocal imaging showed that collagen fibers in close proximity of the microparticles (MPs) were oriented tangentially to their surface (Figure 3.2a and Figure S.3.15a-b), in contrast to the isotropic orientation of collagen fibers around the cancer cells (Figure 3.1c, Figure S.3.15a-b). Nevertheless, the passive microparticles caused a similar reduction in the elastic modulus of the collagen networks (Figure 3.2b) as the cancer cells. The microparticles also similarly delayed collagen polymerization (Figure 3.2h), indicating that passive inclusions slow down the collagen polymerization process. At 20% volume fraction, the inclusion of microparticles resulted in a two-fold reduction in the network stiffness, comparable to the decrease observed with cancer cells. This result suggests that the softening observed at higher cell volume fractions is driven by a volume exclusion effect rather than cell-matrix adhesion.

At the lower volume fraction of 4%, however, we observed an interesting difference in the time dependence of the modulus for microparticles versus cells: the time dependence was monotonic for microparticles (Figure 3.2b), whereas it was non-monotonic for cancer cells (Figure 3.1e). Stress ramp experiments revealed another notable difference: while the cancer cells suppress stress-stiffening, the hydrogel microparticles preserved the stress-stiffening behavior of collagen networks across all volume fractions (4% and 20%) (Figure 3.2c). Stress-stiffening curves for networks with microparticles normalized to the linear modulus of the corresponding control network ($K_0(CTL)$) overlapped with the control collagen at stresses above ~ 2 Pa. The microparticles also did not significantly change the network rupture strain (Figure 3.2g) nor rupture stress (Figure S.3.16), in contrast to the reduced strength in presence of the cancer cells.

These observations suggest that volume exclusion only partially explains the impact of cancer cells on collagen network mechanics. To test whether integrin-mediated adhesion also plays a role, we embedded cancer cells in collagen while blocking β1-integrin adhesion receptors with a specific antibody. β1-integrins are known to mediate cell adhesion to collagen type I fibers [42]. Confocal imaging showed that collagen fibers in close proximity of cancer cells with blocked integrins were more tangentially oriented as compared to fibers around untreated cells (Figure 3.2d and Figure S.3.15a-b), although this effect was less pronounced than the tangential orientation observed around the hydrogel microparticles. Further away from the adhesion-inhibited cells and the microparticles (beyond 4 μm), the collagen fibers were instead arranged isotropically (Figure S.3.15c). Similar to the microparticles, the adhesion-inhibited cells delayed the onset of collagen polymerization (Figure 3.2h) and reduced the final network modulus (Figure 3.2e, for individual curves see Figure S.3.17). At a volume fraction of 20%, the adhesion-inhibited cells reduced the modulus by about two-fold compared to control networks, comparable to the impact of the non-adhesive microparticles. At a volume fraction of 4%, collagen with adhesion-inhibited cells showed a monotonic increase of the modulus with time, similar to collagen with microparticles. Finally, collagen networks with adhesion-inhibited cells showed stress-stiffening across all cell volume frac-

tions (Figure 3.2f), although less marked than with microparticles. There were striking differences between collagen gels with adhesion-inhibited cells compared to cells capable of integrin-mediated adhesion. Networks with cells capable of adhesion showed a non-monotonic dependence of the storage modulus with time during collagen polymerization, not seen upon integrin blocking. Also, networks with adherent cells did not stress-stiffen and had smaller rupture strains (Figure 3.1h) and stresses (Figure S.3.16) than networks with adhesion-inhibited cells (Figure 3.2g). These observations suggest that the cancer cells affect collagen mechanics by a combination of volume exclusion and adhesion-dependent effects. Non-adherent particles and cells (irrespective of adhesion) cause a delay in collagen polymerization and lowering of the final network modulus at high enough volume fraction of the inclusions. These are apparently effects caused by volume exclusion. However, the time-dependent decrease in the storage modulus at low cell volume fraction (4%) and the loss of collagen stress-stiffening are directly associated with the cells' ability to adhere to collagen fibers.

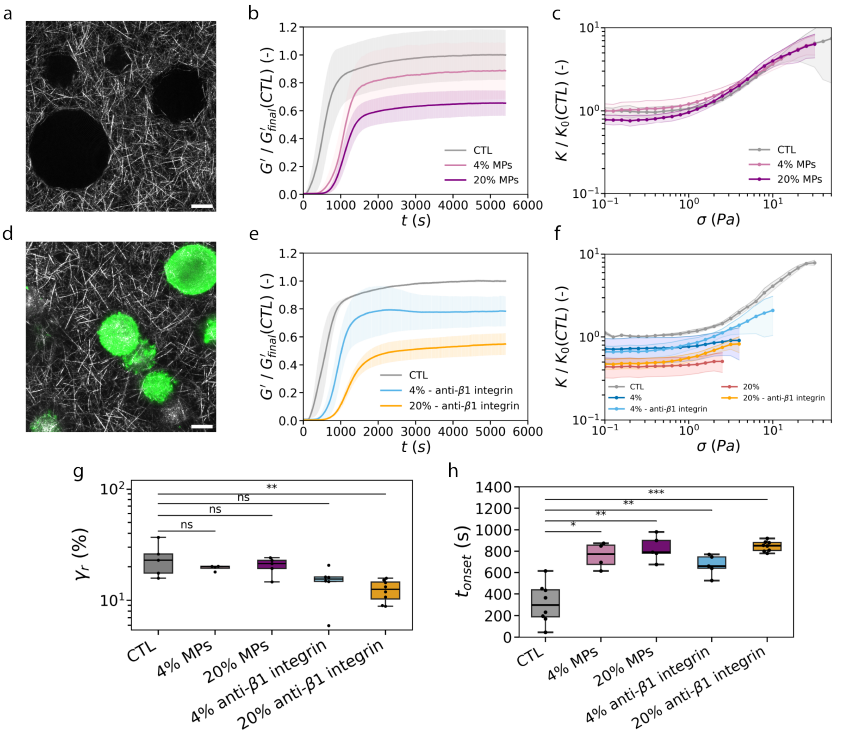

Figure 3.2: **Volume exclusion and cell adhesion together determine the impact of cancer cells on the bulk mechanics of collagen networks.** (a,d) Maximum intensity projections of Z-stacks of confocal images across a depth of 10 μm of a collagen network with embedded soft hydrogel microparticles (a) or MDA-MB-231 cancer cells with an adhesion-blocking anti-β1 integrin antibody (d). Scale bars are 10 μm. Collagen (grey) is imaged in reflection and the cells (green) in fluorescence (using LifeAct-GFP labeling). The dark circles in (a) are due to the presence of microparticles. (b,e) Storage modulus G' normalized to the final modulus of control collagen ($G'_{final}(CTL)$) as a function of polymerization time for networks with hydrogel microparticles (MPs) (b, CTL: n=6, N=2; 4%: n=4, N=2; 20%: n=5, N=2) or adhesion-blocked MDA-MB-231 cells (e, CTL: n=2, N=1; 4%: n=5, N=2; 20%: n=8, N=2), at volume fractions of 0% (CTL), 4% and 20%. Data represent mean ± SD. (c,f) Differential modulus K normalized to the linear modulus of control collagen ($K_0(CTL)$) as a function of applied shear stress σ for networks containing hydrogel microparticles (c, CTL: n=3, N=2; 4%: n=4, N=2; 20%: n=5, N=2) or adhesion-blocked MDA-MB-231 cells (f, CTL: n=2, N=1; 4%: n=5, N=2; 20%: n=8, N=2) at volume fractions of 0% (CTL), 4% and 20%. (g-h) Boxplots of the strain at rupture γ_r (g) and of the collagen polymerization onset time t_{onset} (h) for collagen networks containing hydrogel microparticles or adhesion-inhibited MDA-MB-231 cells at volume fractions of 0% (CTL), 4% and 20%.

3.3.3. RHEO-CONFOCAL IMAGING REVEALS DYNAMIC CELL-MEDIATED NETWORK REMODELING

To understand why cancer cell adhesion impacts the bulk mechanics of the collagen networks, we integrated a rotational rheometer with an inverted confocal microscope, enabling simultaneous rheological measurements and confocal imaging of the collagen network and embedded cells (Figure 3.3a). Briefly, a shear rheometer measuring head was placed on top of a confocal microscope, substituting its XY-moving stage (Figure S.3.3). A glass coverslip was used as bottom plate, to allow high resolution confocal

imaging of the samples from below (with minimal effect on the apparent rheological measurements as shown in Figure S.3.18).

We first used the rheo-confocal setup to correlate the time evolution of the shear moduli during collagen polymerization with the underlying changes in network structure. Confocal imaging showed that collagen fibers first appeared around the same time that the storage modulus started to suddenly increase (Figure S.3.19a). This was observed both in the absence (Supplementary Video 1) and presence (Supplementary Video 2) of cancer cells. The onset times determined from the time-dependent increase of the normalized intensity of the collagen networks (reflection channel) were longer than those obtained from the storage modulus (Figure S.3.19b-d). This discrepancy may result from the inability to detect fibers below a certain thickness by reflection microscopy [43] and the limitation of imaging to a specific region of the sample. Importantly, both confocal imaging and rheology showed that cancer cells increased the onset times for collagen polymerization by about 50% as compared to control collagen networks, confirming that the presence of cells delays nucleation and growth of collagen fibers. Confocal fluorescence imaging showed that the cancer cells actively remodeled the collagen network in a dynamic way as the network formed (Supplementary Videos 3-5). The cancer cells extended and retracted actin-containing membrane protrusions, which mechanically engaged with collagen fibers. The high F-actin intensity in cell protrusions coincided with regions where the collagen networks was visibly remodeled (Figure 3.3b and Supplementary Videos 3-5), indicating that the cells remodel the network through active force application. We observed clear examples of collagen fiber bending (see example denoted by the arrow at the top of the time lapse image series in Figure 3.3b) and pulling (see example denoted by the arrow in the center of the time lapse image series in Figure 3.3b). These fiber deformations were transient, relaxing after the cells retracted the protrusions. Thus, cancer cells can transiently (on timescales of tens of minutes) alter the local structure of the surrounding collagen network through active mechanical interactions with collagen fibers. Similar imaging of the mature collagen network, with or without embedded cancer cells, was performed during the shear stress ramp (Supplementary Videos 6-7). Upon shear, fibers and cells exhibited co-translation up to the rupture point, indicated by the loss of reflection signal. We could not observe any notable differences in collagen fiber displacement under shear between control networks versus networks with cells to explain the loss of stress-stiffening or the reduced rupture strength. In contrast to actively remodeling cancer cells, we also examined the effect of passive, non-adhesive microparticles (at 20% volume fraction) embedded in the collagen network in the rheo-confocal setup (Supplementary Videos 8–9). During polymerization under oscillatory shear (Supplementary Video 8), collagen fibers appeared in random locations with no evidence of preferential nucleation around MPs, which were visualized as voids in the reflection signal. Under a shear stress ramp (Supplementary Video 9), the MPs and surrounding fibers exhibited global lateral co-translation up to the rupture point, where MPs remained undeformed up to about 10 Pa. This comparison highlights that while cancer cells actively remodel and mechanically engage with the collagen network, passive microparticles primarily influence network behavior in a volume-exclusion manner.

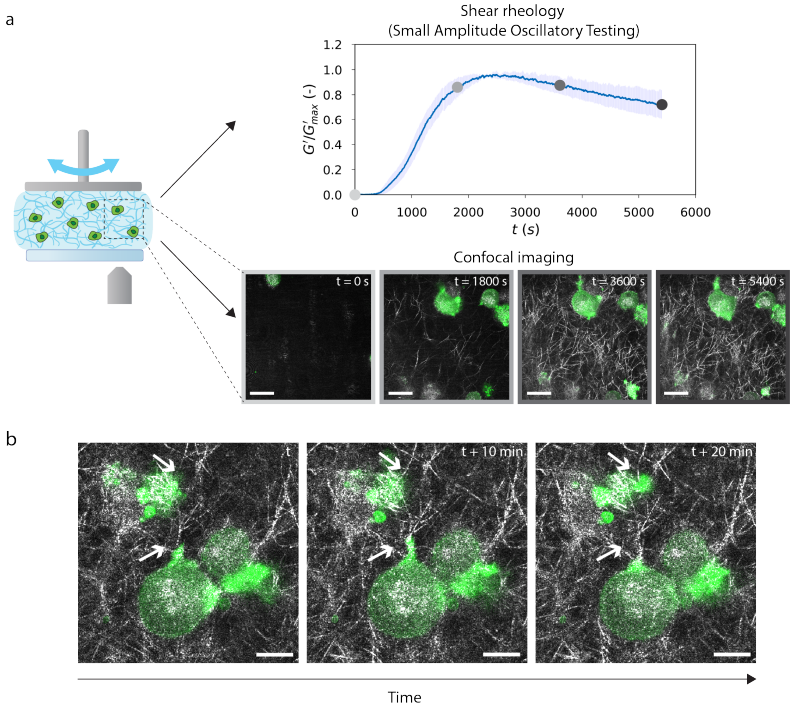

Figure 3.3: **Rheo-confocal microscopy demonstrates dynamic local remodelling of the collagen network by the cancer cells via actin-mediated protrusions.** (a) Schematic of the rheo-confocal setup allowing simultaneous shear rheology measurements and confocal imaging. Top row: Storage modulus G' normalized by its maximum G'_{max} value as a function of polymerization time for a collagen network containing 4% MDA-MB-231 cells. Data represent mean ± SD ($N = 3$). Bottom row: Corresponding representative confocal images at different time points (indicated by colored circles in the shear rheology curve). Collagen fibers are visible in grey (reflection microscopy) and actin labeled with LifeAct-GFP (fluorescence microscopy) is shown in green. Scale bars are 20 μm. (b) Representative time-lapse confocal images for a collagen network (grey) containing 4% MDA-MB-231 cells (green) at different times after the initiation of polymerization. We observe cell-mediated collagen fiber bending (white arrow at the top of the images) and fiber pulling (white arrow at the center of the images). These local remodeling events occur for collagen fibers associated with small cell protrusions. Scale bars are 10 μm.

3.3.4. ACTIVE CELL CONTRACTILITY CONTRIBUTES TO COLLAGEN NETWORK SOFTENING

The rheo-confocal experiments revealed that cancer cells actively interact with collagen fibers through actin-filled protrusions and bend, pull and displace collagen fibers. Combined with the observation that blocking integrin-mediated cell adhesion prevented time-dependent softening of cell-embedded gels and restored stress-stiffening, we hypothesized that active myosin-driven contraction may contribute to the mechanics of cell-embedded networks. To test this hypothesis, we inhibited cell contractility with (±)-blebbistatin, a specific myosin II ATPase inhibitor. Since blebbistatin is dissolved in dimethyl sulfoxide (DMSO), we first verified that exposure to DMSO (0.2% volume fraction) did not affect the cells nor their interaction with the collagen network (Figure S.3.20).

Interestingly, the effect of blebbistatin on the rheology of cell-embedded collagen networks depended on cell density. At high cell volume fraction, the polymerization behavior and the final storage modulus and stress-stiffening behavior of the networks (Figure 3.4a-b) were similar as in absence of blebbistatin. By contrast, blebbistatin significantly changed these features for collagen networks containing cells at an intermediate (4%) volume fraction. First, blebbistatin addition prevented the non-monotonic time-dependence of the storage modulus with a peak at intermediate times seen in its absence (Figure 3.4c, individual curves in Figure S.3.21). Thus, in presence of blebbistatin, the polymerization curves were comparable to those of control collagen and collagen with adhesion-blocked cells. This finding indicates that both cell adhesion and myosin-based contractility are needed for time-dependent network softening by cancer cells. An alternative explanation for cell-mediated network softening could be proteolytic degradation by cell-secreted or cell-surface enzymes. We could, however, exclude this explanation, as no collagen degradation was observed on our experimental time scale (Figure S.3.22). Second, blebbistatin addition recovered stress-stiffening of cell-embedded networks (Figure 3.4d), which was impaired in absence of blebbistatin. Also, blebbistatin returned the rupture strain (Figure 3.4e) and stress (Figure S.3.24) to values close to those of control collagen networks. Apparently, the cancer cells suppress stress-stiffening of collagen networks by physical remodeling, which requires integrin-based adhesion to collagen and myosin-driven active forces.

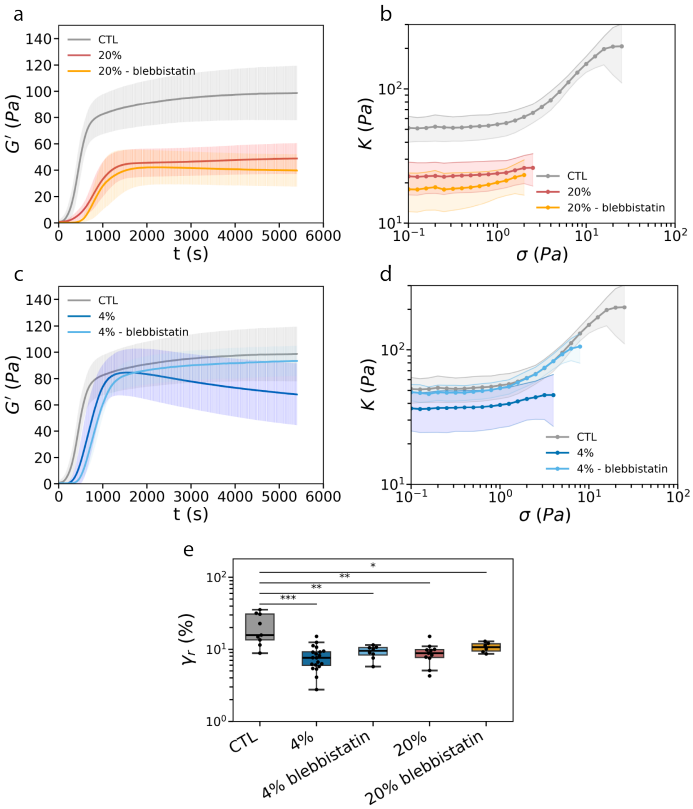

Figure 3.4: **Inhibiting myosin-based contractility of cancer cells demonstrates that cells influence collagen mechanics through active remodeling only at intermediate cell volume fractions.** (a,c) Storage modulus G' as a function of polymerization time for collagen networks containing MDA-MB-231 cells at a volume fraction of 20% (a, CTL: n=16, N=8; 20%: n=16, N=8; 20%- blebbistatin: n=6, N=2) or 4% (c, CTL: n=16, N=8; 4%: n=24, N=10; 4%- blebbistatin: n=8, N=2), comparing control conditions (no cells) and cell-embedded networks with or without blebbistatin treatment (3 hours at 10 μM). (b,d) Differential modulus K as a function of applied shear stress σ for collagen networks containing MDA-MB-231 cells at a volume fraction of 20% (b, CTL: n=9, N=4; 20%: n=11, N=6; 20%- blebbistatin: n=6, N=2) or 4% (d, CTL: n=9, N=4; 4%: n=20, N=8; 4%- blebbistatin: n=8, N=2), comparing control conditions (no cells) and cell-embedded networks with or without blebbistatin. Data represent mean ± SD. (e) Boxplots of the strain at rupture (γ_r) for collagen networks with 0%, 4% or 20% cells, with or without blebbistatin treatment.

3.4. DISCUSSION

Cells play a critical role in shaping the mechanical properties of their surrounding matrix [4, 44]. They can influence the matrix through multiple interconnected processes, including volume exclusion effects [15, 16, 45, 46], adhesion [47], mechanical force generation [26], and biochemical modifications [48]. Since these mechanisms often act simultaneously, decoupling each of their effects on the matrix mechanics is challenging. Here, we investigated how cancer cells influence the shear mechanics of collagen type I networks in bulk rheology experiments. To disentangle the contribution of each individual process, we used cell-sized microparticles to test the impact of passive inclusions,

myosin and integrin inhibitors to test the influence of cell adhesion and contractility.

Different cell types (cancer cells and fibroblasts), but also passive hydrogel microparticles, delayed the onset of collagen polymerization even at small volume fractions. Rheo-confocal experiments showed via simultaneous imaging and rheology that collagen networks are formed through the nucleation of collagen fibers, which rapidly grow and thicken as the network matures. Both cells and microparticles delayed the first appearance of fibers. Apparently, the space occupied by the inclusions reduces the available space for collagen polymerization and thereby delays the formation of a network-spanning structure, consistent with the theory of gelation through percolation [49]. Interestingly, the effect of cell-sized inclusions is opposite to that of small (100 nm) extracellular vesicles, which were recently shown to accelerate collagen fibrillogenesis [50]. While extracellular vesicles likely act as nucleation points, much larger (tens of micrometers) cells and microparticles delay network formation through a passive volume exclusion effect.

The final stiffness of the collagen networks was strongly dependent on the type of inclusion. Human dermal fibroblasts stiffened the collagen networks even at the lowest volume fraction tested (0.4%) (Figure 3.1d). By contrast, cancer cells softened the collagen networks at volume fractions between 4% and 20%. Both cell types adhere to and actively interact with the collagen fibers, but their distinct effects on stiffness arise from differences in the nature and timescale of these interactions: fibroblasts apply sustained traction that promotes strain-stiffening [51], whereas cancer cells engage in dynamic, transient remodeling that disrupts sustained fiber loading and softens the network. Fibroblasts continuously pull on the collagen network with their filopodia [52]. As a consequence, they generate a significant contractile prestress that stiffens the entire network because of its inherent nonlinear response. A similar fibroblast-induced stiffening effect was previously demonstrated for fibrin networks that exhibit similar stress-stiffening behavior as collagen [53]. Several studies also evidenced a local stiffening of collagen networks around embedded fibroblasts [26, 54–56], which was attributed to the alignment and recruitment of collagen fibers through pulling forces. Confocal imaging showed that the MDA-MB-231 cancer cells, as compared to fibroblasts, interact in a much more dynamic and transient manner with collagen. The cells extend small protrusions that can bend, pull and displace collagen fibers. However, the protrusions are transient (minute lifetimes) and the fibers are released upon retraction of the protrusions. As a result, there is much less accumulation of collagen fibers around the cancer cells as compared to the fibroblasts (Figure 3.1b,c). Previous studies measuring local changes in matrix stiffness near cancer cells reported either a local matrix stiffening [26, 56, 57] or no significant mechanical changes [54]. In contrast, our bulk rheology experiments reveal network softening at a macroscopic scale. This discrepancy between local and global mechanical properties is likely a reflection of the highly heterogeneous structure of collagen networks. Computational models have shown that, due to their low connectivity (with mostly three-fold junctions), collagen networks exhibit a highly heterogeneous (non-affine) response to mechanical loading [58, 59].

So, how can the transient and local interactions of cancer cells with the collagen network cause global network softening? At low (4%) cell volume fraction, the cells caused an intriguing time-dependent softening during collagen polymerization. Importantly, this softening was not caused by any proteolytic degradation of the collagen (Figure

S.3.22) and the inhibition of metalloproteinase (MMP) activity with batimastat had no significant effect on the rheological behavior within the timescale of our experiments (Figure S.3.23). Instead, cell-mediated softening was dependent on myosin-driven contractility and integrin-mediated adhesion, as shown by experiments where we blocked myosin II activity or β1-integrins. Interestingly, a similar inclusion-mediated network softening was recently observed with thermosensitive hydrogel beads that were made to contract by heating [60]. In this study, softening was hypothesized to arise from collagen fiber buckling. Similarly, the cancer cells might buckle collagen fibers in their vicinity.

At higher cell volume fractions (20%), time-dependent softening of the collagen networks was much less striking than at low volume fraction (Figure S.3.10), but the final network was still softer than the cell-free networks. This observation suggests that the global shear mechanics of cell-embedded networks depends on a combination of local active cell-mediated network remodeling and volume exclusion. We surmise that the volume exclusion effect is dominant at higher (20%) volume fractions, where cancer cells and passive microparticles confer a comparable softening effect. It will be interesting to investigate under which physiological circumstances cells can act as such inclusion bodies. For instance, quiescent stromal cells might act similarly to passive inclusions, modulating mechanics mainly through their physical presence [61]. At small (4%) volume fractions, where the space occupied by the cells is smaller, the influence of volume exclusion is smaller, so the time-dependent softening by active collagen remodeling is more dominant. Cell-mediated softening of mature collagen networks has also previously been reported in the presence of Chinese ovary hamster (CHO) cells [62]. This study attributed the softening to the cells' ability to recruit collagen around themselves, thereby depleting collagen from the remaining network. For the cancer cells studied here, we can exclude this explanation since confocal imaging revealed a uniform collagen density.

Finally, we found that cells also altered the bulk nonlinear elastic response of collagen network mechanics. Fibroblasts and cancer cells again had opposite effects. While fibroblasts merely slightly decreased the strain and stress at rupture, the cancer cells suppressed collagen stress-stiffening and markedly reduced the strain and stress at rupture. Impairment of stress-stiffening required cell-matrix adhesion: when we blocked β1-integrin-mediated adhesion, stress-stiffening was (partially) restored. Similarly, passive microparticles that did not adhere to collagen did not affect the stress-stiffening behavior. We speculate that anchoring of the fibers to the cells and the altered collagen organization in the immediate proximity of the cells, acting as defects, hinder long-range stress transmission in the network, leading to loss of stress-stiffening.

3.5. CONCLUSIONS

In this study, we showed that invasive cancer cells soften collagen networks and suppress stress-stiffening. This effect is opposite to the more well-studied effect of fibroblasts, which stiffen collagen networks. We showed that softening is caused by a combination of a passive mechanism (volume exclusion) and active mechanisms (network remodeling mediated by cell contractility and adhesion). The balance between these two contributions depends on the cell volume fraction, with the volume exclusion effect predominating at higher cell densities. By using a biomimetic tissue model system, we

were able to shed new light on the mechanical role of living cells in fibrous networks, demonstrating how their nonequilibrium activity can influence the global mechanical response under shear. Our work provides a fundamental basis to understand the biophysical processes by which different types of cells impact tissue mechanics in health and disease.

3.6. CREDIT AUTHORSHIP CONTRIBUTION STATEMENT

Irène Nagle: Writing – original draft, Visualization, Validation, Software, Methodology, Investigation, Formal analysis, Data curation, Conceptualization. **Margherita Tavasso:** Writing – original draft, Visualization, Validation, Software, Methodology, Investigation, Formal analysis, Data curation, Conceptualization. **Ankur D. Bordoloi:** Software, Formal Analysis, Data curation, Writing - review. **Iain A.A. Muntz:** Software, Methodology, Conceptualization, Writing - review. **Gijsje H. Koenderink:** Writing – review & editing, Validation, Supervision, Project administration, Funding acquisition, Conceptualization. **Pouyan E. Boukany:** Writing – review & editing, Validation, Supervision, Project administration, Funding acquisition, Conceptualization.

3.7. DECLARATION OF COMPETING INTEREST

The authors declare that they have no known competing financial interests or personal relationships that could have appeared to influence the work reported in this paper.

3.8. DATA AND CODE AVAILABILITY

All data reported in this paper are available upon request. The original codes have been deposited on GitHub and can be accessed publicly via these links: https://github.com/irenenagle/functions_rheology and https://github.com/aerials00/fiber_analysis

3.9. ACKNOWLEDGEMENTS

I. Nagle and G. H. Koenderink gratefully acknowledge the Flagship Healthy Joints, which is (partly) financed by Convergence Health and Technology, for funding. M. Tavasso and P.E. Boukany gratefully acknowledge funding from the European Research Council (ERC) under the European Union's Horizon 2020 research and innovation program (grant agreement no. 819424). A.D. Bordoloi gratefully acknowledges funding from MSCA Postdoctoral Fellowships 2022 Project ID: 101111247. MDA-MB-231 Lifeact-GFP and nls-mCherry cells were kindly provided by P. ten Dijke (LUMC Leiden, NL). We thank I. Liang for help with fibroblast cell culture, K. David for help with MDA-MB-231 cell culture and F. Ramirez Gomez for help with the flow cytometry measurements. We thank S. ten Hagen for designing and printing the Peltier holder for the rheo-confocal setup. Flow cytometry measurements for HDF cells were kindly provided by I. Liang and J. Conboy. We thank C. Margadant (Leiden University) for his advice on the usage of the anti-integrin antibody.

SUPPLEMENTARY FIGURES

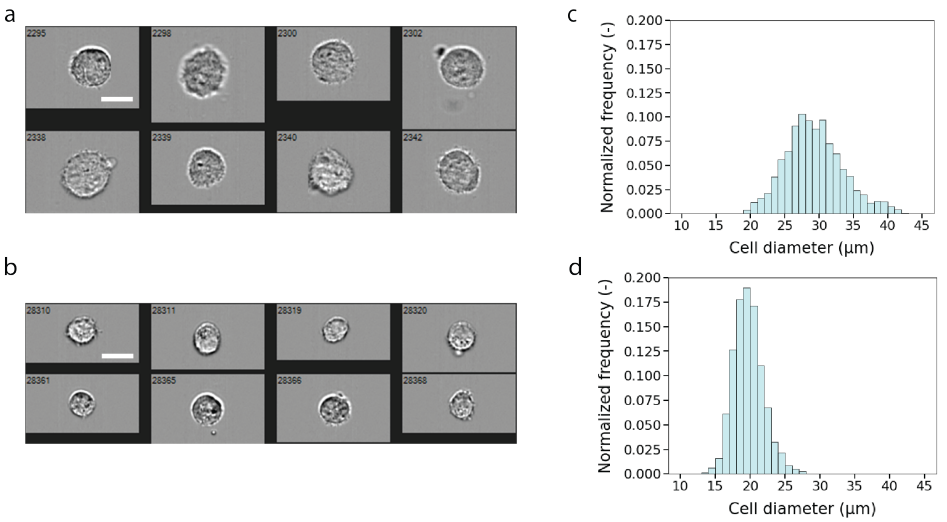

Figure S.3.1: **Cell diameter measurements for human dermal fibroblasts (HDF) and breast cancer cells (MDA-MB-231 Lifeact-GFP).** (a-b) Representative bright-field images of the HDF cells (a) and MDA-MB-231 Lifeact-GFP cells (b), both imaged in the flow cytometer. Scale bars are 20 μm. (c-d) Cell diameter distributions for HDF cells (c) and MDA-MB-231 Lifeact-GFP cells (d) measured by flow cytometry. The average cell diameter was 29.3 ± 4.2 μm for HDF cells (measured on 6,223 cells) and 19.7 ± 2.1 μm (mean ± SD) for MDA-MB-231 cells (measured on 13,234 cells).

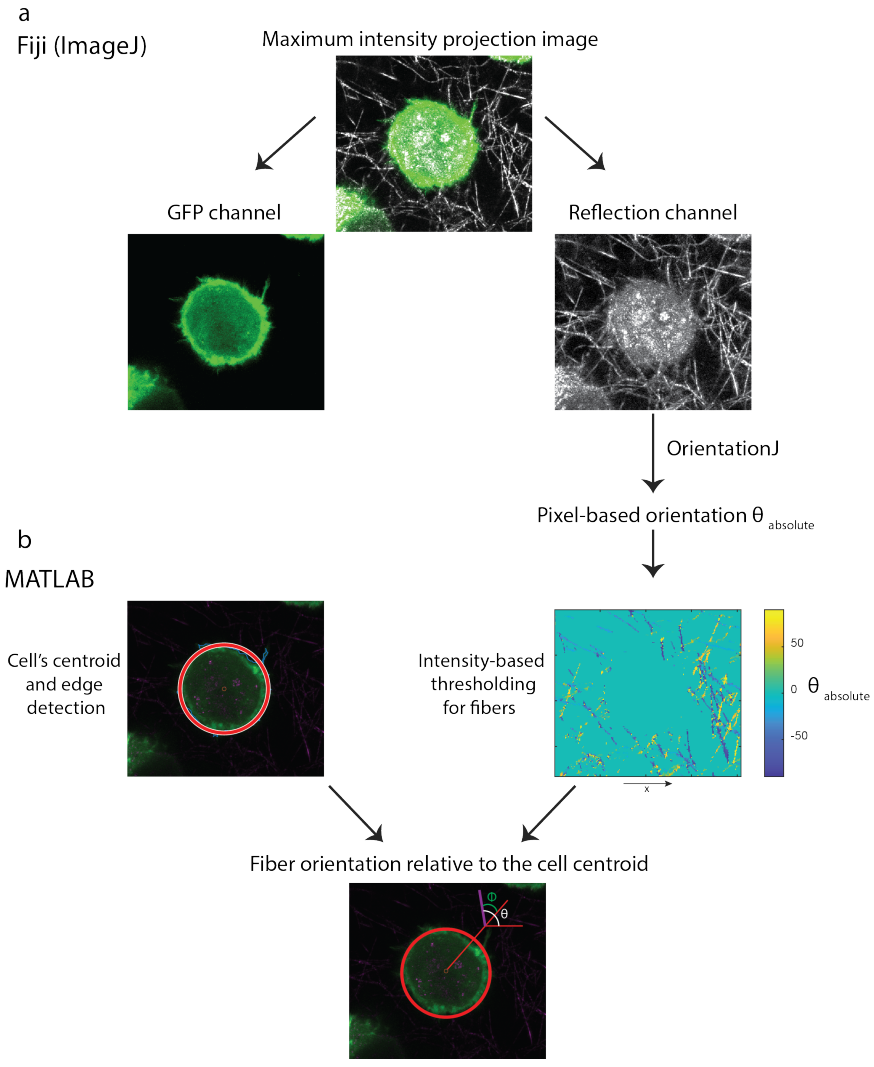

Figure S.3.2: **Schematic representation of the analysis pipeline for quantifying collagen fiber orientations relative to microparticles or cells.** (a) In ImageJ, a maximum intensity projection over a depth of 2 μm was obtained from Z-stacks. The GFP (actin) and the reflection channels were separated, and the OrientationJ plugin was applied to the reflection image (using the gaussian gradient and a local window σ of 1 pixel) to obtain pixel-based orientation angles ($\theta_{absolute}$) relative to the x-axis. (b) Left: Circular masks are generated based on the cell boundary (red) to define the reference centroid for orientation analysis. For microparticles, a circular shape was fitted to the boundary to create a binary mask, as they are not fluorescent. Right: The pixel locations corresponding to the cell/microparticle were subtracted from the OrientationJ output in order to process only pixels from collagen fibers. An intensity-based thresholding was applied (using the function imbinarize in MATLAB), to remove noisy orientation values. The colormap represents the extracted orientation values (θ_{absolute}) of the selected fibers. Bottom: The absolute orientation angles (θ_{absolute}, white) were converted into polar coordinates centered at the cell/microparticle centroid to determine the relative orientation ϕ (green) for each fiber pixel (example fiber in purple).

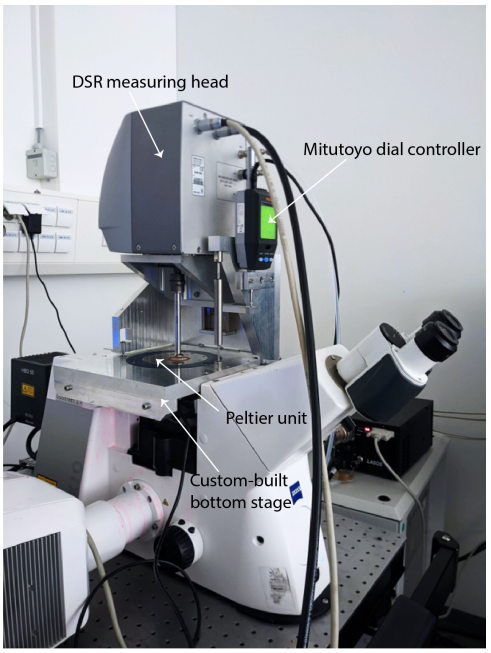

(a)

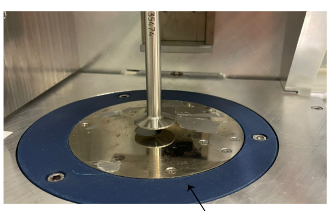

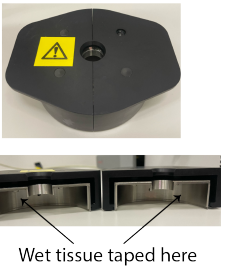

(b)

Figure S.3.3: **Rheo-confocal microscopy setup.** (a) Photograph of the setup shows the DSR rheometer measuring head mounted on a confocal microscope through a custom-built bottom stage that replaces the microscope's original XY-moving stage. The measuring gap is controlled by a Mitutoyo dial indicator, while the temperature is controlled by a Peltier unit, on which a glass coverslip is glued (red circle in the image) for sample deposition and imaging. (b) Left: The Peltier unit was mounted onto the rheometer bottom stage using a 3D-printed holder, made of polylactide (PLA). Right: A metal hood with wet tissues taped inside was placed around the measuring head to maintain humidity and prevent sample drying.

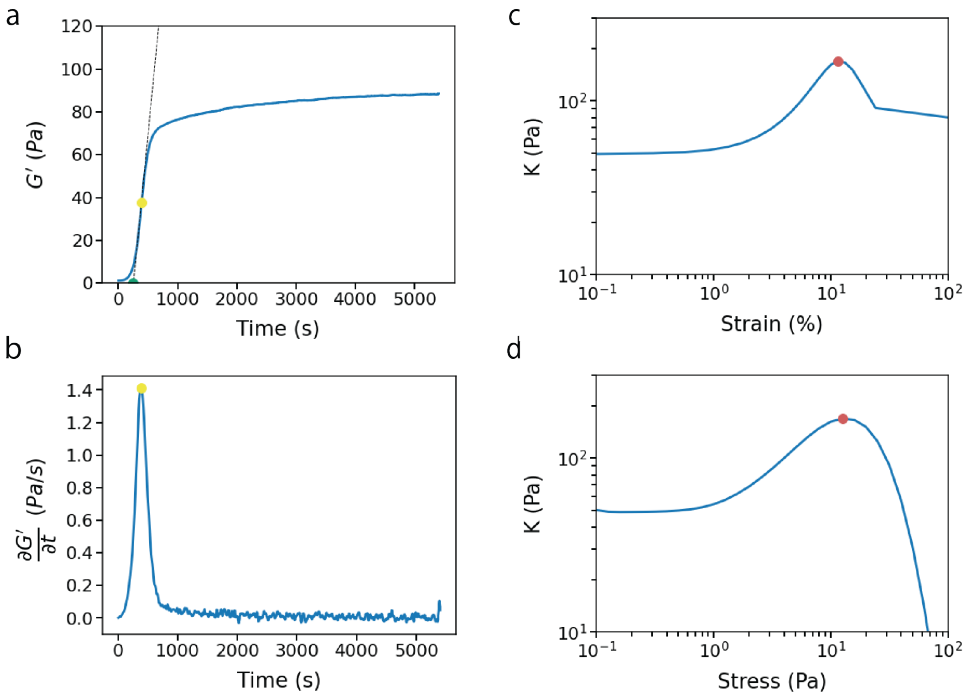

Figure S.3.4: **Determination of the onset time and strain/stress at rupture.** (a-b) Representative curves of the storage modulus G' (a) and the derivative of the storage modulus with respect to time $\frac{\partial G'}{\partial t}$ (b) as a function of time. The onset time (green point) is determined from the polymerization curve (a) as the intersection between the tangent (dashed black line) to the curve's inflection point (yellow point) and the time axis. The inflection point of the curve is determined as the maximum of $\frac{\partial G'}{\partial t}$. (c-d) Representative curves of the differential modulus K as a function of the strain γ (c) or the stress σ (d). The strain and stress at rupture are determined as the point where the differential modulus reaches its maximum value (red point).

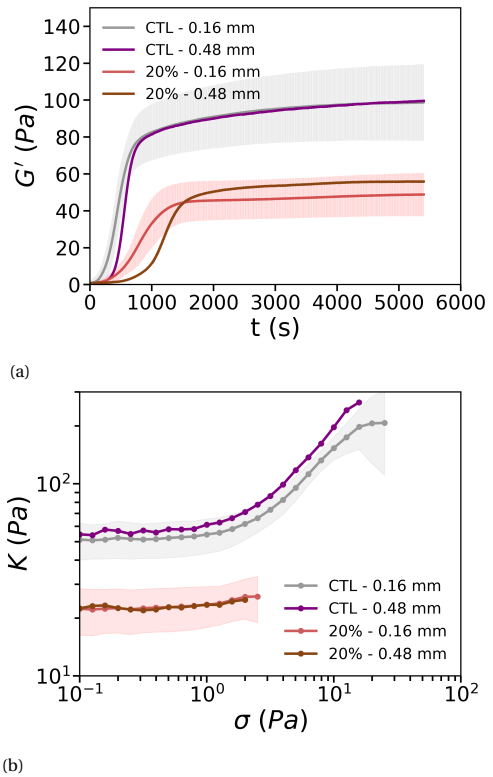

Figure S.3.5: **The measurement gap of the parallel plate geometry does not influence the bulk rheological properties of collagen networks.** (a) Time-dependent storage moduli $G'(t)$ during polymerization for control collagen networks and cancer cell-embedded networks (at 20% volume fraction of MDA-MB-231 cells) for two different gaps (0.16 mm and 0.48 mm). The longer delay before the onset of collagen polymerization for control networks and networks containing 20% cells observed when the gap is 0.48 mm gap is likely due to the larger sample volume deposited between the plates. (b) Corresponding stress-dependent differential moduli $K(\sigma)$ measured by applying a stress ramp to the mature networks. Curves are truncated at the rupture point. Comparable results are obtained for gaps of 0.16 mm (CTL: n=16, N=8 and 20%: n=16, N=8) and 0.48 mm (CTL and 20%: n=1, N=1), confirming that wall slip effects are negligible. Graphs in (a) and (b) represent mean ± SD.

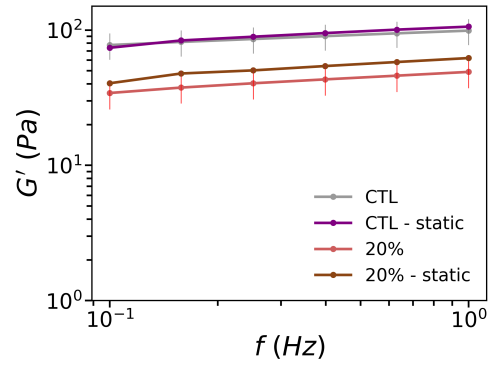

(a)

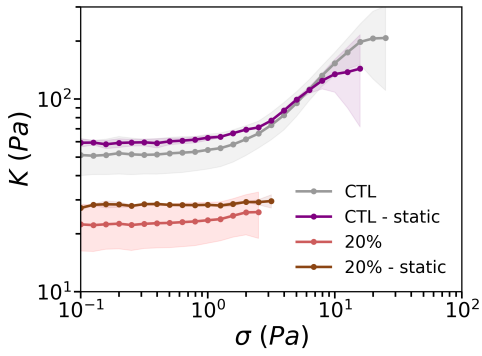

(b)

Figure S.3.6: **Rheological properties of collagen networks polymerized in static conditions *vs* small oscillatory strain conditions are identical.** (a) Storage moduli G' obtained from small amplitude oscillatory measurements at different frequencies for control collagen networks (CTL) and collagen networks containing cancer cells (at 20% volume fraction). (b) Corresponding differential moduli K as a function of applied stress stress σ for the final networks. Static conditions (labeled as *static*) refer to networks polymerized between the rheometer parallel plates at 37°C for 90 minutes without shearing, followed by frequency sweeps and stress ramps. The results in static conditions (CTL and 20%: n=2, N=1) are comparable to those obtained under oscillatory shear conditions (CTL: n=16, N=8 and 20%: n=16, N=8), confirming that the application of small shear oscillations during collagen polymerization does not affect the rheological properties of the network, neither for cell-free nor for cell-embedded networks. Graphs in (a) and (b) represent mean ± SD.

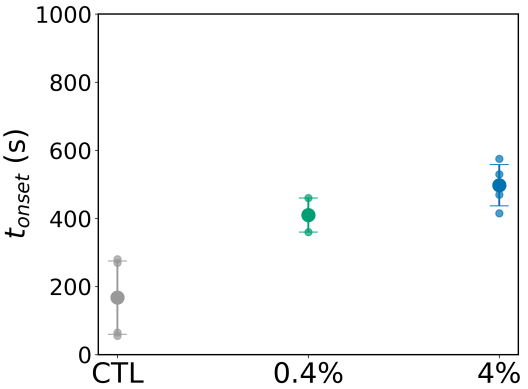

Figure S.3.7: **Onset of polymerization time t_{onset} determined from the increase of the storage modulus with time during polymerization of HDF-embedded collagen networks.** Cell-embedded networks containing HDF cells at volume fractions of 0.4% or 4% show a longer onset time than control networks (CTL). Data represent mean ± SD.

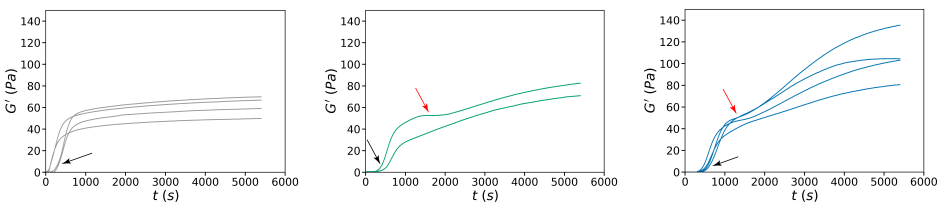

Figure S.3.8: **Time-dependent rheology data showing individual polymerization curves of collagen networks containing fibroblasts (HDF cells).** (a) Storage modulus G' as a function of time for control collagen (n=4, N=1). Curves show a monophasic increase of the modulus that sets in around 200 s (marked by black arrow). (b) Storage modulus G' as a function of time for collagen containing HDF cells at a volume fraction of 0.4% (n=2, N=1). (c) Storage modulus G' as a function of time for collagen containing HDF cells at a volume fraction of 4% (n=4, N=1). For consistency, the control collagen in (a) is prepared with the medium used for HDF cell culture. In the presence of cells, the polymerization curves tend to show a biphasic increase of the modulus, with a first onset corresponding to collagen polymerization (black arrows in b,c) and a second onset likely corresponding to force generation by the cells on the formed network (red arrows in b,c).

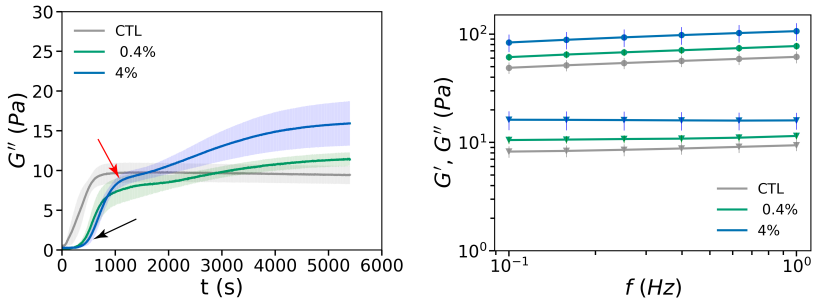

(a) (b)

Figure S.3.9: **Loss modulus G'' and frequency sweeps for collagen networks containing human dermal fibroblasts (HDF).** (a) Loss moduli during collagen polymerization for control collagen networks (CTL) and networks containing HDF cells at a volume fraction of 0.4% or 4%. Note that G'' increases with time in a monophasic way for the control network, whereas the increase is biphasic in the presence of cells (black arrow and red arrow). (b) Frequency dependence of the storage moduli (circles) and loss moduli (triangles) for mature networks. Graphs represent mean ± SD.

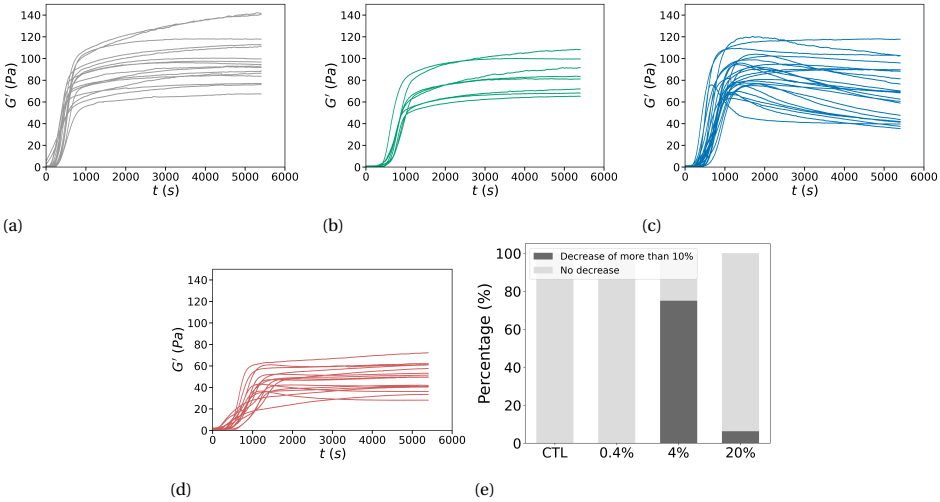

(a) (b) (c) (d) (e)

Figure S.3.10: **Individual polymerization curves of control and MDA-MB-231-embedded collagen matrices.** Curves show the storage modulus G' as a function of polymerization time. (a) Collagen only (n=16, N=8), prepared with MDA-MB-231 complete medium. (b-d) Cell-embedded collagen with cell volume fractions of (b) 0.4% (n=8, N=3), (c) 4% (n=24, N=10) and (d) 20% (n=16, N=8) respectively. Notably, in more than 75% of the 4% cell-embedded samples, the final G' value, at the end of the polymerization, decreased by at least 10% from its peak value, as shown in (e).

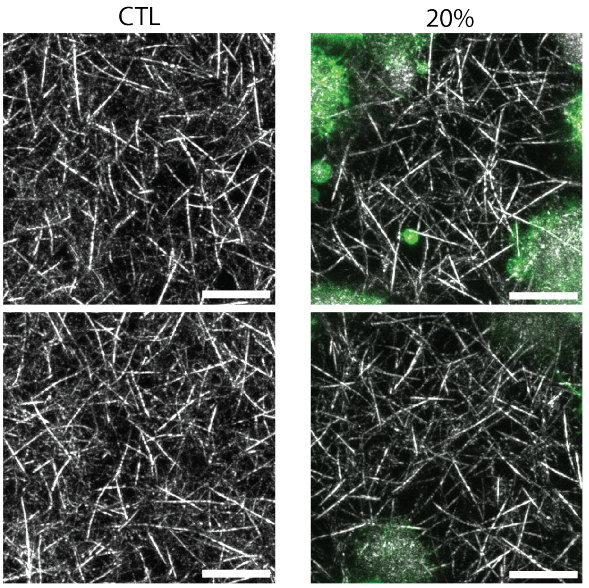

Figure S.3.11: **The collagen network structure is similar with and without the presence of MDA-MB-231 cancer cells.** Representative maximum intensity projection images (based on confocal stacks across a depth of 10 μm) of cell-free collagen hydrogels (CTL, left column) or collagen hydrogels with 20% volume fraction of MDA-MB-231 cells (20%, right column). Bottom and top rows show two different example regions of interest. Collagen fibers (grey) are imaged with reflection microscopy, while LifeAct-GFP tagged actin (green) is imaged with fluorescence microscopy. Scale bars are 10 μm.

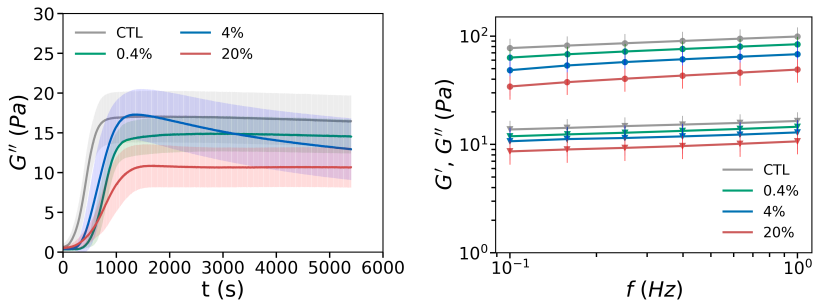

(a) (b)

Figure S.3.12: **Loss modulus G'' and frequency sweeps for collagen networks with embedded MDA-MB-231 cancer cells.** (a) Loss moduli G'' during the polymerization of collagen and MDA-MB-231-embedded collagen matrices at volume fractions of 0.4%, 4%, and 20%, showing trends similar to the storage moduli in Figure 1e of the main text. (b) Storage moduli G' (circles) and loss moduli G'' (triangles) from frequency sweep experiments on mature networks. Data represent mean ± SD.

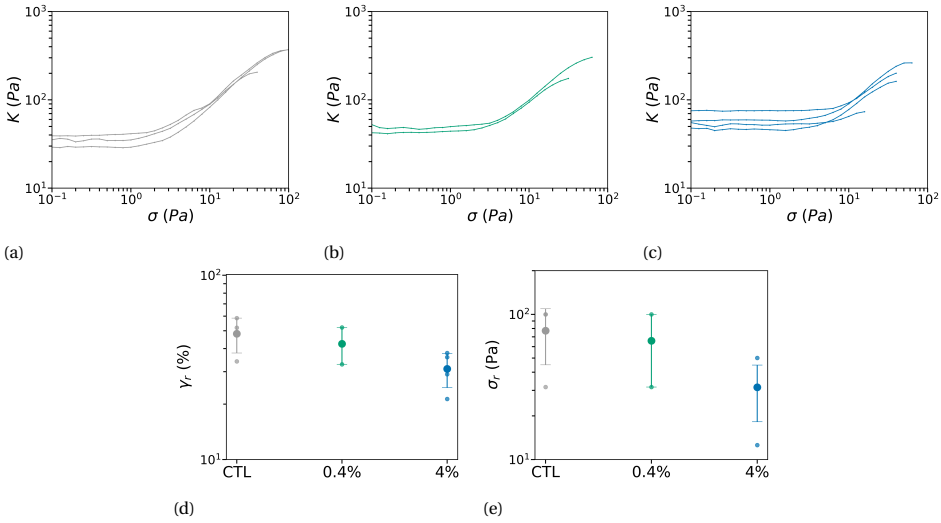

Figure S.3.13: **Individual stress ramp data for control collagen networks and HDF-embedded collagen matrices.** (a-c) Differential modulus K as a function of applied shear stress σ for (a) collagen alone (n=3, N=1), (b) collagen with HDFs at a volume fraction of 0.4% (n=2, N=1), and (c) HDFs at a volume fraction of 4% (n=4, N=1). The curves are truncated at the rupture point. All the samples exhibit stress-stiffening behavior. (d) Strain at rupture γ_r. (e) Stress at rupture σ_r. Data in (d) and (e) represent mean ± SD. The strain and stress at rupture values are not significantly different between collagen control networks and cell-embedded collagen networks.

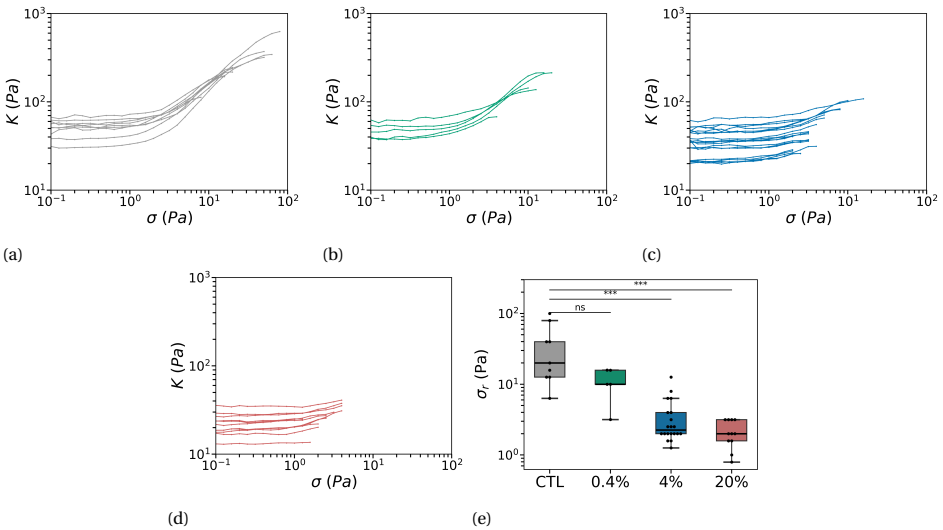

Figure S.3.14: **Individual stress ramp data for control collagen and MDA-MB-231-embedded collagen matrices.** (a-c) Differential modulus K as a function of applied shear stress σ for (a) collagen alone (n=9, N=4), (b) collagen with MDA-MB-231 cells at a volume fraction of 0.4% (n=5, N=2), (c) 4% (n=20, N=8), and (d) 20% (n=11, N=6). The curves are truncated at the rupture point. Samples in (a) and (b) exhibit stress-stiffening behavior, while samples in (c) and (d) do not. (e) Stress at rupture σ_r. Networks with 0.4% cell-embedded collagen samples behave the same as control networks, but networks with higher cell densities (4% and 20%) exhibit significantly lower values for the rupture stress compared to the control.

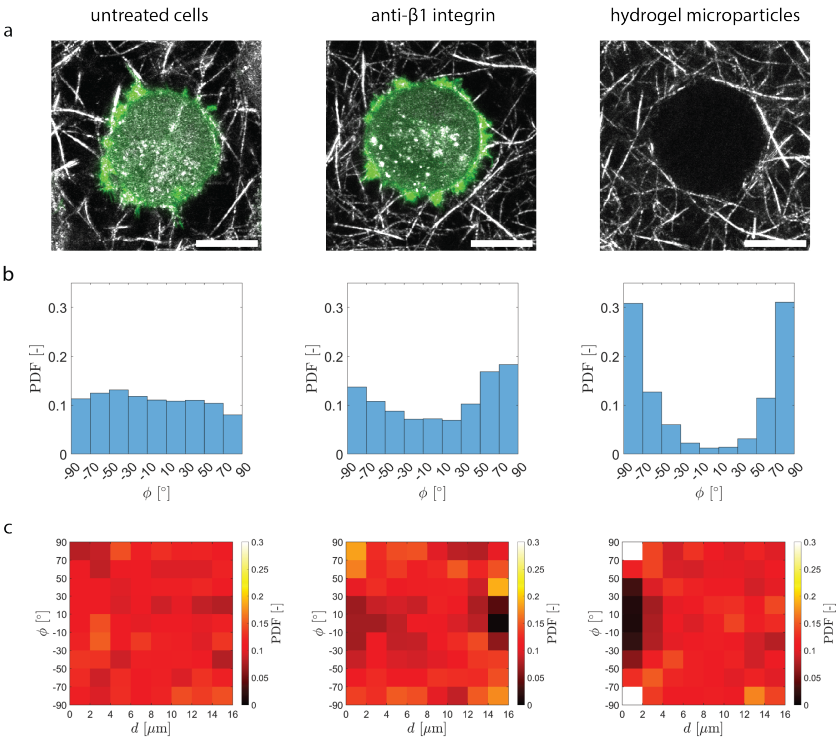

Figure S.3.15: **Orientation of collagen fibers around MDA-MB-231 cells or microparticles.** (a) Representative maximum intensity projections (2 μm) of confocal Z-stacks showing untreated cells, anti-β1 integrin-treated cells and hydrogel microparticles, and the surrounding collagen fibers. Collagen fibers (grey) are imaged by reflection microscopy while actin (green) is imaged by fluorescence microscopy. These images illustrate differences in fiber organization around the cells or microparticles. Scale bars are 10 μm. (b) Probability density function (PDF) of the orientation (ϕ) of collagen fibers relative to the cell or microparticle edge and located at a distance of 2 μm from the edge of untreated cells (left, n= 9, N=5), anti-β1 integrin-treated cells (middle, n=8, N=1), and hydrogel microparticles (right, n=10, N=1). For fibers tangential to the egde, $\phi = \pm 90°$, while for fibers perpendicular to the edge, $\phi = 0°$. Around the hydrogel microparticles, fibers are predominantly tangentially oriented ($\phi = \pm 90°$). Anti-β1 integrin-treated cells exhibit more tangentially oriented fibers compared to untreated cells, which instead display an isotropic fiber distribution. (c) Heatmaps displaying the probability density function (PDF) of the orientation (ϕ) of collagen fibers relative to the cell or microparticle edge as a function of the distance d from the edge of untreated cells (left), anti-β1 integrin-treated cells (middle), and hydrogel microparticles (right). In the immediate proximity of the cells or microparticles, fiber orientation varies depending on the condition, as highlighted in panel (b). However, above 4 μm distance from the edge, the orientation of collagen fibers becomes isotropic and randomly distributed.

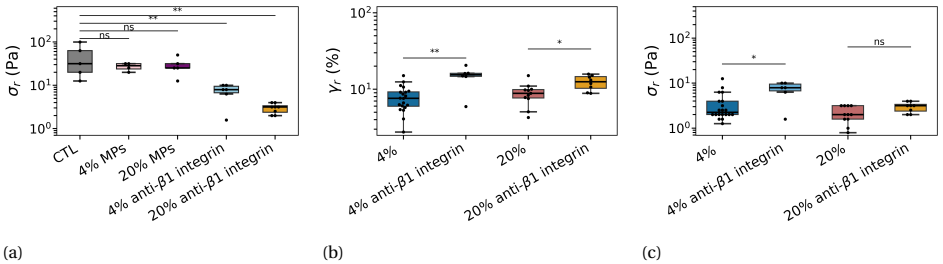

(a) (b) (c)

Figure S.3.16: **Stress at rupture for collagen alone, collagen embedded with soft hydrogel microparticles or with MDA-MB-231 cells with blocked β1 integrins.** (a) Boxplots of the stress at rupture σ_r measured for 0% (CTL), 4% and 20% volume fraction of microparticles or MDA-MB-231 cells with integrin-mediated adhesion blocked by anti-β1 integrin antibody. (b-c) Comparison of strain and stress at rupture of cell-embedded matrices (4% and 20% cell volume fractions) with and without blocked β1 integrins.

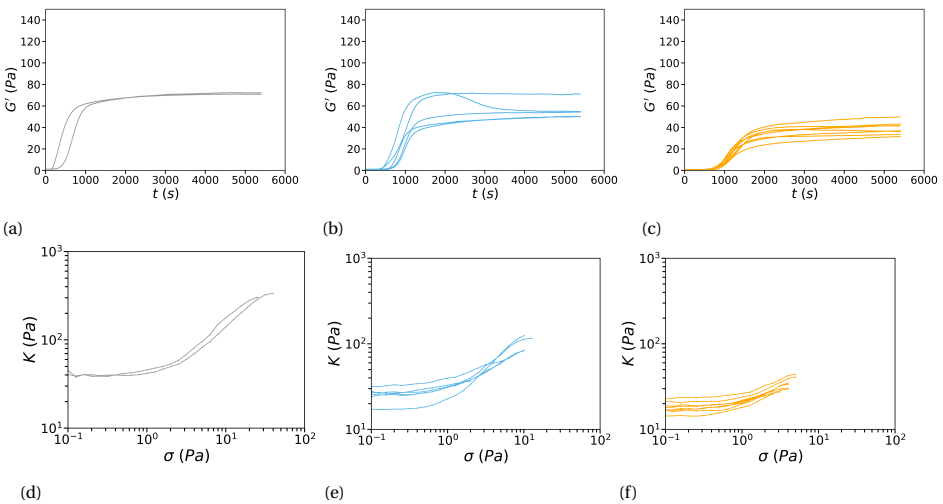

(a) (b) (c)

(d) (e) (f)

Figure S.3.17: **Individual polymerization curves and stress ramp data for collagen networks containing MDA-MB-231 cells with blocked β1 integrins.** Storage modulus G' as a function of polymerization time and differential modulus K as a function of the applied stress σ for collagen alone (n=2, N=1) (a,d), collagen with 4% cells with blocked β1 integrins (n=5, N=2) (b,e) and with 20% cells with blocked β1 integrins (n=8, N=2) (c,f). The K curves are truncated at the rupture point. Note that in presence of 4% cells (panel b), only one curve out of 5 shows a non-monotonic dependence of G' on time with a peak, in contrast to samples where adhesion is not blocked (Figure S.3.10c).

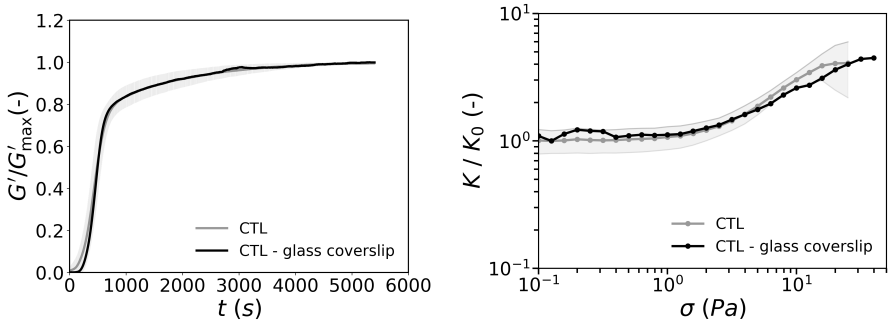

(a) (b)

Figure S.3.18: **Bulk rheology of collagen networks remains unchanged when the stainless steel bottom plate is replaced by a glass coverslip.** A glass coverslip (similar to the ones used for rheo-confocal microscopy) was glued on top of the bottom stainless steel plate of the rheometer. (a) Storage modulus G' normalized by its maximal value G'_{max} as a function of polymerization time for collagen deposited on the rheometer bottom plate (grey) (n=16, N=8) and on a glass coverslip (black, n=1, N=1). (b) Differential modulus K normalized by the linear modulus K_0 (determined as K at 0.1 Pa) as a function of applied shear stress σ for collagen deposited on the rheometer stainless steel bottom plate (grey, n=9, N=4) and on a glass coverslip (black, n=1, N=1).

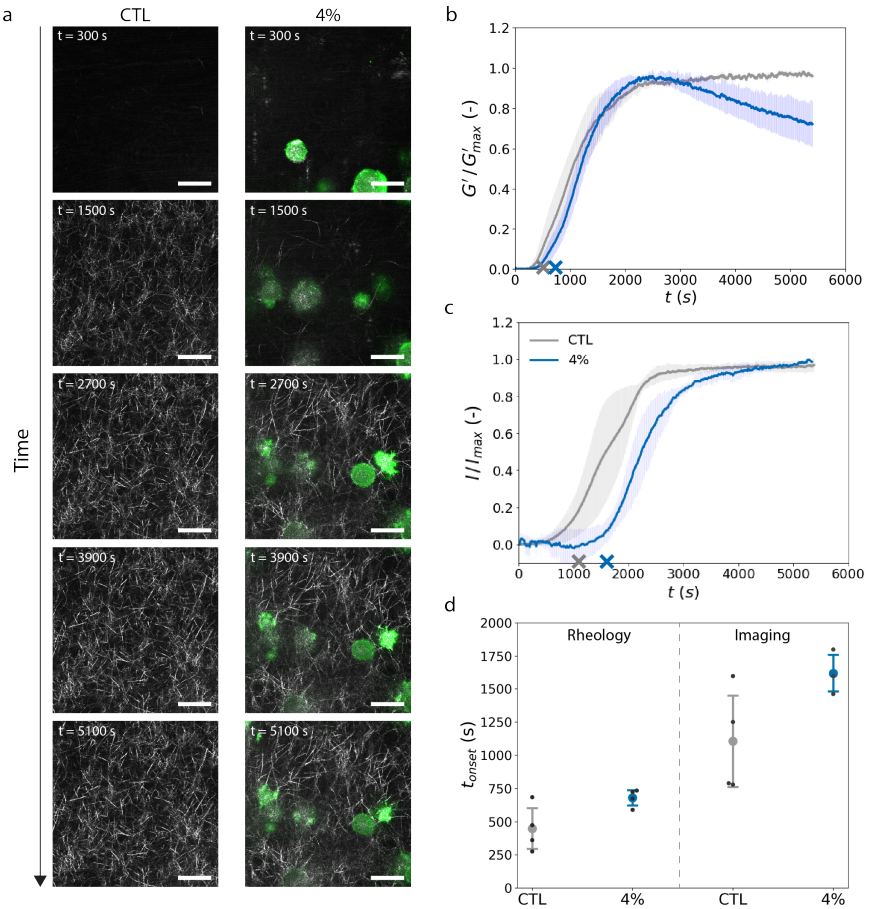

Figure S.3.19: **Confocal imaging and rheology measurements both demonstrate that cells delay the onset of collagen polymerization.** a) Representative time lapse confocal image series acquired for collagen mixed with 0% (CTL) cells or 4% MDA-MB-231 cells during polymerization. Collagen fibers (grey) are imaged by reflection microscopy while actin (green) is imaged by fluorescence microscopy using LifeAct-GFP tagging. Scale bars are 20 μm. b) Storage modulus normalized by its maximal value G'_{max} as a function of polymerization time for CTL networks and networks with 4% MDA-MB-231 embedded cells. c) Total intensity of the reflectance images of collagen normalized by the final value as a function of polymerization time for CTL networks and networks with 4% MDA-MB-231 embedded cells. Average onset times measured are indicated with crosses for CTL (grey) or 4% cells (blue) in (b) and (c). d) Onset polymerization times (t_{onset}) for CTL or 4% MDA-MB-231 embedded cells measured from the rheological measurements in panel (b) or from the imaging data in panel (c). Data represent mean ± SD. CTL: N = 4 and 4%: N = 3.

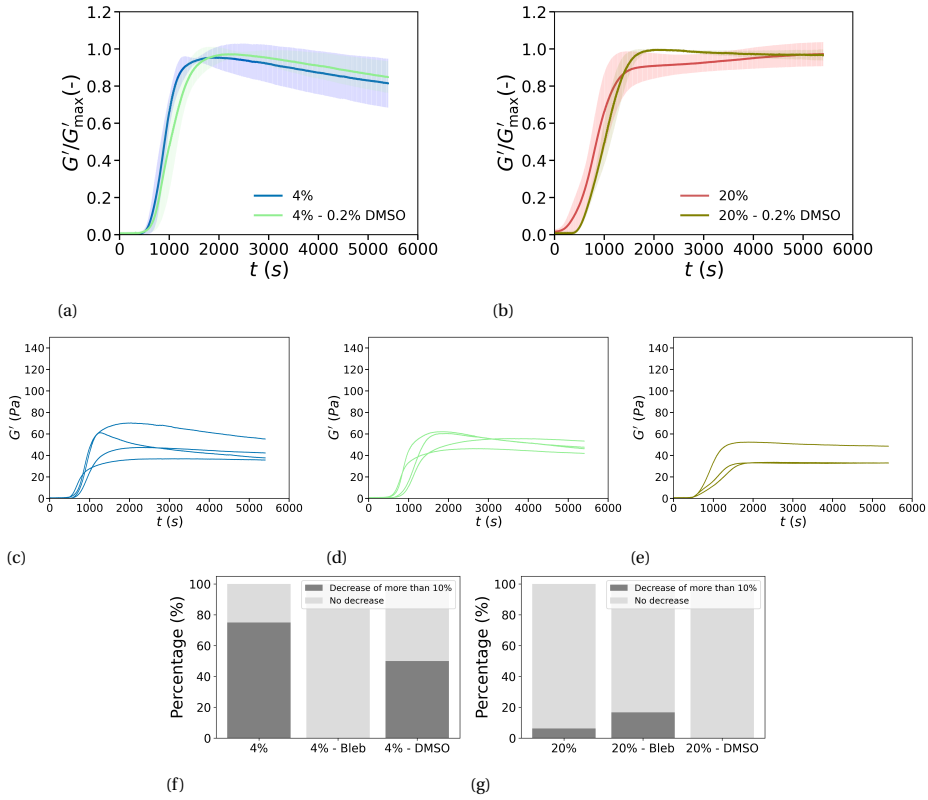

Figure S.3.20: **Control experiment showing that the presence of small amounts of DMSO, used as the solvent for the myosin-inhibiting drug blebbistatin, does not affect the bulk rheology of cell-embedded collagen.** (a,b) Storage modulus G' normalized by its maximum value G'_{max} as a function of polymerization time. (a) Comparison between networks with 4% MDA-MB-231 cells exposed to 0.2% DMSO (volume percentage) for 3 hours before cell detachment and the corresponding 4% control, without DMSO. (b) Comparison between networks with 20% cells exposed to DMSO and the entire dataset for 20% cells, without DMSO. Data represent mean ± SD. (c-e) Individual curves corresponding to the averaged data from (a,b) for the control experiment with 4% cells and no DMSO (c) (n=4, N=1), 4% cells exposed to 0.2% DMSO (d) (n=4, N=1), and 20% cells exposed to 0.2% DMSO (n=3, N=2). (f,g) Histograms depicting the percentage of polymerization curves exhibiting a peak with a decrease of G' of at least 10% compared to its peak value.

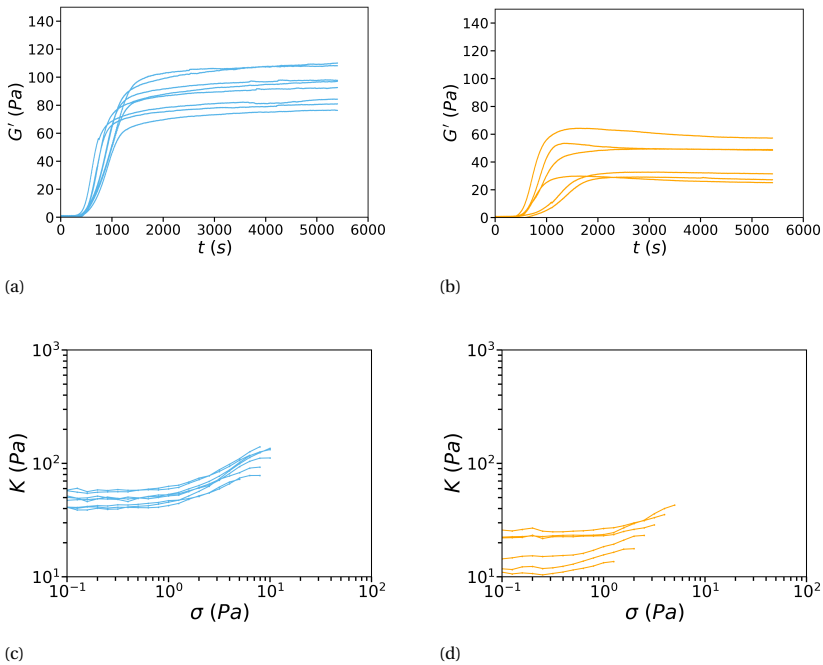

Figure S.3.21: **Individual polymerization curves and stress ramp data for collagen networks containing blebbistatin-treated MDA-MB-231 cells.** Storage modulus G' as a function of polymerization time and differential modulus K as a function of applied shear stress σ for collagen networks containing cells exposed to blebbistatin for 3 hours before cell passage at volume fractions of 4% (n=8, N=2) (a,c) and 20% cells (n=6, N=2) (b,d). The K curves are truncated at the rupture point.

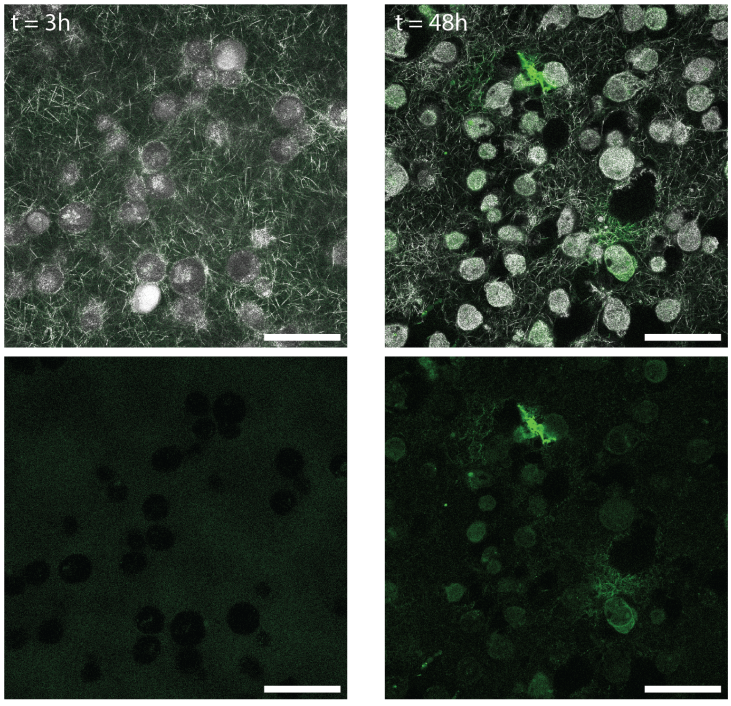

Figure S.3.22: **DQ-collagen assays indicate that MDA-MB-231 cells do not significantly degrade collagen on a 3 hour time scale.** Collagen networks containing 25 μg/mL of DQ-collagen were prepared to quantify proteolytic degradation of collagen by the cells. Collagen fibers and cells are visible in reflection microscopy (grey) while the degradation of collagen is assessed by imaging the fluorescence of DQ-collagen (green). Top panels show merged images, bottom panels show the fluorescence signal. While no degradation is observed after 3h, a clear degradation signal is visible on collagen fibers in the immediate surrounding of the cells after 48h. Scale bars are 50 μm.

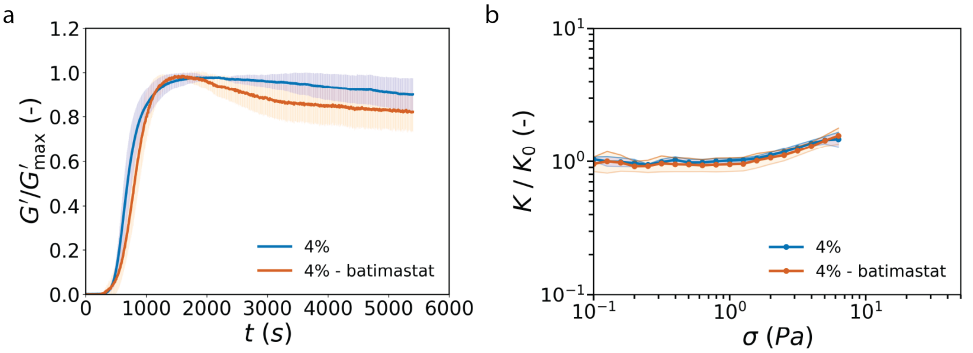

Figure S.3.23: **MMP inhibition with batimastat does not alter cell-mediated softening of collagen networks.** a) Storage modulus G' normalized by its maximum value G'_{max} as a function of polymerization time. Comparison between collagen networks with 4% MDA-MB-231 cells treated with 10 μM batimastat (orange; n = 3, N = 1) and untreated control samples (blue; n = 2, N = 1). A decrease of at least 10% from the peak G' was observed in all batimastat-treated samples, comparable to the control samples. b) Differential modulus K normalized by the linear modulus K_0 (determined as K at 0.1 Pa) for the steady-state networks with (orange, n = 2, N = 1) and without (blue, n = 2, N = 1) batimastat treatment. The non-monotonic behavior of G' in batimastat-treated samples and the overlap of the differential moduli curves both indicate that inhibiting metalloproteinase (MMP) activity does not alter the bulk rheology of collagen networks containing cells. Thus, the observed time-dependent softening is not driven by MMP-induced matrix degradation, suggesting that other cellular processes instead underlie the softening phenomenon.

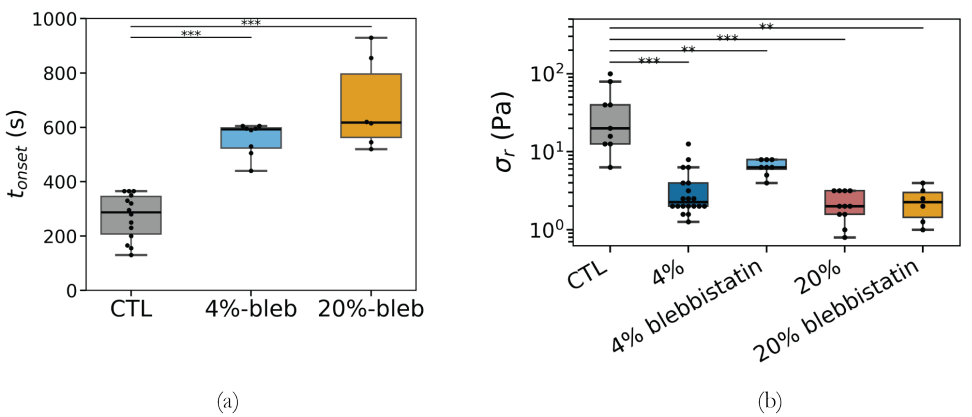

Figure S.3.24: **Onset time of collagen polymerization and shear stress at rupture for collagen networks containing blebbistatin-treated MDA-MB-231 cells.** (a) Onset time for collagen polymerization t_{onset} measured from rheology measurements for collagen mixed with cells exposed to blebbistatin for 3 hours before cell passage at volume fractions of 0% (CTL) (n=14, N=7), 4% (n=8, N=2), or 20% (n=6, N=2). (b) Boxplots of the stress at rupture σ_r, for cell-embedded collagen with and without blebbistatin treatment.

SUPPLEMENTARY VIDEOS

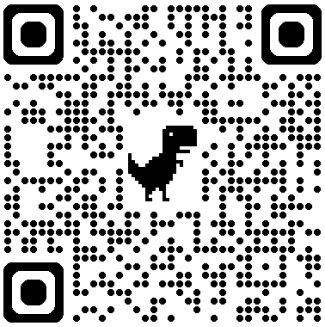

Supplementary video 1: Polymerization of a control collagen network imaged in the rheo-confocal set-up. Collagen fibers appearing over time (grey) are imaged by reflection microscopy. The visible oscillations over time are caused by the constant application of shear strain oscillations at a frequency of $1\,Hz$ and amplitude of 1%.

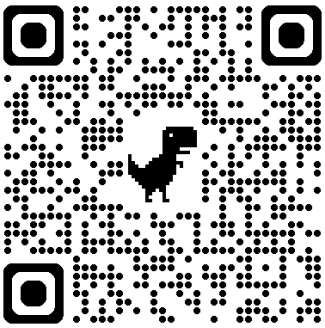

Supplementary video 2: Polymerization of a collagen network in presence of 4% volume fraction of MDA-MB-231 cells imaged in the rheo-confocal setup. Collagen fibers (grey) appearing over time are imaged by reflection microscopy and actin (green) is imaged by fluorescence microscopy. The visible oscillations over time are caused by the constant application of shear strain oscillations at a frequency of $1\,Hz$ and amplitude of 1%.

Supplementary video 3: Confocal imaging of cell-matrix interactions during polymerization of collagen in the presence of 4% MDA-MB-231 cancer cells acquired using the rheo-confocal setup. White arrows indicate cell-mediated remodeling events. Collagen fibers (grey) are imaged by reflection microscopy while actin (green) is imaged by fluorescence microscopy. The central arrow points at a cell protrusion pulling the fiber network and then retracting, while the top arrow indicates a fiber being bent by a cell.

Supplementary video 4: Confocal imaging of cell-matrix interactions during polymerization of collagen in the presence of 4% MDA-MB-231 cancer cells acquired using the rheo-confocal setup. White arrows indicate cell-mediated remodeling events. Collagen fibers (grey) are imaged by reflection microscopy while actin (green) is imaged by fluorescence microscopy. The arrow on the left indicates a cell protrusion that first displaces collagen fibers and then pulls on one individual collagen fiber. This pulling leads to the displacement of a crosslink node and to the bending of a fiber, indicated by the arrow on the right.

Supplementary video 5: Confocal imaging of cell-matrix interactions during polymerization of collagen in the presence of 4% MDA-MB-231 cancer cells acquired using the rheo-confocal setup. White arrows indicate cell-mediated remodeling events. Collagen fibers (grey) are imaged by reflection microscopy while actin (green) is imaged by fluorescence microscopy. Arrows indicate cell protrusions that displace collagen fibers and locally remodel the structure of the network.

Supplementary video 6: Confocal imaging during the shear stress ramp of a control collagen network acquired using the rheo-confocal set-up. A stress ramp is applied to the mature collagen network with stresses logarithmically increasing from 0.01 Pa to 100 Pa at a rate of 10 points per decade and with 5 s between each point. Collagen fibers (grey) are imaged by reflection microscopy. At early times corresponding to low stresses, there is no visible movement of the sheared network. After about 100 s, corresponding to an applied stress of 1 Pa, we observe a global displacement of the network to the right, corresponding to the direction of shear. The disappearance of the reflection signal from the collagen network for the final frames corresponds to the rupture point.

Supplementary video 7: Confocal imaging during the shear stress ramp of collagen in the presence of 4% MDA-MB-231 cancer cells acquired using the rheo-confocal set-up. A stress ramp is applied to the mature network with stresses logarithmically increasing from 0.01 Pa to 100 Pa at a rate of 10 points per decade and with 5 s between each point. Collagen fibers (grey) are imaged by reflection microscopy while actin (green) is imaged by fluorescence microscopy. A global displacement of the network in the direction of shear is visible. The collagen network and the cells seem to translate laterally in a similar manner. No clear differences in the local displacement of collagen fibers are evidenced when comparing to the stress ramp videos of control collagen network. The final frame of the video corresponds to the rupture point, indicated by the loss of actin fluorescence signal.

Supplementary video 8: Polymerization of collagen network in the presence of 20% volume fraction of microparticles (MPs) imaged in the rheo-confocal setup. Collagen fibers (grey) appearing over time are imaged by reflection microscopy, while the MPs appear as voids within collagen fibers. The visible oscillations over time are caused by the constant application of shear strain oscillations at a frequency of 1 Hz and amplitude of 1%. Collagen fibers appear in random locations and no preferential nucleation of collagen fibers around the microparticles can be observed.

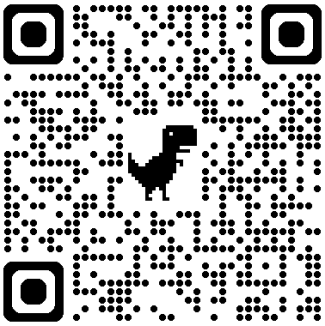

Supplementary video 9: Confocal imaging during the shear stress ramp in the presence of 20% volume fraction of microparticles (MPs) imaged in the rheo-confocal setup. A stress ramp is applied to the mature network with stresses logarithmically increasing from 0.01 Pa to 100 Pa at a rate of 10 points per decade and with 5 s between each point. Collagen fibers (grey) are imaged by reflection microscopy, while the MPs appear as voids within collagen fibers. A global displacement of the network in the direction of shear is visible. The collagen network and the MPs seem to translate laterally in a similar manner, with no deformation of the MPs up to about 10 Pa (corresponding to time point 2:30 of the stress ramp). After this point and right before rupture, the holes in the collagen network seem to expand. The final frame of the video corresponds to the rupture point, corresponding to 20 Pa in this example.

REFERENCES

[1] K. Saini, S. Cho, M. Tewari, A. Jalil, M. Wang, A. Kasznel, K. Yamamoto, D. Chenoweth, and D. Discher, *Pan-tissue scaling of stiffness versus fibrillar collagen reflects contractility-driven strain that inhibits fibril degradation,* bioRxiv preprint (2023), 10.1101/2023.09.27.559759.

[2] N. K. Karamanos, A. D. Theocharis, Z. Piperigkou, D. Manou, A. Passi, S. S. Skandalis, D. H. Vynios, V. Orian-Rousseau, S. Ricard-Blum, C. E. Schmelzer, L. Duca, M. Durbeej, N. A. Afratis, L. Troeberg, M. Franchi, V. Masola, and M. Onisto, *A guide to the composition and functions of the extracellular matrix,* FEBS Journal **288**, 6850 (2021).

[3] C. Frantz, K. M. Stewart, and V. M. Weaver, *The extracellular matrix at a glance,* Journal of Cell Science **123**, 4195 (2010).

[4] X. Di, X. Gao, L. Peng, J. Ai, X. Jin, S. Qi, H. Li, K. Wang, and D. Luo, *Cellular mechanotransduction in health and diseases: from molecular mechanism to therapeutic targets,* Signal Transduction and Targeted Therapy **8** (2023), 10.1038/s41392-023-01501-9.

[5] K. M. Yamada, A. D. Doyle, and J. Lu, *Cell–3D matrix interactions: recent advances and opportunities,* Trends in Cell Biology **32**, 883 (2022).

[6] C. Bonnans, J. Chou, and Z. Werb, *Remodelling the extracellular matrix in development and disease,* Nature Reviews Molecular Cell Biology **15**, 786 (2014).

[7] J. D. Humphrey, E. R. Dufresne, and M. A. Schwartz, *Mechanotransduction and extracellular matrix homeostasis,* Nature Reviews Molecular Cell Biology **15**, 802 (2014).

[8] L. J. Dooling, K. Saini, A. A. Anlaş, and D. E. Discher, *Tissue mechanics coevolves with fibrillar matrisomes in healthy and fibrotic tissues,* Matrix Biology **111**, 153 (2022).

[9] M. Van Dijk, S. A. Göransson, and S. Strömblad, *Cell to extracellular matrix interactions and their reciprocal nature in cancer,* Experimental Cell Research **319**, 1663 (2013).

[10] P. J. Asif, C. Longobardi, M. Hahne, and J. P. Medema, *The role of cancer-associated fibroblasts in cancer invasion and metastasis,* Cancers **13**, 4720 (2021).

[11] T. Wakatsuki, M. S. Kolodney, G. I. Zahalak, and E. L. Elson, *Cell mechanics studied by a reconstituted model tissue,* Biophysical Journal **79**, 2353 (2000).

[12] Guy M. Genin, Teresa M. Abney, Tetsuro Wakatsuki, and Elliot L. Elson, *Cell-Cell Interactions and the Mechanics of Cells and Tissues Observed in Bioartificial Tissue Constructs,* in *Mechanobiology of Cell-Cell and Cell-Matrix* (Springer US, 2011) Chap. 5, pp. 75–103.

[13] J. K. Kular, S. Basu, and R. I. Sharma, *The extracellular matrix: Structure, composition, age-related differences, tools for analysis and applications for tissue engineering,* Journal of Tissue Engineering **5**, 1743 (2014).

[14] A. J. Licup, S. Münster, A. Sharma, M. Sheinman, L. M. Jawerth, B. Fabry, D. A. Weitz, and F. C. MacKintosh, *Stress controls the mechanics of collagen networks,* Proceedings of the National Academy of Sciences **112**, 9573 (2015).

[15] A. S. van Oosten, X. Chen, L. K. Chin, K. Cruz, A. E. Patteson, K. Pogoda, V. B. Shenoy, and P. A. Janmey, *Emergence of tissue-like mechanics from fibrous networks confined by close-packed cells,* Nature **573**, 96 (2019).

[16] J. L. Shivers, J. Feng, A. S. G. Van Oosten, H. Levine, P. A. Janmey, and F. C. Mackintosh, *Compression stiffening of fibrous networks with stiff inclusions,* Proceedings of the National Academy of Sciences **117**, 21037 (2020).

[17] B. Carroll, M. T. H. Thanh, and A. E. Patteson, *Dynamic remodeling of fiber networks with stiff inclusions under compressive loading,* Acta Biomaterialia **163**, 106 (2023).

[18] T. Wakatsuki and E. L. Elson, *Reciprocal interactions between cells and extracellular matrix during remodeling of tissue constructs,* Biophysical Chemistry **100**, 593 (2002).

[19] J. P. Marquez, E. L. Elson, and G. M. Genin, *Whole cell mechanics of contractile fibroblasts: Relations between effective cellular and extracellular matrix moduli,* Philosophical Transactions of the Royal Society A: Mathematical, Physical and Engineering Sciences **368**, 635 (2010).

[20] G. Baneyx, L. Baugh, and V. Vogel, *Fibronectin extension and unfolding within cell matrix fibrils controlled by cytoskeletal tension,* PNAS **99**, 5139 (2002).

[21] C. J. Dalton and C. A. Lemmon, *Fibronectin: Molecular structure, fibrillar structure and mechanochemical signaling,* Cells **10**, 2443 (2021).

[22] A. Zhmurov, A. E. Brown, R. I. Litvinov, R. I. Dima, J. W. Weisel, and V. Barsegov, *Mechanism of fibrin(ogen) forced unfolding,* Structure **19**, 1615 (2011).

[23] A. Malandrino, M. Mak, R. D. Kamm, and E. Moeendarbary, *Complex mechanics of the heterogeneous extracellular matrix in cancer,* Extreme Mechanics Letters **21**, 25 (2018).

[24] T. R. Cox, *The matrix in cancer,* Nature Reviews Cancer **21**, 217 (2021).

[25] C. Verdier and L. I. Palade, *A rheological model for spheroids including extra-cellular matrix,* EPL **145** (2024), 10.1209/0295-5075/ad1d6f.

[26] Y. L. Han, P. Ronceray, G. Xu, A. Malandrino, R. D. Kamm, M. Lenz, C. P. Broedersz, and M. Guo, *Cell contraction induces long-ranged stress stiffening in the extracellular matrix,* Proceedings of the National Academy of Sciences **115**, 4075 (2018).

[27] R. Rodrigues de Mercado, K. Beslmüller, D. Vorselen, E. H. Danen, and T. Schmidt, *Single-Cell Local Stress Analysis in Tumoroids,* arXiv preprint (2024), 10.1101/2024.01.22.576025.

[28] A. F. Straight, A. Cheung, J. Limouze, I. Chen, N. J. Westwood, J. R. Sellers, and T. J. Mitchison, *Dissecting Temporal and Spatial Control of Cytokinesis with a Myosin II Inhibitor,* Science **299** (2003), 10.1126/science.1081412.

[29] H. M. Zhang, H. H. Ji, T. Ni, R. N. Ma, A. Wang, and X. D. Li, *Characterization of Blebbistatin Inhibition of Smooth Muscle Myosin and Nonmuscle Myosin-2,* Biochemistry **56**, 4235 (2017).

[30] T. Kelly, Y. Yan, R. L. Osborne, A. B. Athota, T. L. Rozypal, J. C. Colclasure, and W. S. Chu, *Proteolysis of extracellular matrix by invadopodiafacilitates human breast cancer cell invasion and ismediated by matrix metalloproteinases,* Clin Exp Metastasis **16**, 501 (1998).

[31] C. Jedeszko, M. Sameni, M. B. Olive, K. Moin, and B. F. Sloane, *Visualizing protease activity in living cells: From two dimensions to four dimensions,* Current Protocols in Cell Biology **39** (2008), 10.1002/0471143030.cb0420s39.

[32] R. Rezakhaniha, A. Agianniotis, J. T. Schrauwen, A. Griffa, D. Sage, C. V. Bouten, F. N. Van De Vosse, M. Unser, and N. Stergiopulos, *Experimental investigation of collagen waviness and orientation in the arterial adventitia using confocal laser scanning microscopy,* Biomechanics and Modeling in Mechanobiology **11**, 461 (2012).

[33] J. Schindelin, I. Arganda-Carreras, E. Frise, V. Kaynig, M. Longair, T. Pietzsch, S. Preibisch, C. Rueden, S. Saalfeld, B. Schmid, J. Y. Tinevez, D. J. White, V. Hartenstein, K. Eliceiri, P. Tomancak, and A. Cardona, *Fiji: An open-source platform for biological-image analysis,* Nature Methods **9**, 676 (2012).

[34] E. Fabiano, J. Zhang, and C. A. Reinhart-King, *Tissue density in the progression of breast cancer: Bedside to bench and back again,* Current Opinion in Biomedical Engineering **22**, 100383 (2022).

[35] J. M. Mcpherson, D. G. Wallace, S. J. Sawamura, A. Conti, R. A. Condell, S. Wade, and K. A. Piez, *Collagen Fibrillogenesis In Vitro: A Characterization of Fibril Quality as a Function of Assembly Conditions,* Collagen and Related Research **5** (1985), 10.1016/S0174-173X(85)80034-0.

[36] K. E. Sung, G. Su, C. Pehlke, S. M. Trier, K. W. Eliceiri, P. J. Keely, A. Friedl, and D. J. Beebe, *Control of 3-dimensional collagen matrix polymerization for reproducible human mammary fibroblast cell culture in microfluidic devices,* Biomaterials **30**, 4833 (2009).

[37] A. Sharma, A. J. Licup, K. A. Jansen, R. Rens, M. Sheinman, G. H. Koenderink, and F. C. Mackintosh, *Strain-controlled criticality governs the nonlinear mechanics of fibre networks,* Nature Physics **12**, 584 (2016).

[38] F. Burla, Y. Mulla, B. E. Vos, A. Aufderhorst-Roberts, and G. H. Koenderink, *From mechanical resilience to active material properties in biopolymer networks,* Nature Reviews Physics **1**, 249 (2019).

[39] J. Cooper and F. G. Giancotti, *Integrin Signaling in Cancer: Mechanotransduction, Stemness, Epithelial Plasticity, and Therapeutic Resistance,* Cancer Cell **35**, 347 (2019).

[40] F. Mustapha, K. Sengupta, and P. H. Puech, *Protocol for measuring weak cellular traction forces using well-controlled ultra-soft polyacrylamide gels,* STAR Protocols **3** (2022), 10.1016/j.xpro.2022.101133.

[41] J. Kumai, S. Sasagawa, M. Horie, and Y. Yui, *A Novel Method for Polyacrylamide Gel Preparation Using N-hydroxysuccinimide-acrylamide Ester to Study Cell-Extracellular Matrix Mechanical Interactions,* Frontiers in Materials **8** (2021), 10.3389/fmats.2021.637278.

[42] X. Pang, X. He, Z. Qiu, H. Zhang, R. Xie, Z. Liu, Y. Gu, N. Zhao, Q. Xiang, and Y. Cui, *Targeting integrin pathways: mechanisms and advances in therapy,* (2023).

[43] C. F. Bohren and D. R. Huffman, *Absorption and scattering of light by small particles* (Wiley, 1998).

[44] A. Saraswathibhatla, D. Indana, and O. Chaudhuri, *Cell–extracellular matrix mechanotransduction in 3D,* Nature Reviews Molecular Cell Biology **24**, 495 (2023).

[45] A. M. Douglas, A. A. Fragkopoulos, M. K. Gaines, L. A. Lyon, A. Fernandez-Nieves, and T. H. Barker, *Dynamic assembly of ultrasoft colloidal networks enables cell invasion within restrictive fibrillar polymers,* Proceedings of the National Academy of Sciences **114**, 885 (2017).

[46] W. L. Ng, M. H. Goh, W. Y. Yeong, and M. W. Naing, *Applying macromolecular crowding to 3D bioprinting: Fabrication of 3D hierarchical porous collagen-based hydrogel constructs,* Biomaterials Science **6**, 562 (2018).

[47] B. Geiger and K. M. Yamada, *Molecular architecture and function of matrix adhesions,* Cold Spring Harbor Perspectives in Biology **3**, 1 (2011).

[48] R. Borst, L. Meyaard, and M. I. Pascoal Ramos, *Understanding the matrix: collagen modifications in tumors and their implications for immunotherapy,* Journal of Translational Medicine **22** (2024), 10.1186/s12967-024-05199-3.

[49] G. Forgacs, S. A. Newman, B. Hinner, C. W. Maier, and E. Sackmann, *Assembly of collagen matrices as a phase transition revealed by structural and rheologic studies,* Biophysical Journal **84**, 1272 (2003).

[50] N. W. Tam, R. Dimova, and A. Cipitria, *Breast cancer cell-derived extracellular vesicles accelerate collagen fibrillogenesis and integrate into the matrix,* bioRxiv preprint (2024), 10.1101/2024.08.08.607183.

[51] D. Böhringer, A. Bauer, I. Moravec, L. Bischof, D. Kah, C. Mark, T. J. Grundy, E. Görlach, G. M. O'Neill, S. Budday, P. L. Strissel, R. Strick, A. Malandrino, R. Gerum, M. Mak, M. Rausch, and B. Fabry, *Fiber alignment in 3D collagen networks as a biophysical marker for cell contractility,* Matrix Biology **124**, 39 (2023).

[52] A. Padhi, K. Singh, J. Franco-Barraza, D. J. Marston, E. Cukierman, K. M. Hahn, R. K. Kapania, and A. S. Nain, *Force-exerting perpendicular lateral protrusions in fibroblastic cell contraction,* Communications Biology **3** (2020), 10.1038/s42003-020-01117-7.

[53] K. A. Jansen, R. G. Bacabac, I. K. Piechocka, and G. H. Koenderink, *Cells actively stiffen fibrin networks by generating contractile stress,* Biophysical Journal **105**, 2240 (2013).

[54] A. Jagiełło, M. Lim, and E. Botvinick, *Dermal fibroblasts and triple-negative mammary epithelial cancer cells differentially stiffen their local matrix,* APL Bioengineering **4** (2020), 10.1063/5.0021030.

[55] J. Pokki, I. Zisi, E. Schulman, D. Indana, and O. Chaudhuri, *Magnetic probe-based microrheology reveals local softening and stiffening of 3D collagen matrices by fibroblasts,* Biomedical Microdevices **23** (2021), 10.1007/s10544-021-00547-2.

[56] H. I. Yang, E. I. Berthier, C. Li, P. I. Ronceray, Y. Long Han, C. P. Broedersz, S. I. Cai, and M. Guo, *Local response and emerging nonlinear elastic length scale in biopolymer matrices,* Proceedings of the National Academy of Sciences **120** (2023), 10.1073/pnas.

[57] S. Goren, B. Ergaz, D. Barak, R. Sorkin, and A. Lesman, *Micro-tensile rheology of fibrous gels quantifies strain-dependent anisotropy,* Acta Biomaterialia **181**, 272 (2024).

[58] J. L. Shivers, S. Arzash, and F. C. Mackintosh, *Nonlinear Poisson Effect Governed by a Mechanical Critical Transition,* Physical Review Letters **124** (2020), 10.1103/PhysRevLett.124.038002.

[59] J. L. Shivers, A. Sharma, and F. C. Mackintosh, *Strain-Controlled Critical Slowing Down in the Rheology of Disordered Networks,* Physical Review Letters **131** (2023), 10.1103/PhysRevLett.131.178201.

[60] M. Sarkar, B. M. Burkel, S. M. Ponik, and J. Notbohm, *Unexpected softening of a fibrous matrix by contracting inclusions,* Acta Biomaterialia **177**, 253 (2024).

[61] E. D'Arcangelo, N. C. Wu, J. L. Cadavid, and A. P. McGuigan, *The life cycle of cancer-associated fibroblasts within the tumour stroma and its importance in disease outcome,* British Journal of Cancer **122**, 931 (2020).

[62] A. Iordan, A. Duperray, A. Gérard, A. Grichine, and C. Verdier, *Breakdown of cell-collagen networks through collagen remodeling,* Biorheology **47**, 277 (2010).

4

Conclusion and Outlook

Tissue mechanics play a critical role in cancer progression and metastasis, influencing processes such as tumor growth, invasion, and dissemination [1, 2]. This chapter summarizes the key findings from the previous chapters of this dissertation, which investigated the rheological properties of breast tumors and their surrounding environment, under relevant biophysical conditions. To unravel the viscoelastic characteristics of biological model systems, we employed two different experimental approaches.

In **Chapter 2**, multicellular aggregates - referred to as 3D multicellular spheroids - were formed from three different types of breast cancer cell types. These spheroids were analyzed within a microfluidic chip featuring a constricted middle channel, enabling the characterization of their viscoelastic properties and relaxation behavior. Two physical models were applied to extract key mechanical parameters, providing insights into how cancer cell type influences spheroid deformation and recovery.

Chapter 3 focused on understanding how highly invasive cancer cells alter the mechanical properties of their surrounding extracellular matrix, by directly measuring the bulk rheological properties of tissue-mimicking systems. Among the three previously studied cell lines, the highly invasive breast cancer cell (MDA-MB-231) line was selected. These cells were suspended in collagen I matrices at varying cell volume fractions, and the bulk rheological properties of the cell-laden hydrogels were characterized using a rotational rheometer. This approach allowed for a systematic evaluation of how cell density impacts the macroscopic mechanical behavior of the extracellular matrix and demonstrated that cells actively remodel the network mechanics in an integrin-mediated, adhesion-dependent manner.

This thesis brings together multiple experimental strategies to study the rheological properties of breast cancer at different scales. It combines 3D *in vitro* models, like microfluidic platforms and spheroids, and hydrogel-based matrices to recreate the extracellular matrix. Furthermore, the use of pharmacological inhibitors—such as blebbistatin (a myosin II ATPase inhibitor) and anti-β1 integrin antibodies— enabled the investigation of cellular mechanisms governing tissue mechanics. By adopting this interdisciplinary approach, this research addresses the core questions outlined in **Chapter 1**. The following sections revisit these questions, discuss the implications of the findings, and suggest potential directions for future research.

4.1. VISCOELASTICITY AND RELAXATION TIMESCALES ACROSS CANCER MALIGNANCIES

In **Chapter 2**, we examined the viscoelastic properties of breast cancer spheroids with varying metastatic potential in a microfluidic chip equipped with a middle constriction and a relaxation chamber. An important aspect of this work was the adaptation of an existing physical model to the dynamic pressure conditions of our microfluidic setup. We introduced a modified version of such model, termed the **Dynamic Modified Maxwell Model**, which allowed us to extract quantitative measures of spheroid elasticity (E) and viscosity (η). Our key findings revealed that benign MCF-10A spheroids exhibit higher bulk elastic modulus (E) and viscosity (η) compared to their malignant counterparts (MCF-7 and MDA-MB-231). These results highlight that the viscoelastic properties of breast cancer spheroids reflect those of their constituent cells and reinforce the concept

that increasing malignancy is associated with decreased stiffness and viscosity, also at the multicellular level. Notably, the viscoelastic parameters of the benign spheroids are significantly strain-dependent, while the malignant spheroids display little to no sensitivity to changes in strain. This suggests that the apparent viscoelastic behavior of breast cancer spheroids is influenced by both the imposed mechanical conditions and their metastatic potential. We were unable to distinguish the two malignant cell lines from their viscoelastic properties, despite their different biological behaviors. However, a key distinction between these two types of spheroid was evident during the relaxation phase.

The relaxation phase was characterized by two distinct timescales: an early-time fast relaxation (characterized by τ_1) associated with surface elasticity and a late-time slow relaxation (characterized by τ_2) related to bulk elasticity. MCF-10A and MCF-7 spheroids, which exhibit a well-defined peripheral actin rim and maintain a spherical shape, demonstrated faster initial relaxation compared to MDA-MB-231 spheroids. Immunostaining revealed that MDA-MB-231 spheroids lack this actin organization, which likely contributes to their slower surface-driven relaxation. This finding suggests that the structural arrangement of actin fibers at the spheroid periphery plays a critical role in shaping the early-time mechanical response. Although both MCF-7 and MDA-MB-231 exhibit similar values of τ_2, the latter presents a broader range of residual deformations due to its increased cell mobility at the cell periphery. We hypothesize that the absence of E-cadherin-mediated adhesions in MDA-MB-231 spheroids facilitates cells' rearrangements, making them more prone to irreversible deformation and fragmentation under high compression, as confirmed by spheroid rupture and cell dissemination under high compression levels for such spheroids.

4.1.1. FUTURE RESEARCH DIRECTIONS

From a broader perspective, our findings imply that the biophysical properties of breast cancer spheroids reflect their metastatic potential. Benign spheroids exhibit greater stiffness, viscosity, and resistance to deformation, whereas malignant spheroids, particularly those with high metastatic potential, are more deformable and prone to irreversible structural changes. These mechanical characteristics can have clinical relevance, as they provide a physical framework for understanding how primary tumors can be classified and diagnosed based on their malignancy. By quantifying key mechanical parameters, a distinction can be made between benign and malignant tumors, providing clinicians with a complementary diagnostic approach alongside traditional histopathological methods [3]. Furthermore, monitoring changes in these properties over time could provide insights into tumor progression and therapeutic response. In line with this idea, an existing company, ARTIDIS®, has developed a nanomechanical sensor that captures the physical properties of tumor cells and their microenvironment with high accuracy, enabling the differentiation between benign and malignant tissues, based on the samples' physical properties, within 3 hours. Similarly, Optics11 Life's technology addresses the mechanical differences between healthy and malignant cells, as well as changes in the tumor's mechanical environment during progression. Their approach aims at evaluating the effectiveness of anticancer drugs at reducing stiffness and restoring normal tissue function, but also supports the development of physiologically relevant 3D in vitro models.

To enhance the future applicability of the microfluidic platform presented here, the experimental framework should be therefore expanded to more physiologically relevant tissues. This could involve studying heterogeneous spheroids that more accurately represent the diverse cellular composition of real tumors or incorporating patient-derived biopsy samples [4, 5]. Furthermore, incorporating additional experimental techniques such as two-photon or spinning disk confocal microscopy [6] could facilitate imaging of cell membranes, enabling assessment of cell-cell rearrangements, or the variations in E-cadherin levels post-compression [7]. In conclusion, this microfluidic-based platform offers a robust and versatile tool for probing three-dimensional cellular aggregates of different tissue origins. By elucidating the relationship between spheroid mechanics and metastatic potential, this research lays the groundwork for future studies aimed at leveraging mechanical biomarkers for cancer diagnosis, prognosis, and treatment.

4.2. INFLUENCE OF CELL EMBEDDING ON COLLAGEN RHEOLOGY

In **Chapter 3** we investigated how cell-embedding affects the macroscopic bulk properties of collagen matrices. Specifically, we examined the behavior of human dermal fibroblasts (HDFs) and invasive breast cancer cells (MDA-MB-231) within collagen hydrogels at a concentration of 4 mg/mL. The polymerization process of these cell-embedded networks occurred under small amplitude oscillatory strain, imposed by shear rheometers. The results revealed contrasting outcomes depending on the embedded cell type: fibrobalsts caused stiffening of the collagen network already at low cell volumes (0.4%), whereas invasive cancer cells induced softening, accompanied by a distinctive non linear, time- dependent trend in storage modulus G' at cell densities of 4%. The strong contractile nature of HDFs, observed in previous studies with collagen and fibrin hydrogels, likely drives network stiffening by applying pre-stress to collagen fibers. Interestingly, for cancer cell volume fraction of 4%, the typical stress stiffening behavior of collagen matrices was disrupted and the network stress-induced rupture was characterized by lower strain and stress at rupture, compared to cell-free collagen. This indicated that MDA-MB-231 cells not only alter the mechanical response, but also weaken the structural integrity of the network under stress. We also observed a consistent delay in collagen polymerization across all density conditions. This delay may be attributed to the physical volume occupied by the cells, which could increase the time required for individual collagen fibers to form a network-spanning structure.

The unexpected softening effect and disruption of collagen stress-stiffening observed with MDA-MB-231 cells led us to further investigate into which mechanisms governs these changes in the collagen network. By embedding passive polyacrylamide beads at concentrations equivalent to the cells, we observed neither the non-linear, time-dependent behavior of G' nor the loss of stress stiffening in the collagen network. From this results, we hypothesize that cell adhesion to collagen fibers plays a pivotal role in these distinct mechanical behaviors. To confirm this, inhibition of MDA-MB-231 cell adhesion using a $\beta 1$ integrin antibody restored the stress stiffening response and eliminated the non-linear, time-dependent modulus trend during polymerization. Through the assembly of a rheo-confocal setup, which combines simultaneous rheological measurements with

live confocal imaging, dynamic interactions between cells and collagen fibers were observed, where cells actively engaged with their F-actin to remodel and bend collagen fibers. Blocking contractility with blebbistatin restored stress-stiffening only at lower cell densities (4%), while this effect diminished at higher densities (20%). This suggests that both adhesion to collagen fibers and F-actin-mediated contractility are required to alter the macroscopic behavior of the collagen network. However, at higher cell volume fractions, the mere presence of cells becomes the dominant factor via a volume-exclusion effect, disrupting collagen matrix formation, impairing stress-stiffening, and causing softening for non-contractile cell embedding.

4.2.1. FUTURE RESEARCH DIRECTIONS

This study demonstrates how local cell-ECM interactions influence the macroscopic behavior of collagen matrices, with cell type-specific effects observed as the network polymerization begins. This highlights the importance of considering the significant changes in network rheology given by cells when designing experiments involving cell-embedded matrices. Specifically, stiffness or Young's modulus values obtained in cell-free conditions may not accurately represent the true conditions of matrices with cells (above a certain concentration). A promising extension of this work would involve longer observation times of collagen-cell interactions in the rheo-confocal setup. Cancer cells are known to both deposit and degrade collagen through metalloproteinases (MMPs) [8], making it highly valuable to investigate the rheological changes in the ECM when these processes are activated. However, such studies were not feasible in the current setup due to experimental limitations, as the system was not allocated in an incubator, where CO_2, humidity and temperature could be properly monitored. Furthermore, improving the temperature control in the existing setup would enhance the accuracy of rheological measurements: an internal temperature regulation within the rheometer would prevent the establishment of temperature gradients between the bottom and top plates, which resulted in some discrepancies between the measurements taken on temperature-controlled rheometers and those in the rheo-confocal setup. Additionally, using fluorescent collagen, as attempted in some final experiments show in Figure 4.1, would significantly improve the resolution imaging compared to the reflection mode, enabling clearer tracking of collagen fibers and their interactions with cells.

An important step forward would involve the use of high-resolution, high-speed imaging to allow for more detailed observation of polymerization dynamics and long-range interactions between cells and collagen fibers across the sample thickness. Expanding the field of view would also enable better imaging of these processes through the entire sample. This setup can also be combined with actice or passive microrheology techniques, allowing for the assessment of both bulk and local rheological properties, to provide a holistic view of how microscale mechanical responses drive the macroscale material behavior, offering deeper insights into the correlation between physical properties and structural dynamics of complex biological matrices. The work can extend beyond cancer research and be applied to other biological contexts, such as wound healing, morphogenesis, bone repair [9]. Understanding how local cell-ECM interactions influence the macroscopic behavior of collagen (or other) matrices provides a valuable framework for studying various biological processes where mechanical cues play a crucial role.

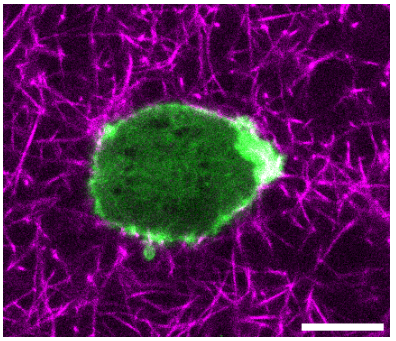

Figure 4.1: **MDA-MB-231 cell in fluorescent collagen** Snapshot of a MDA-MB-231 cells LifeAct GFP (green) embedded in a fluorescent collagen network (magenta). The collagen solution was pre-mixed with DyLight550 antibody at a concentration of 25% (v/v) to stain collagen fibers.The resulting images provide a better resolution and fiber detection compared to reflection imaging employed in Chapter 3.

REFERENCES

[1] H. T. Nia, L. L. Munn, and R. K. Jain, *Physical traits of cancer,* Science **370**, eaaz0868 (2020).

[2] M. K. Hayward, J. M. Muncie, and V. M. Weaver, *Tissue mechanics in stem cell fate, development, and cancer,* (2021).

[3] K. A. Papavassiliou, E. K. Basdra, and A. G. Papavassiliou, *The emerging promise of tumour mechanobiology in cancer treatment,* European Journal of Cancer **190** (2023), 10.1016/j.ejca.2023.112938.

[4] N. Dadgar, A. M. Gonzalez-Suarez, P. Fattahi, X. Hou, J. S. Weroha, A. Gaspar-Maia, G. Stybayeva, and A. Revzin, *A microfluidic platform for cultivating ovarian cancer spheroids and testing their responses to chemotherapies,* Microsystems and Nanoengineering **6** (2020), 10.1038/s41378-020-00201-6.

[5] N. V. Kosheleva, Y. M. Efremov, P. I. Koteneva, I. V. Ilina, I. M. Zurina, P. Y. Bikmulina, A. I. Shpichka, and P. S. Timashev, *Building a tissue: Mesenchymal and epithelial cell spheroids mechanical properties at micro- and nanoscale,* Acta Biomaterialia **165**, 140 (2023).

[6] S. L. Tlili, F. Graner, and H. Delanoë-Ayari, *A microfluidic platform to investigate the role of mechanical constraints on tissue reorganization,* Development **149** (2022), 10.1242/dev.200774.

[7] K. V. Iyer, R. Piscitello-Gómez, J. Paijmans, F. Jülicher, and S. Eaton, *Epithelial Viscoelasticity Is Regulated by Mechanosensitive E-cadherin Turnover,* Current Biology **29**, 578 (2019).

[8] A. Bhattacharya, K. Alam, N. S. Roy, K. Kaur, S. Kaity, V. Ravichandiran, and S. Roy, *Exploring the interaction between extracellular matrix components in a 3D organoid*

disease model to replicate the pathophysiology of breast cancer, Journal of Experimental and Clinical Cancer Research **42** (2023), 10.1186/s13046-023-02926-4.

[9] K. A. Jansen, R. G. Bacabac, I. K. Piechocka, and G. H. Koenderink, *Cells actively stiffen fibrin networks by generating contractile stress,* Biophysical Journal **105**, 2240 (2013).

Propositions

accompanying the dissertation

MECHANOBIOLOGY OF BREAST CANCER

A RHEOLOGICAL APPROACH FROM SPHEROIDS TO EXTRACELLULAR MATRIX

by

Margherita TAVASSO

1. The viscoelastic properties of breast cancer spheroids reflect the ones of their constituent single cells.
   This proposition pertains to chapter 2 of this thesis.

2. Assessing merely the deformability of cancer spheroids overlooks key biophysical properties across malignancies that can be revealed through stress relaxation measurements.
   This proposition pertains to chapter 2 of this thesis.

3. Measuring the rheological bulk properties of cell-free hydrogels leads to inaccurate estimates of such properties in cell-embedded conditions.
   This proposition pertains to chapter 3 of this thesis.

4. A rheoconfocal setup could be used for microrheology experiments, extending its application to probe localized mechanical behavior.

5. The biophysical properties of cancer are dependent on the technique employed to measure them, often allowing for qualitative comparisons, but not quantitative.
   (Agrawal et al., npj Biol.Phys.Mech., 2025).

6. The time required to optimize a microfluidic device is often underestimated and crucial methodological aspects are poorly reported in research papers.

7. PhD candidates should increase their awareness of how public funds are invested in their research.

8. It is unlikely for a first-year PhD candidate to create a reliable Gantt chart for the upcoming 3.5 years.

9. While scientific progress has enabled the acquisition of a black hole image, it still fails into accurately predicting the weather forecast of the next 10 minutes.

10. The approach to science, much like that to life, varies depending on scale and perspective.

These propositions are regarded as opposable and defendable, and have been approved by the promotors dr. Pouyan E. Boukany and prof. dr. Valeria Garbin

ACKNOWLEDGEMENTS

At the close of this memorable four-year journey, I find myself reflecting on all the people who, whether directly or indirectly, have shaped my growth, offered their support, inspired me and challenged me. First of all, thanks to the two people that took me under their wing and made my PhD experience possible and unforgettable, my supervisors and promotors. With heartfelt gratitude, thank you **Pouyan** for the trust you put in me from our very first online meeting and for believing in my capabilities to take on your beloved project. Thank you for your constant guidance and support, for always keeping the door open whenever I had a question or concern. Your mentorship shaped my scientific curiosity, my confidence and perseverance. **Valeria**, thank you for always offering different perspectives whenever needed, for helping me stay balanced and focused. Thanks for your kindness, the encouragement and the meticulous attention to detail that your careful eyes never missed.

Gijsje, our collaboration has been an immensely fulfilling experience, I learned so much from you. Thank you for your kindness, your generosity with time and advice and for always being so readily available to offer guidance and support.

Ankur, you made it all the way up here, but you know very well that our relationship grew into a great friendship beyond the workplace. Your arrival in PPE truly shaped my PhD journey, I could write pages about how fundamental your presence has been. A simple thank you would never suffice. We created so many unforgettable memories: the 21 beers at Brouwhuis and the trip to Marseille have a special place in my heart.

Irène, I cannot imagine a better person to work with than you. Your energy, enthusiasm and passion are truly contagious. Even on the most frustrating days, when experiments wouldn't work, being together in the lab made everything easier. I am very proud of our collaboration and of the paper we produced together. **Anouk**, even though our paths only overlapped briefly, it was always a pleasure to work with you. You were always so approachable, willing to help and generous in sharing your knowledge. **Kristen**, thanks for being such a fundamental figure in the lab and for making the hours spent there much more pleasant with our chats. The lab work wouldn not have been as "easy" without you.

Thanks to **Leslie**, **Ruud**, **Gabrie**, **Volkert**, **Alina**, **Caas**, **Duco**, **Stephan**, **Tony**, **Arthur**, **Ana** for making PPE/PSE such a welcoming and enjoyable workplace. Thank you for openly sharing your work and life experiences, for being so approachable, helpful and kind. I have learned something valuable from each of you.

A big thank you to the students I was honoured to supervise: **Eliz**, **Mostafa**, **Elsa** and **Sanne**. Guiding you through such an important step in your academic journey was an incredibly rewarding learning experience for me. I hope that, in the process, you were able to take away something valuable as well from me.

Zaid, we had an immediate connection from the moment we met and I never imagined I could find my corresponding male version at work. Thank you for always having my back, for the genuine friendship we share, for the fun and silly moments and for the gym motivation. You are one of the first people I want to share things with, whether big or small. Lastly, thank you for standing by my side as my paranymph and closing

this PhD chapter together. **Aswin**, behind the serious look lies the biggest, purest heart. Thanks for being such a good friend, for your presence, for the uncountable sweets, ice creams, chicken bites we had, for all the kilometers we walked talking about life. You are the brightest person I know and I am sure one day I will brag to the world that I am your friend. **Isabel** and **Lukas**, thank you for opening the doors of your home to the new girl in the group and for the fun nights spent playing board games, though I could never quite remember the rules! I wish you and **Cleo** a lifetime of happiness together. And thank you **Dominik** for delighting us with your homemade pizzas and keeping us laughing with your jokes during the games. **Ruben**, in the end, there was no reason not to get along. I am truly happy that we share so many fun moments together now. Thank you for making my karaoke dream come true and for trusting me enough to let me wax your hairy back! **Pranav** and **Albert**, I can confidently say that you make two of my favourite dishes in the world. Thanks for taking care of our bellies and for hosting so many evenings that brought us all closer. **Rens**, thank you for always being genuinely yourself and for providing the reassuring certainty that at 12:00 the office door would open for lunch, even on days when the PhD journey was full of uncertainties. Jokes aside, I deeply cherish our fun moments together and I'm glad that Napolitan cuisine is the only one your sensitive belly can handle. **Lena**, my wonderfully crazy friend, I am so happy to have met you! Our Craft&Create sessions are a true stress-relief therapy and the Aperol ones bring pure (orange) happiness. Fun with you is always guaranteed, as is the certainty that I can count on you at any moment. That is why it could only be you standing by my side as my paranymph. I am looking forward to our Austro-Napolitan trip! **Riccardo**, to me the office life marks your arrival as Year 0. What did we do before you entertained us with all sorts of conversations? Who was reaching first the workplace in the morning? Thanks for your precious advice when planning experiments and making paper figures, for patiently listening to all the complaints, for cheering for the successes and for being such a caring, kindly-hearted friend. Your silly jokes will always make me laugh. **Marc**, I am still waiting for the moment you will successfully scare me! Thank you for the constant teasing and laughs. One day, I will join you bouldering or surfing (maybe). **Simone**, thank you for your (sometimes brutally honest) advice, for always being present and available. You are my lab clean-freak heir and I am confident you will not disappoint me. **Sophie**, the The Script concert was such a spontaneous and amazing experience we shared, I will never forget it. Thank you for always being incredibly kind, you truly have a heart of gold. **Qing**, I needed a super girly presence in the office to share nail art and fashion advice with and I found you! Thank you for being so funny, enthusiastic and generous. **Gürhan**, briefly sharing the office with you was such a pleasure. Thanks for all the advice during the job search. You are a true gentleman and I loved exchanging cultural stories with you. Speaking of gentlemen, **Saeed**, thank you for not leaving PPE with your heart and for still being around. It's as if you never left us and I am truly happy about that. Thanks to **Mahdiyeh**, **Meryl**, **Hardlife**, **Nassim**, **Peter**, **Christian Ignasi**, **Gao**, **Dominik**, **Giacomo**, **Max**, **Sophia**, **Angga**, **Doğa**, **Athina**, **Bhavesh**, **Kalani**, **Dorian**, **Lucas P.**, **Suzanne**, **Rafaella**, for all the fun moments at work and outside work, for being each of you a different and unique part of the group. A special mention goes to **Ida**, for being the kindest person anyone could ever meet. Thank you for checking on us in the lab, for our endless conversations, for the support and strength we shared and for being such a won-

derful friend. I miss walking around Delft with you and Anuar. I also want to mention **Lukas**, our dancing at the Jazz Festival was such a freeing and joyful moment, thanks for hosting cocktail-making evenings. **Tanuj**, thanks for introducing me to Joppie sauce and always being ready for fun, spontaneous adventures and a cone with Alpaco!

It is now time for family acknowledgments, so dear reader, I will switch to my mother tongue.

Mamma, **Papà**, lo so quanto sia stato difficile per voi salutarmi quel 4 Gennaio in aeroporto, sapermi lontana, ma libera. Ed è questo quello che mi avete sempre insegnato. Essere libera di essere, fare, conoscere, osare, sbagliare. Voi e **Raffa** siete la mia forza motrice. Vi amo infinitamente e un grazie non sarà mai abbastanza.

Raffa, grazie per mostrare affetto per entrambe, visto che io spesso gioco il ruolo dell'anaffettiva tra le due. Sei un'ispirazione e un esempio da seguire per me. Grazie per esserci sempre e per farmi sentire ancora la sorellina da proteggere.

Mariangela, mia sorella acquisita, grazie per l'amore che ci scambiamo in un modo tutto nostro. Tormentarti sarà sempre il mio passatempo preferito.

Grazie alle colonne portanti della mia famiglia, i nonni. **Nonna Lella**, **Nonno Pasquale**, mi mancheranno i vostri "auguri felicissimi". Quando un raggio di sole si fa spazio tra le nuvole, mi piace pensare che siate voi. **Nonna Maggie**, **Nonno Peppe**, se potessi, giocherei a burraco ogni pomeriggio e ascolterei all'infinito tutte le vostre storie di vita. La vostra scienziata, come mi chiamate, vi deve tutto.

Grazie alla tutta la mia famiglia, per essere sempre unita e forte, divertente e a tratti stramba. Un grazie particolare a **zia Ivana**, per essere la zia confidente e fiera sostenitrice delle sue nipoti.

Carola, **Ivana**, **Oriana**, **Kekko**, siamo nati e cresciuti tenendoci per mano e tra un nascondino e una corsa lungo le colline toscane, le nostre mani non si sono mai lasciate. Tra gioie e successi, ma anche dolori e avversità, la nostra amicizia rimane una promessa per tutta la vita.

Marika e **Carmen**, ci siamo trovate e da allora il nostro legame non si è mai spezzato. Così diverse eppure inaspettatamente simili (e folli) in certi tratti, so che potrò sempre contare su di voi. **Paco**, ritrovarci è stato davvero prezioso, sono troppo felice di averti di nuovo nella mia vita.

Thanks to the family I found away from my own, the Vreekers (or Freakers). **Marjolein**, **Rob**, **Annabel**, **Alex**, **Tim** and **Maritha**, thank you for making me feel so welcome, accepted and loved from the very first moment we met. The spontaneous and genuine affection that grew between us is truly precious and I am grateful to be part of your amazing family.

To my lieve nichtjes, **Liza**, **Bodi**, **Lotta** and **Nina**, watching you grow up is such a wonderful experience. I promise to learn how to communicate properly in Dutch with you and I like to think that one day I will be the cool aunt who can cover up your little messes. I can't wait!

Last, but not least, thanks to **Edo**. Who would have said that the tall, Dutch guy I casually met in Cambridge would become my partner for life. Thanks for your presence, your constant support, your patience, for calming my mind and my soul with your pragmatic words or simply with a hug. Thank you for bringing out the best in me. I can't wait to live many other adventures together.

ABOUT THE AUTHOR

Margherita Tavasso was born on the 30th August 1995 in Naples, Italy. She pursued her academic journey with a strong passion for chemical engineering and biological soft matter. She obtained her Bachelor of Science (BSc) in Chemical Engineering from the Scuola Politecnica e delle Scienze di Base, Federico II in Naples, Italy, where she developed a solid foundation in transport phenomena, thermodynamics, and materials science. She continued at the same institution for her Master of Science (MSc) in Chemical Engineering, graduating with distinction (110/110 cum laude). During her master's studies, she carried out research projects focused on complex fluids and microfluidics. Her thesis in Complex Fluid Mechanics was conducted during a five-month Erasmus traineeship at the University of Cambridge's Cavendish Laboratory, where she focused on the design and optimization of microfluidic devices to study red blood cell invasion by the malaria parasite under flow conditions.

Enthusiastic about the potential of *in vitro* systems to replicate pathological conditions, Margherita embarked on her PhD in Chemical Engineering at Delft University of Technology in January 2021, under the supervision of Dr. Pouyan E. Boukany and Prof. Valeria Garbin. Her research focused on the biomechanical properties of breast cancer models, employing both microfluidics and rheology to study the mechanical properties of tissue-mimicking systems. Her work combined engineering, physics, and biology to investigate how mechanical properties relate to malignancy.

Throughout her PhD, she actively collaborated with interdisciplinary teams, supervised student projects, and presented her findings at international conferences. She was teaching assistant for the Molecular Transport Phenomena course and published her research outputs in academic journals.

Following her doctoral research, she transitioned to industry by joining 1NA Technologies B.V., a company that commercialises DNA curtains flow cells, as a Business Developer.

List of Publications

Journal publications related to this dissertation:

2. I.Nagle*, **M. Tavasso***, A. D. Bordoloi, I.A. A. Muntz, G. H. Koenderink, P. E. Boukany, "Invasive cancer cells soften collagen networks and disrupt stress stiffening via volume exclusion, contractility and adhesion", *Acta Biomaterialia, 2025 (* equal author contribution).*

1. **M. Tavasso**, A. D. Bordoloi, E. Tanré, S. A. H. Dekker, V. Garbin, P. E. Boukany, "Linking Metastatic Potential and Viscoelastic Properties of Breast Cancer Spheroids via Dynamic Compression and Relaxation in Microfluidics" *Adv.Healthcare Mater.*, 2024.

Other publications:

3. M. Ahmed, T. T. Nguyen, L. Akerkouch, **M. Tavasso**, A. D. Bordoloi, T. B. Le, "Numerical modelling of tumor transport in fluid flows." Proceedings of Design of Medical Devices Conference, 2025.

2. Z. Rahman, A. D. Bordoloi, H. Rouhana, **M. Tavasso**, G. V. D. Zon, V. Garbin, P. T. Dijke, P. E. Boukany "Interstitial flow potentiates TGF-β/Smad-signaling activity in lung cancer spheroids in a 3D-microfluidic chip." *Lab on a Chip*, 2024.

1. B. Klemm, **M. Tavasso**, I.Piergentili, M. Satijn, T.G.Brevé, P. E. Boukany, R.Elkema, "Signal-triggered release of allyl-caged tertiary amine drugs from polymer hydrogels", *ChemRxiv*, 2024.

Conference Presentations

5. **M. Tavasso**, I. Nagle, G. H. Koenderink, P. E. Boukany, Annual European Rheology Conference, Leeds, UK, *Oral Presentation*, April 2024. *"Bridging the gap between bulk rheology and local deformations in cell-embedded collagen via rheo-confocal microscopy."*

4. **M. Tavasso**, A. D. Bordoloi, E. Tanré, S. A. H. Dekker, V. Garbin, P. E. Boukany, NWO Bio-Physics, Veldhoven, the Netherlands, *Oral Presentation*, October 2023. *"Mechanical properties of cancer spheroids in constricted microfluidic channels."*

3. **M. Tavasso**, A. D. Bordoloi, E. Tanré, S. A. H. Dekker, V. Garbin, P. E. Boukany, hDMT Cancer-on-Chip Meeting, Groningen, the Netherlands, *Oral Presentation*, September 2023. *"Viscoelastic response of breast cancer spheroids in constricted microfluidic channels."*

2. **M. Tavasso**, A. D. Bordoloi, E. Tanré, S. A. H. Dekker, V. Garbin, P. E. Boukany, International Rheology Congress, Athens, Greece, *Oral Presentation*, August 2023. *"Viscoelastic and plastic deformation of cancer spheroids in constricted microfluidic channels."*

1. **M. Tavasso**, A. D. Bordoloi, V. Garbin, P. E. Boukany, NWO Physics, Veldhoven, the Netherlands, *Poster Presentation*, January 2022. *"Impact of confinement on spheroids mechanobiology in constricted microchannels."*